The burn rate of calcium sulfate dihydrate-aluminium thermites

Desania Raquel Govender

Dissertation submitted in partial fulfilment of the requirements for the degree of

Master of Engineering
(Chemical Engineering)

In the Faculty of Engineering, Built Environment and Information Technology, University of Pretoria

Pretoria

January 2018

Declaration

I hereby declare that the dissertation submitted for the degree Master of Engineering: Chemical Engineering, at the University of Pretoria, is my own original work and has not previously been submitted to any other institution of higher education. I further declare that all sources cited or quoted are indicated and acknowledged by means of a comprehensive list of references.

_____   7 January 2018

Desania Raquel Govender   Date submitted

                                              15 March 2018

                                              Date revised

The burn rate of calcium sulfate dihydrate-aluminium thermites

Student: Desania Raquel Govender

Supervisor: Prof. Walter W. Focke

Department of Chemical Engineering, University of Pretoria

Degree: Master of Engineering (Chemical Engineering)

Abstract

The energetics of cast calcium sulfate dihydrate-aluminium thermites was explored and its use as a potential metal-cutting tool was investigated. Thermite is a pyrotechnic composition that undergoes a highly exothermic reaction that burns relatively slowly. It is often used in cutting, welding and incendiary devices. Consolidation of thermite by casting was chosen to enable control of the burning front. The base case thermite comprised 60 wt-% calcium sulfate dihydrate oxidiser and 40 wt-% aluminium fuel. Addition of additives were considered for their effect on the cast thermite's setting time, density, surface temperature, reaction products and burn rate. EKVI and FactSage thermodynamic simulations were used to determine optimum compositions for the various systems. The thermite powder compositions were sieved before mixing with water and casting in a mould. The casts were allowed to set for 3 days to form calcium sulfate dihydrate-aluminium compositions. The copper sulfate pentahydrate additive was found to significantly decrease the setting time of the casts. The heat of hydration of the base case was 59 ± 8 J g^{-1}. The compressive strength reached 2.9 ± 0.2 MPa, the open air burn rate was 12.0 ± 1.6 mm s^{-1} and a maximum surface temperature of 1370 ± 64 °C was recorded using a pyrometer. Bomb calorimetry indicated an energy output of 7.96 ± 1.07 MJ kg^{-1}, slightly lower than predicted by the EKVI simulation. The density of the castings was varied by either adding hollow sodium borosilicate glass spheres or by adding excess water. The glass spheres resulted in a burn rate that decreased nonlinearly with decreasing cast density. The excess water made no changes to the burning, except for increasing the burn rate of the copper sulfate pentahydrate-based thermite. Calcium sulfate in the casts was also dehydrated by thermal treatments at 155 °C and 200 °C. This resulted in significant increases in the burn rate due to the porosity created by the evaporation of the hydration waters. Castings that were thermally treated in an oven at 155 °C were successful in puncturing part of an aluminium block in confined burn tests. A hole with a diameter of ~13.6 mm and depth of ~7 mm was produced. It is recommended that the composition with copper sulfate pentahydrate be used as a binder in further tests.

Keywords: Cast thermite, Burn rate, Calcium sulfate dihydrate, Aluminium

Acknowledgements

Many thanks to my supervisor, Prof. Walter Focke, for your invaluable advice, guidance and knowledge throughout the project. I would also like to thank my mentor from the Council for Scientific and Industrial Research (CSIR), Billy Cloete. I have learned so much from you and it has been a pleasure working with you. Also, thank you to the CSIR for the financial support. Dr Shepherd Tichapondwa, thank you for always being available to listen and discuss new ideas. And thank you for your amazing stories. I am very grateful to Suzette Seymore. Thank you for being so helpful with all my administrative and general queries, and for always brightening my day. Shanana! Thank you, Isbé Van Der Westhuizen, for all your assistance with the technical instruments and equipment.

Additionally, thank you to Wiebke Grote and Jeanette Dykstra for their assistance with X-Ray Diffraction and X-Ray Fluorescence analyses. Udrie, Erna and Irene from the Laboratory for Microscopy and Microanalysis, thank you for aiding me with Scanning Electron Microscopy (SEM). Dr Maxim Kovtun and Vanessa Doman from the Department of Civil Engineering, thank you for providing information regarding the heat calorimeter and tensile tester. Further thanks must be given to Gawie Croeser and Nicholas Tsila from the CSIR, for their help in the confined burn tests.

Contents

List of Figures

List of Tables

Abbreviations

BET	Brunauer, Emmett and Teller
CSIR	Council for Scientific and Industrial Research
DTA	Differential Thermal Analysis
FTIR	Fourier Transform Infrared Spectroscopy
MSDS	Material Safety Data Sheet
SEM	Scanning Electron Microscopy/e
UP	University of Pretoria
XRD	X-Ray Diffraction
XRF	X-Ray Fluorescence

Chemical formulas

Al	Aluminium
$CaSO_4$	Anhydrite or anhydrous calcium sulfate
$CaSO_4 \cdot 0.5H_2O$	Calcium sulfate hemihydrate or Plaster of Paris
$CaSO_4 \cdot 2H_2O$	Calcium sulfate dihydrate or gypsum
$CuSO_4 \cdot 5H_2O$	Copper sulfate pentahydrate
$SiO_2/Na_2O/B$	Sodium borosilicate (glass spheres)
S	Sulfur

Glossary

Anhydrite	Anhydrous form of calcium sulfate containing no hydration water ($CaSO_4$)
Base1	Base case thermite composition containing 60 wt-% $CaSO_4 \cdot 2H_2O$ and 40 wt-% Al
Blend2	Thermite composition containing a blend of oxidisers with 30 wt-% $CaSO_4$, 30 wt-% $CaSO_4 \cdot 2H_2O$ and 40 wt-% Al
Cast	The mixing of $CaSO_4 \cdot 0.5H_2O$ (and other components such as Al fuel, additives etc.) with water to form $CaSO_4 \cdot 2H_2O$
Consolidation	Processes that combine small parts to form one object with a specific geometry, structure or property

CSP5   Thermite composition containing copper sulfate pentahydrate additive with 50 wt-% $CaSO_4 \cdot 2H_2O$, 10 wt-% $CuSO_4 \cdot 5 H_2O$ and 40 wt-% Al

Dihydrate   Form of calcium sulfate also known as gypsum containing two hydration water molecules ($CaSO_4 \cdot 2H_2O$)

GSB, GS1 – GS5   Hollow glass spheres, of loadings 0 wt-%, 5 wt-%, 9 wt-%, 13 wt-%, 17 wt-% and 20 wt-%, were added to the Base1 system to investigate the effects of lowering density

Hemihydrate   Form of calcium sulfate also known as Plaster of Paris containing half a water molecule ($CaSO_4 \cdot 0.5H_2O$)

Pyrotechnics A composition that undergoes a non-detonative, self-sustaining and exothermic reaction to produce an effect

S4   Thermite composition containing sulfur additive with 50 wt-% $CaSO_4 \cdot 2H_2O$, 20 wt-% S and 30 wt-% Al

Thermite   A pyrotechnic composition, traditionally made up of aluminium fuel and a metal oxide, capable of undergoing a highly exothermic redox reaction

T1, T2, T3   Casts were heat-treated in an oven at 155 °C (T2) and 200 °C (T3), untreated casts were labelled T1

U0, U1, U2, U3   Urea loadings of 0 wt%, 1 wt-%, 2 wt-% and 9 wt-% were dissolved in the casting water of the Base1, Blend2, S4 and CSP5 compositions

Chapter 1: Introduction

1.1. Subject

This dissertation reports on an investigation into the energetics of cast thermite compositions, made up of aluminium fuel and calcium sulfate dihydrate oxidiser, for potential use as a metal-cutting tool. Additives including calcium sulfate anhydrite, sulfur, copper sulfate pentahydrate and urea were considered to determine their effect on the linear burn rate. Additionally, the effect of density on burn rate was investigated by the inclusions of low-density hollow glass spheres.

1.2. Background and context

Pyrotechnics refer to a substance or mixture of substances that undergo a non-detonative, self-sustaining and exothermic reaction in order to produce an effect (Klapötke, 2012). Typically, one or more oxidisers and one or more fuels make up a pyrotechnic composition that react to generate heat, light, colour or gas effects (Conkling, 1985). Thermite is a pyrotechnic composition that burns at relatively slow rates and is capable of reaching very high temperatures of between 1500 – 4000 °C (Berger, 2005). For this reason, and considering their non-detonative nature, thermite devices are used in cutting tools for metals. Other applications include airbags, fire extinguishers, underwater thermite torches amongst others (Steinhauser & Klapötke, 2008, Wu et al., 2012).

Aluminium (Al) is a popular fuel choice for many reasons. It is readily available, inexpensive and possesses a high reaction enthalpy, low ignition temperature and high thermal conductivity (Wu et al., 2012). Additionally, the surface oxide layer imparts a desirable passivation nature, i.e. it provides significant corrosion protection. Meanwhile, calcium sulfate hemihydrate (hydrated to the dihydrate form) is an inexpensive oxidiser while also being non-toxic. Furthermore, it can simply be mixed with water to produce a flowable mixture that can be cast into any desired shape that will set into a monolithic part. This is advantageous as there is little to no control of the burning front of loose powder thermite compositions. Consolidation of thermite powders by casting would enable regulation and control of the burning front by creating an object with more uniform properties. When calcium sulfate hemihydrate ($CaSO_4·0.5H_2O$) is hydrated to form calcium sulfate dihydrate ($CaSO_4·2H_2O$) excess water evaporates resulting in a porous structure. The effect of this porosity on burn rate was of interest in this system.

It was assumed that the presence of pores could result in an inconsistent burn rate. To remedy this, it was suggested that additives such as anhydrous calcium sulfate ($CaSO_4$) be included as a filler. This could reduce void formation created by the evaporation of water after casting. Additionally, materials soluble in water such as copper sulfate pentahydrate ($CuSO_4 \cdot 5H_2O$) and urea ($CO(NH)_2$) could be added to the system. Since the evaporation of water would still leave voids within the structure, it was further suggested to fill the remaining voids by melting a material within the composition with a low melting point, such as sulfur (S). The effect of density on the burn rate was explored by including low-density hollow sodium borosilicate glass spheres in the system. This provided a safe way to investigate the effect of porosity or density on performance.

The Council for Scientific and Industrial Research (CSIR) is currently working on developing metal-cutting thermites, where calcium sulfate is used as a suitable inorganic binder in the energetic material. These thermites are to be prepared in-situ in the field. It was of interest to determine the energetic properties of the binder alone in terms of its setting time, how its setting rate could be accelerated and its suitability for use in metal-cutting. The findings described in this dissertation is thus a subset of the larger project and investigates calcium sulfate-aluminium thermites.

1.3. Objectives of the investigation

The objectives of the investigation were therefore to:
- Determine the optimum (i.e. maximum adiabatic flame temperature) base case thermite composition and optimum compositions of systems with additives;
- Determine whether it is possible to accelerate the setting rate of the Plaster of Paris;
- Measure the burn rates of the different systems;
- Ascertain whether the burn rate is affected by the density of the composition;
- Evaluate and compare the performance of the casts to theoretical predictions and
- Determine whether the calcium sulfate-aluminium thermites are suitable for metal-cutting.

1.4. Scope and limitations

The proposed laboratory test samples were limited in size and quantity due to licensing constraints imposed on the Pyrotechnics Laboratory at the University of Pretoria (UP). That is, mixed samples for evaluation in the test room could not exceed 50 g at any time. Additional very limited testing was conducted at the Council for Scientific and Industrial Research (CSIR).

1.5. Plan of development

The dissertation begins with a brief introduction to the research topic in Chapter 1. Chapter 2 outlines important literature and theory regarding pyrotechnics and thermite reactions. Chemical analysis techniques necessary for the investigation are also briefly highlighted. Chapter 2 ends with the research hypothesis, key questions and detailed objectives. Chapter 3 briefly outlines the experimental methodology that was followed while Chapter 4 includes findings from EKVI and FactSage thermodynamic simulations. Characterisation of raw materials is presented in Chapter 5. Results and discussions of the burn tests are given in Chapter 6. Finally, Chapter 7 details conclusions and recommendations.

Chapter 2: Theory and literature review

2.1. Pyrotechnics

The word "pyrotechnics" is derived from Ancient Greek meaning "art of fire" or "art of handling fire" (Klapötke, 2012). Pyrotechnics refer to a substance or mixture of substances that undergo a non-detonative, self-sustaining and exothermic reaction in order to produce an effect (Klapötke, 2012). Typically, one or more oxidisers and one or more fuels makes up a pyrotechnic composition that react to generate heat, light, colour or gas effects (Conkling, 1985). Pyrotechnics are used extensively in a wide range of applications besides perhaps the most well-known form of fireworks. Other technical uses include airbags, fire extinguishers, flares, matches and propellants (Steinhauser & Klapötke, 2008).

Pyrotechnics differ from propellants and explosives by their rate of reaction. While explosives react very fast and propellants slow, pyrotechnics lie between the two in terms of the reaction rate. Another property singular to a pyrotechnic is that it is a mixture of an oxidiser and fuel molecules, in contrast to explosives where both oxidiser and fuel are contained in one and the same molecule (Klapötke, 2012).

Pyrotechnic reactions differ from typical combustion reactions as they do not require the presence of ambient air in order to occur (Berger, 2005). Since a typical pyrotechnic composition is made up of a fuel and an oxidiser, the oxidiser provides the oxygen required for the reaction to proceed (Steinhauser & Klapötke, 2010). Optional additives to the composition include binders, propellants and colouring agents (Steinhauser & Klapötke, 2008).

Reactions involving pyrotechnic compositions are highly exothermic, consequently reaching temperatures in the range of approximately 1500 – 4000 °C (Berger, 2005). They generally undergo a redox reaction, which requires a reducing agent (fuel) as well as an oxidiser to occur. The resulting products are an oxidised reducing agent and a reduced oxidiser. The reaction can be solid-solid, solid-liquid or solid-gaseous in phase (Berger, 2005). Most pyrotechnic reactions are solid-solid reactions and, for this reason, particle size and homogeneity of the mixture are of the utmost importance (Steinhauser & Klapötke, 2008).

The chemicals involved in the redox reaction influence the way the reaction proceeds. Consequently, it is important that these chemicals are well-defined by means of purity, particle size and shape, particle surface, crystal structure and water content (Berger, 2005).

2.1.1. Thermite reaction

Thermite is a pyrotechnic composition typically made up of aluminium fuel capable of undergoing a highly exothermic reaction. Generally, thermite reactions include a metal and a metallic (or non-metallic) oxide that form a more stable oxide and the metal (or non-metal) of the reactant oxide (Wang et al., 1993). Thermite reactions can thus be portrayed in the general form

$$M + AO \xrightarrow{-\Delta H} MO + A \hspace{3cm} (1)$$

Where, metal M reacts with metal oxide AO to form the corresponding metal oxide MO and the reduced metal A.

Thermite reactions are highly exothermic and they result in large amounts of heat being released. This allows thermite reactions to be initiated locally and thereafter enables the reaction to be self-sustaining and energy efficient. Often, the heat release is large enough to reach and exceed the melting points of the reaction products, resulting in products of a heavy metallic phase and a lighter oxide phase (Wang et al., 1993). The presence of oxidiser within the thermite composition means that the reaction will occur without requiring any external oxidiser, but it should be noted that the reaction may be enhanced by interaction with oxygen in the surrounding environment (Conkling, 1985).

2.1.2. Thermodynamics of pyrotechnic compositions

According to Kosanke and Kosanke (1994), pyrotechnics are said to exist in a metastable region. This means that under normal conditions the material is stable, however upon ignition the reaction becomes self-sustaining. Pyrotechnics do not spontaneously combust; instead, they require an energy input in order to ignite and thereafter burns to produce energy (Kosanke & Kosanke, 1994). Figure 2-1 illustrates the changes to the internal energy of a system from the initial ignition to the end of the reaction.
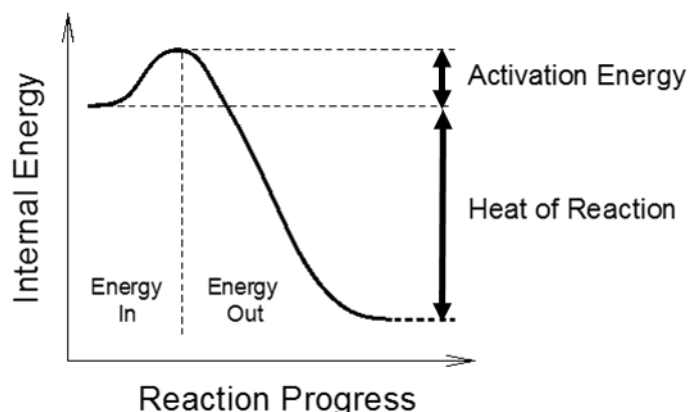
Figure 2-1: Changes to internal energy upon ignition and burning of a pyrotechnic composition (adapted from Kosanke & Kosanke, 1994)

As seen in Figure 2-1, the minimum energy input required for ignition to occur is referred to as the activation energy. Once ignited, the pyrotechnic composition burns and energy is produced in this process. The heat of the reaction, as indicated in Figure 2-1, refers to the net energy produced (Kosanke & Kosanke, 1994).

The Ellingham diagram is a graph showing the thermodynamic driving force for a particular reaction over a range of temperatures (Kumar et al., 2008). It can be used to evaluate and compare the stability of an element and its oxide. An effective method of comparing the stability of metals and their oxides is to compare their standard Gibbs free energy (Rutter & Bennet, 2015). Basic thermodynamics and chemistry is used to plot an Ellingham diagram.

The chemical reaction A + B → C + D will proceed spontaneously if the total Gibbs free energy change (ΔG) is negative, which is the difference between the Gibbs free energy of the products and reactants. Assuming a standard state of 1 atm, the general form is

$$\Delta G = \Delta G^{\circ} + RT \ln \left(\frac{a_C \, a_D}{a_A \, a_B} \right) \tag{2}$$

Where, ΔG and ΔG° are the total and standard Gibbs free energy change (kJ mol^{-1}), RT is the product of the ideal gas constant (kJ mol^{-1} K^{-1}) and temperature (K). The dimensionless activity of each of the reaction species is represented by a.

At equilibrium conversion, the change in the total Gibbs free energy is zero and rearranging Equation 2 gives

$$\Delta G^{\circ} = -RT \ln (K) \tag{3}$$

Where, K is the dimensionless equilibrium constant for the reaction. For an ideal gas phase reaction A + B → C + D, the equilibrium constant K_p is

$$K = K_p = \frac{p_C \, p_D}{p_A \, p_B} \tag{4}$$

Similarly, the equilibrium constant for the reaction of a metal with oxygen can be determined. Taking the reaction of aluminium with oxygen as an example,

$$\text{4/3 Al}_{(s)} + O_{2\,(g)} \rightarrow \text{2/3 Al}_2O_{3\,(s)} \tag{5}$$
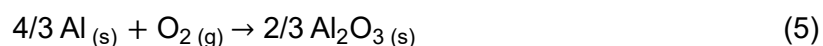
and assuming that Al and Al_2O_3 are in their pure crystalline state, the equilibrium constant is

$$K_p = 1/p_{O_2} \tag{6}$$

Where, p_{O_2} is the partial pressure of oxygen (Pa). It should be noted that the equilibrium constant may change with reaction stoichiometry. It is therefore convenient to ensure that each reaction occurs with a consistent 1 mole of O_2, since oxygen is a variable component of each of the reactions (Rutter & Bennet, 2015).

Another way of expressing the standard Gibbs free energy is given by Equation 7

$$\Delta G^{\circ} = \Delta H^{\circ} - T\Delta S^{\circ} \tag{7}$$

Where, ΔG° is the change in standard Gibbs free energy (kJ mol^{-1}), ΔH° is the change in standard enthalpy of reaction (kJ mol^{-1}) and ΔS° is the change in standard entropy of reaction (kJ mol^{-1} K^{-1}). The temperature is shown by T (K). Equation 7 can be likened to the equation of a straight line, since the variations in enthalpy and entropy are negligible. Equation 8 shows the general equation of a straight line, where m is the gradient of the line, c is the y-intercept, x is the independent variable and y is the dependent variable.

$$y = mx + c \tag{8}$$

The gradient of each line corresponds to the change in standard entropy in Equation 9, which is only valid at a constant pressure.

$$m = \frac{d\Delta G^\circ}{dT} = -\Delta S^\circ \tag{9}$$

Since the values of ΔS° are typically negative, the gradient of each metal/oxide straight line is in fact positive. Furthermore, the y-intercept of each straight line corresponds to the change in standard enthalpy of reaction since it can be assumed that there are negligible changes in enthalpy and entropy with respect to temperature (Rutter & Bennet, 2015). These straight lines can be plotted for different metals and their oxides. Figure 2-2 shows an Ellingham diagram displaying a plot of ΔG° (kJ mol^{-1} O$_2$) vs T (°C). It shows the standard Gibbs free energy of various metals and their oxides at different temperatures,
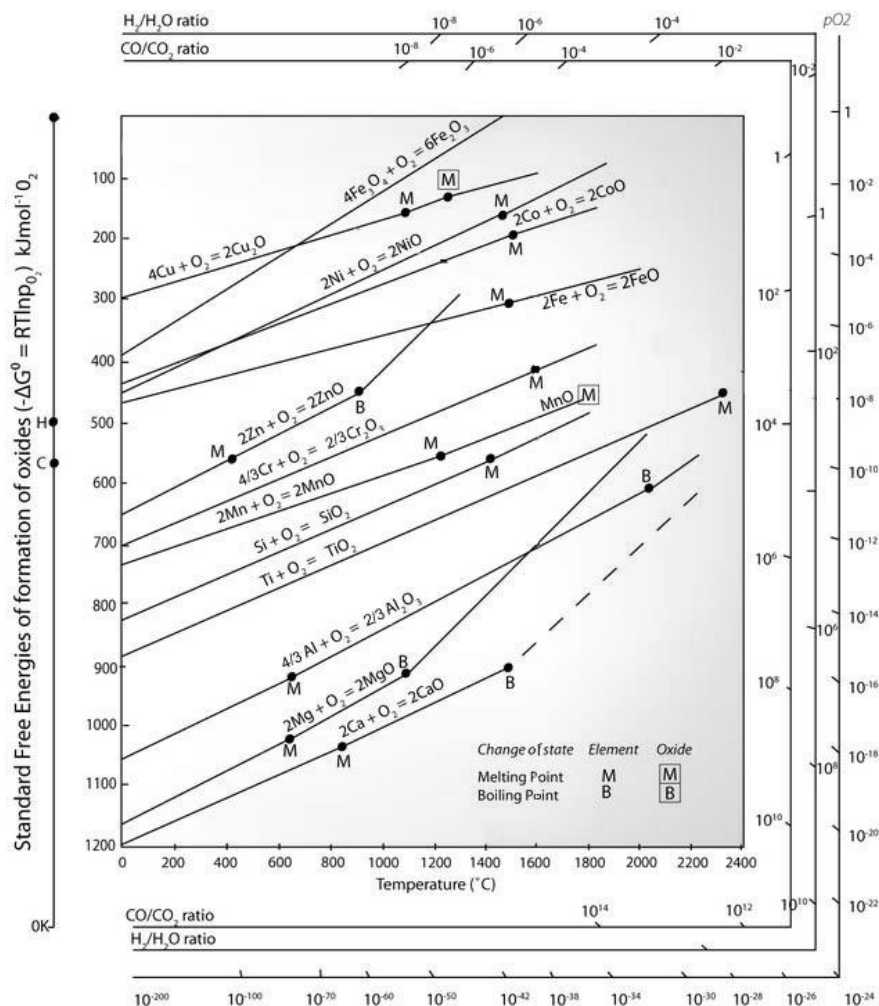
Figure 2-2: An example of an Ellingham diagram (Kumar et al., 2008)

Metal oxidation lines located higher up on the Ellingham diagram in Figure 2-2 indicate a higher stability than those located lower down. The lower a metal is located, the more negative its standard Gibbs free energy change. For all temperatures, metals located lower down on the diagram potentially result in a larger equilibrium constant. This means that the reaction is more favoured to the products and consequently is more likely to occur. The oxides of these metals are thus more stable than those located higher up.

2.1.3. Ignition of pyrotechnic composition

The onset temperature at which sufficient heat is released that would result in a self-sustained reaction between fuel and oxidiser is called the ignition temperature of the composition (Conkling, 1985). Typically, an oxidiser would first melt or decompose, thus releasing its oxygen and making it available to partake in the reaction. Therefore, reaction rates will be slower if the oxidiser decomposes at a higher temperature but will be faster when an oxidiser decomposes at a lower temperature (Conkling, 1985). The external energy required for the compositions to reach the onset temperature may be in the form of friction, impact, hot wire or a burning fuse providing external heat, amongst others (Conkling, 1985).

The critical ignition temperature, T_{ign}, is the minimum temperature to which a thermite charge of specified size, shape and boundary constraints must be heated in order to induce thermal runaway. The heat generated by the reaction inside the sample is compared to the heat lost to the environment. This balance determines whether ignition occurs and a reaction becomes self-sustaining.

The physics underpinning the concept of the ignition temperature is illustrated in Figure 2-3.
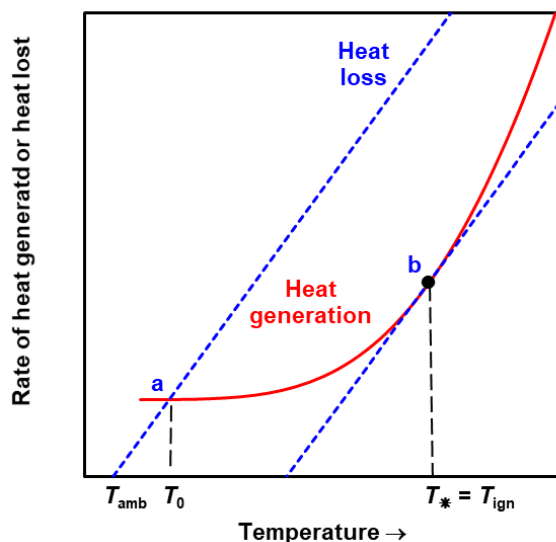
Figure 2-3: Semenov diagram indicating the heat generated by the sample and (a), (b) heat lost to the environment as a function of temperature (Merzhanov & Abramov, 1981)

Figure 2-3 shows that the rate of heat generated by the pyrotechnic reaction in the sample is proportional to the rate of the reaction described by the Arrhenius equation. The rate of heat release at lower temperatures is slow but increases exponentially with temperatures (see red curve). During the reaction, however, the composition interacts with the surroundings and heat is lost through conduction, convection and radiation processes as shown by the blue curves (Merzhanov & Abramov, 1981). In the simplest theory, it is assumed that the heat loss is proportional to the temperature of the environment, and that the heat transfer coefficient is a constant (Merzhanov & Abramov, 1981). Therefore, the cooling curve is a straight line with slope proportional to the heat transfer coefficient.

Figure 2-3 shows two scenarios. In the first scenario at point (a), the temperature of the environment is the same as that of ambient temperature. The cooling curve and the heat of reaction curves cross at the bottom left corner at point (a). This corresponds to a temperature of the sample that is slightly higher than ambient. Stability analysis shows that this is a stable situation: If the sample temperature is increased slightly, the heat loss to the environment is greater than the heat generated by the reaction and the sample cools down. If the temperature of the environment is increased a bit, the result is simply that the intersection of the two curves moves to higher temperatures. However, if the temperature of the environment is set to very high values, then it is possible that the two curves do not intersect at all. In this case, the heat generated by the reaction is always higher than the heat lost to the environment. The sample

will raise its temperature by self-heating and a thermal runaway occurs. Therefore, the critical ignition temperature corresponds to the situation where the cooling line corresponds to a tangent to the heat of reaction curve, seen at point (b) in Figure 2-3.

2.1.4. Determining the burn rate

Various theoretical models have been proposed to describe the self-propagating mechanism of solid-to-solid reactions, including two cases of kinetics-controlled and diffusion-controlled reactions Montgomery et al. (2016).

The kinetics-limited case in Equation 10 considers an nth order gasless exothermic solid-state reaction where physical properties are independent of composition and temperature. Furthermore, it disregards phase changes, assumes a thin reaction zone and that the rate constant follows an Arrhenius-type temperature dependency (Khaikin & Merzhanov, 1966).

$$u^2 = \frac{g(n)\ RT_c^2}{E_a\ (T_c - T_o)}\ (\alpha k_o)\ e^{-\frac{E_a}{RT_c}} \tag{10}$$

Where, u^2 is the burning velocity (m s^{-1}), $g(n)$ is a function of reaction order n between $n = 0.5 - 2.0$ (dimensionless). T_o and T_c are the initial and maximum temperature of the burning column respectively (K). The apparent Arrhenius activation energy is E_a (J mol^{-1}) and the Arrhenius pre-exponential factor of reaction rate constant is k_o (s^{-1}). Thermal diffusivity is represented by α (m^2 s^{-1}).

On the other hand, Equation 11 assumes the reaction is mass and energy transport limited, or diffusion-controlled, meaning the burn rate is calculated with thermal diffusivities, mass diffusivities and the particle size (Montgomery et al., 2016). This model determines burn rate by considering ordered layers of reactants, the thickness of which is determined by stoichiometry and density. Again, phase changes are not considered and it assumed that products form instantaneously once components become in contact with other (Aldushin & Khaikin, 1974).

$$u^2 = \frac{6\ RT_c^2}{E_D\ (T_c - T_o)}\ \left(\frac{\alpha D_o}{d^2}\right)\ e^{\frac{E_D}{RT_c}} \tag{11}$$

Where, E_D is the effective pre-exponential factor for the diffusion coefficient (m^2 s^{-1}) while D_o is the apparent activation energy for the diffusion coefficient (J mol^{-1}). Furthermore, d represents the particle size distribution of the reactants (m).

2.1.5. Factors affecting burn rate

2.1.5.1. Reducing agent and oxidiser

The optimum fuel to oxidiser ratio is one that produces the highest energy output but not necessarily the fastest burn rate. Typically, this optimum ratio results in the least amount of fuel or oxidiser being left over after the completion of the reaction (Kosanke & Kosanke, 1994). Deviation from the optimum ratio would result in lower burn rates, since the heat of reaction is lowered. This is since there is more unreacted material left over after the reaction that did not contribute to the energy produced. The equivalence ratio (∅) is an indicator for a fuel and oxidiser being mixed in a stoichiometric, fuel-rich or fuel-lean manner (Janbozorgi et al., 2010). See Equation 12. If ∅ $= 1,$ the mixture is stoichiometric. For values of ∅ > 1, the mixture is said to be fuel-rich while values ∅ < 1 indicate a fuel-lean mixture.

$$\emptyset = \frac{\left(\dfrac{m_F}{m_A}\right)_{act}}{\left(\dfrac{m_F}{m_A}\right)_{st}} = \frac{\left(\dfrac{n_F}{n_A}\right)_{act}}{\left(\dfrac{n_F}{n_A}\right)_{st}} \tag{12}$$

Where, m_F and m_A is the mass of fuel and oxidiser respectively (g) while n_F and n_A is the mole of fuel and oxidiser respectively (mol). Subscripts "act" and "st" refer to actual and stoichiometric amounts.

2.1.5.2. Particle size

The burn rate increases as the particle size of the fuel or oxidiser becomes smaller (Kosanke & Kosanke, 1994). Decreasing the size of particles results in a reduction in the activation energy required for the reaction to proceed, since less energy is required to heat smaller particles to ignition. The particle size of the fuel has a greater effect on burn rates, which is due to fuels having a higher melting temperature that is typically greater than the ignition temperature (Kosanke & Kosanke, 1994).

2.1.5.3. Particle shape

The effect of particle shape on the burn rate is similar to that shown by particle size. Figure 2-4 shows the effect of different shapes of aluminium particles on the burn rate. The fastest burn rate was produced by flakes while spherical particles produced slower burn rates. This can be explained by the fact that flakes have a larger surface area available for the reaction to occur.
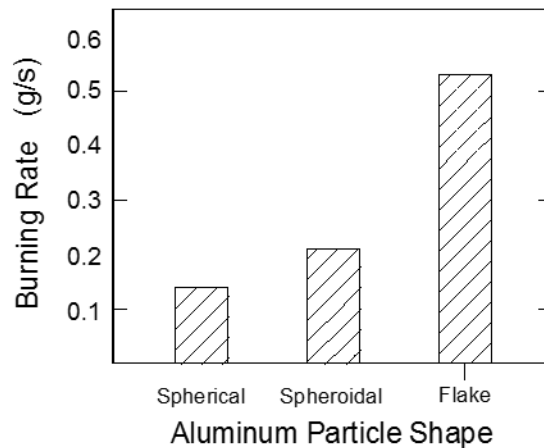
Figure 2-4: Effect of aluminium particle shape on burn rate (Kosanke & Kosanke, 1994)

2.1.5.4. Oxygen balance

The potential of an oxidiser can be determined by completing an oxygen balance, which can also be shown by obtaining an equivalence ratio. The value obtained from Equation 13 is indicative of a system's ability to undergo complete combustion; that is where all fuel is consumed in the reaction leaving no residue behind (Steinhauser & Klapötke, 2008).

$$OB = 100\frac{n_{Ox}M_{Ox}u}{n_{Red}M_{Red} + n_{Ox}M_{Ox}} \tag{13}$$

Where, OB refer to the oxygen balance (%) while M_{Ox} and M_{Red} refer to the molecular weight of oxygen and the reducing agent respectively (g mol^{-1}). The number of oxygen atoms in the oxidiser is represented by dimensionless u and the moles of oxygen is given by n (mol).

For $OB = 0$, it shows that the mixture of fuel and oxidiser atoms is stoichiometric in nature. When $OB < 1$, there is insufficient oxygen for the reaction to proceed and that there will be unburned fuel remaining upon completion. On the other hand, $OB > 1$ indicates that there is an excess of oxygen atoms for combustion of the fuel.

2.1.5.5. Degree of mixing

The reaction rate can be maximised by ensuring homogeneity in the composition (Berger, 2005). For a diffusion-controlled reaction, better contact between fuel and oxidiser means diffusion distances between the particles are reduced (Pantoya & Granier, 2005). This results in a faster burn rate. Poor mixing and insufficient contact between fuel and oxidiser may however result in the heat of reaction not being severely affected. This is since all the material will react; however, it will take longer than usual (Kosanke & Kosanke, 1994).

2.1.5.6. Additives

Besides the base fuel and oxidiser, pyrotechnic composition may also include other additives depending on the required effect. For example, large granular fuel particles may be added to produce sparks while binder may be added to combine and keep the composition together (Kosanke & Kosanke, 1994).

2.2. Burn rates of micron- and nano-thermites

Weismiller et al. (2011) investigated factors affecting the propagation rate of thermite by varying the size of fuel and oxidiser particles in the micrometer and nanometer size range. The aluminium-based thermite contained copper oxide (CuO) and molybdenum trioxide (MoO_3) oxidisers. It was found that nano-fuel/nano-oxidiser compositions propagated the fastest. Furthermore, it was found that micron-aluminium/nano-oxidiser compositions propagated significantly faster than nano-aluminium/micron-oxidiser compositions. This is since micron-aluminium inherently contains a thin aluminium oxide (Al_2O_3) layer that acts as a passivating layer that inhibits further oxidation while nano-aluminium contains an oxidising layer that is relatively thicker making ignition and propagation more difficult (Pantoya & Granier, 2005).

The heats of reaction of micron-sized aluminium oxide compositions were found to be in the range of 1.5 – 4.8 MJ kg^{-1} with burn velocities in the range of 200 – 840 m s^{-1} (Comet et al., 2015). This is contrasted with the nano-sized aluminium oxide compositions that produced heats of reaction between 4 – 6 MJ kg^{-1} and combustion velocities of 100 – 2500 m s^{-1} (Comet et al., 2015).

2.3. Sulfates-based thermites

Typically, most oxygen-containing anions possess only slightly negative and sometimes positive standard Gibbs free energy of formations. Despite unfavourable thermodynamics, metal sulfates have been used in conjunction with micron- and nano-aluminium in thermite compositions. This is since some anions such as sulfates (SO_4^{2-}) and phosphates (PO_4^{3-}) possess low Gibbs energies of formations, i.e. -745 kJ mol^{-1} and -1019 kJ mol^{-1} respectively (Comet et al., 2015). Metal sulfates including calcium (Ca), copper (Cu) and magnesium (Mg) were used as oxidisers with nano- and micron-sized aluminium fuel. Weismiller et al. (2011) reported that the nanothermites produced combustion velocities of $\sim$1 km s^{-1}, significantly higher than conventional thermite. Furthermore, Tichapondwa et al. (2015) used anhydrous calcium sulfate with silicon for application in "green" pyrotechnic time delays, resulting in burn rates of between 6.9 – 13 mm s^{-1} and energy outputs of between 1.97 – 3.87 MJ kg^{-1}.

It has been reported that the water of hydration associated with the sulfate increases the heat of reaction while also significantly influencing the sensitivity to impact and electrostatic discharge (Comet et al., 2015). Fitzpatrick (1959) was the first to suggest using highly hydrated salts as a source of "solid" water for the reaction of metal fuel with water. Water was used as a source for oxidation with the preferred salt being Epsom salts ($MgSO_4 \cdot 7H_2O$) because of its non-toxicity and low cost. Other salts used were considered on the basis of their available heat energies, thermal stability, decomposition hazards, burn rate amongst various other factors (Fitzpatrick, 1959). Magnesium (Mg) or magnesium/aluminium alloys were preferred as the fuel. Sulfur dioxide (SO_2) was the only toxic by-product released; however, not in quantities sufficient for it to be harmful. The proposed reaction mechanism was that ignition of the thermite would induce the breakdown of a water molecule. This water would thereafter react with the fuel to produce hydrogen gas and a metal oxide. Once the reaction becomes self-sustaining, the heat generated would further breakdown the salt to produce water vapour to react with the metal fuel.

Similarly, Schroder & Dass (2012) have made use of hydrated salts with nano-aluminium particles. Reaction 14, between aluminium and water, is theoretically exothermic possessing a heat of reaction (ΔH) of -818 kJ (Schroder & Dass, 2012)

$$2Al_{(s)} + 3H_2O_{(l)} \rightarrow Al_2O_{3(s)} + 2H_{2(g)} \qquad (14)$$
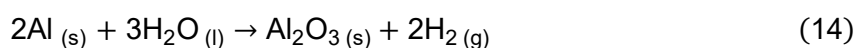
While the reaction between aluminium and water is capable of being very energetic, it is not often used as an energetic material since the reaction is very slow. It is difficult to ignite compositions containing aluminium particles, 5 μm in diameter, mixed with a stoichiometric amount of water since the reaction does not propagate (Schroder & Dass, 2012). However, in contrast very fine aluminium, e.g. nano-aluminium particles < 200 nm in diameter results in very fast reaction rates similar to a burning propellant. At room temperature, however, nano-aluminium of 80 nm diameter reacts with de-ionised water within a few minutes after mixing (Schroder & Dass, 2012).

Schroder & Dass (2012) proposed two different methods of creating energetic materials. The first involves dissolving the hydrate salt in a solvent after which fuel particles are added to the salt solution. The solvent is then removed, leaving behind an energetic composition. The second method involves dispersing the fuel in a solvent and then dissolving the hydrate in the dispersion. The solvent is preferably water, which is thereafter removed by methods such as evaporation, heating, vacuum drying and freeze drying amongst various others (Schroder & Dass, 2012).

Olander and Petersen (1983) patented a preparation method for castable and combustible compositions based on aluminium, calcium sulfate and magnesium sulfate. Water was included as part of this mixture where hydration water was taken into account. Additional water should be added if anhydrous calcium sulfate is used. The composition of the components used are displayed in Table 2-1.

Table 2-1: Thermite composition used by Olander and Petersen (1983)

Component	Composition
Aluminium (Al)	$m_{Al} = m_{CaSO_4 \cdot 0.5H_2O}$
Calcium sulfate hemihydrate ($CaSO_4 \cdot 0.5H_2O$)	$m_{CaSO_4 \cdot 0.5H_2O} = m_{Al}$
Magnesium sulfate ($MgSO_4$)	$0.5\ n_{CaSO_4 \cdot 0.5H_2O}$
Water (H_2O)	$6\ n_{MgSO_4}$

m = mass, n = moles

Table 2-1 shows that equal parts of aluminium (Al) and calcium sulfate hemihydrate ($CaSO_4 \cdot 0.5H_2O$) were used by Olander and Petersen (1983). These fuel and oxidiser combinations were effective in ratios of between 1.0:5.7 and 1.0:0.67 (Olander & Petersen, 1983). A solution of magnesium sulfate ($MgSO_4$) was added to the fuel and oxidiser powders. The amount of $MgSO_4$ was 1.5 times the molar amount of $CaSO_4 \cdot 0.5H_2O$, which was

combined with water approximately 6 times the molar amount of $MgSO_4$. Additional water was added by trial and error to enable effective mixing of the mixture before curing. It was found that the addition of 1 – 4 wt-% glycerin controlled the burn rate by decreasing it and increased the strength of the casted structure (Olander & Petersen, 1983).

It was found that aluminium and gypsum ($CaSO_4 \cdot 2H_2O$) compositions that consist of micron-sized particles are capable of burn speeds in the range of a few cm s^{-1} while nanothermites burn at much faster rates of 200 – 840 m s^{-1} (Comet et al., 2015). The water in hydrates such as gypsum are bound by a small amount of energy, which prevents it from spontaneously reacting with the fuel particles (Comet et al., 2015). Comet et al. (2015) determined the heat evolved from reactions containing nano-aluminium and sulfate compounds by using a parabolic law based on the aluminium content (X_{Al}) of the composition. The parabolic law describes the heat of reaction (Q_{exp}) on the condition that compositions are stoichiometric (± 20 wt-%)

$$Q_{exp} = A_i\, X_{Al}^2 + B_i\, X_{Al} + C_i \tag{15}$$

Where, Q_{exp} is the heat of reaction (J g^{-1}) with constants A_i, B_i, C_i (J g^{-1}). The aluminium content is X_{Al} (wt-%). The constants A_i, B_i and C_i are shown for various sulfates in Table 2-2.

Table 2-2: Experimentally determined constants for determining heats of reaction of various n-Al/sulfate compositions (Comet et al., 2015)

Sulfate	A	B	C	Q_{max} (MJ kg^{-1})	$X_{Al, max}$ (wt-%)
$BaSO_4$	−1.5673	150.74	−279.71	3.34	48.1
$Bi_2(SO_4)_3$	−3.2917	294.56	−1662.7	4.93	44.7
$CaSO_4 \cdot 2H_2O$	−3.3616	347.54	−3816	5.17	51.7
$CuSO_4 \cdot 5H_2O$	−3.5182	360.75	−3349.2	5.90	51.3
$MgSO_4 \cdot 6H_2O$	−4.1926	456.27	−6813.4	5.60	54.4

Table 2-2 shows the maximum heat of reaction (Q_{max}) and the optimised aluminium loading ($X_{Al, max}$). These values were calculated by differentiating Equation 15 for each sulfate (Comet et al., 2015). It was found that the heat of reaction was higher for the hydrated sulfates.

Increasing the nano-aluminium content with calcium sulfate resulted firstly in dehydration, next in the production of aluminate and lastly the formation of calcium sulfide (Comet et al., 2015). The needle-like structure of the $CaSO_4 \cdot 2H_2O$ means that the composition's density is not influenced by compaction (Comet et al., 2015). Comet et al. (2015) observed that combustion rates of sulfates-based nanothermites varied like their heats of reaction in that they increase with hydration. The combustion rates were also found to increase with porosity, which fits the convective propagation mechanism (Comet et al., 2015).

After heating, n-Al/$CaSO_4 \cdot 2H_2O$ decomposed firstly at around 85 – 120 °C by the removal of hydration water molecules. The melting point of aluminium is 660 °C. The n-Al particles oxidised in two steps at around 480 – 660 °C and at 660 – 870 °C. Firstly, oxidation of solid aluminium occurs where oxygen diffused through the outer alumina (Al_2O_3) shell to the inner aluminium core. Secondly, oxidation of the liquid aluminium occurred. The liquid aluminium escaped from the cracks in the shell created by the expansion of the molten aluminium. Sulfate decomposition occurred at higher temperatures at 1150 – 1330 °C, which was lowered to 1010 – 1190 °C when considering the composite with aluminium.

Thermogravimetric analysis (TGA) was conducted on the composite and results are shown in Figure 2-5.
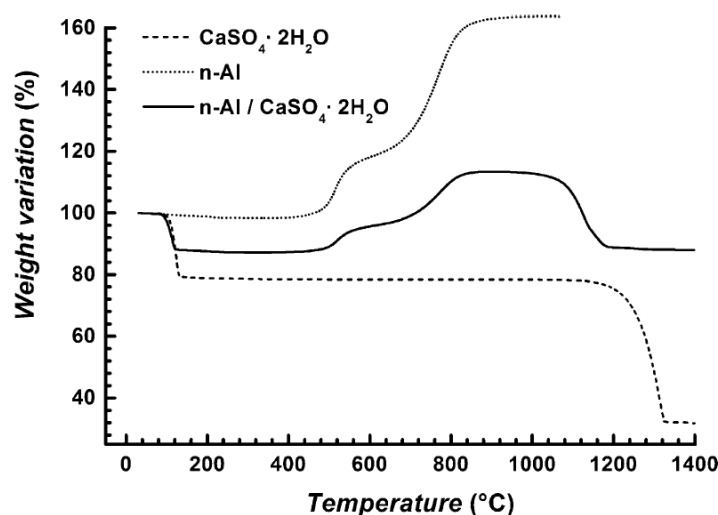
Figure 2-5: Thermogravimetric analysis of the slow decomposition of n-Al/ $CaSO_4 \cdot 2H_2O$ composites in an oxidising atmosphere (Comet et al., 2015)

The composition ignites readily and the reaction proceeds as a slow, sparkling combustion (Comet et al., 2015). The immediate reaction is that of aluminium with water. At times when this does not occur immediately, the sample heats up until it is red and then reacts abruptly. The reaction with the sulfate takes longer to occur since it requires prolonged pre-heating.

Thermites made up of micron-sized sulfates possess a higher impact-sensitivity threshold than nano-sized sulfates (Comet et al., 2015). The relationship between the impact sensitivity threshold and the number of hydration waters follows a parabolic law, where a minimum is reached with five water molecules (Comet et al., 2015). Samples that were subjected to impact induced the reaction between aluminium and water. The sample was thus more sensitive with increased amounts of water since the reaction was more easily initiated. However, the reaction was more difficult to initiate when more water molecules (n) are present (that is $n > 5$) because of the heat-sink effect of water (Comet et al., 2015).

Sulfate-based thermites are considerably more sensitive to electrostatic discharge than most oxide-based thermites (Comet et al., 2015). Furthermore, it is assumed that the presence of the water molecules increases electrical conductivity of the composition (Comet et al., 2015).

2.4. Calcium sulfate oxidiser

Calcium sulfate is a white, odourless powder. There are three different forms of calcium sulfate including the anhydrite ($CaSO_4$), hemihydrate ($CaSO_4 \cdot 0.5H_2O$) and dihydrate ($CaSO_4 \cdot 2H_2O$). The dihydrate is more commonly known as gypsum. The hemihydrate, which can be derived from the dihydrate, is often referred to as Plaster of Paris. It forms a mouldable paste when mixed with water and thereafter hardens into the dihydrate form. The hemihydrate is slightly soluble in water with a solubility of 0.65 g/ 100 mL at 20 °C while the dihydrate has a lower solubility of 0.24 g/ 100 mL (Lewry & Williamson, 1994).

Gypsum undergoes dehydration to form Plaster of Paris when heat is applied, as shown by Reaction 16

$$CaSO_4 \cdot 2H_2O \xrightarrow{+\Delta H} CaSO_4 \cdot 0.5H_2O + 1.5H_2O \qquad (16)$$
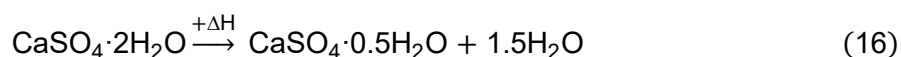
This endothermic reaction may commence at a temperature around 107 °C, which varies with ambient conditions (Ramsdell & Partridge, 1929). It has been reported by de Korte (2015) that Reaction 16 occurs in the range of 120 – 180 °C.

Two forms of hemihydrate may form depending on the production process used. The α-hemihydrate is produced by wet methods such as autoclaving while the β-hemihydrate is produced by dry methods such as calcining (Lewry & Williamson, 1994). These forms differ with respect to their reactivity with water and the strength of the resulting hydration products (Singh & Middendorf, 2007). The α-hemihydrate is quite hard and relatively insoluble as opposed to the β-hemihydrate (Thomas & Puleo, 2009). A scanning electron microscope (SEM) has shown that the α-hemihydrate has well-formed idiomorphic crystals while the β-hemihydrate features more flaky crystals as shown in Figure 2-6.
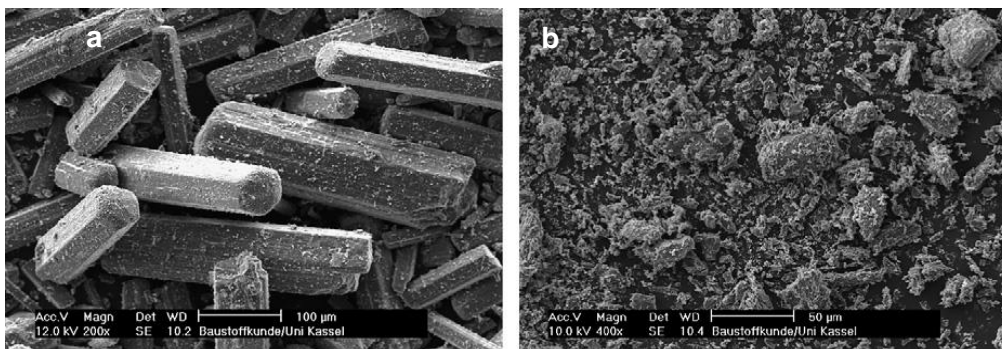
Figure 2-6: Morphology of (a) α-hemihydrate and (b) β-hemihydrate at 200 and 400 magnification respectively (Singh & Middendorf, 2007)

Figure 2-7 compares both forms of the hydrates at 10 µm, showing the β-hemihydrate that is more flaky than the α-hemihydrate.
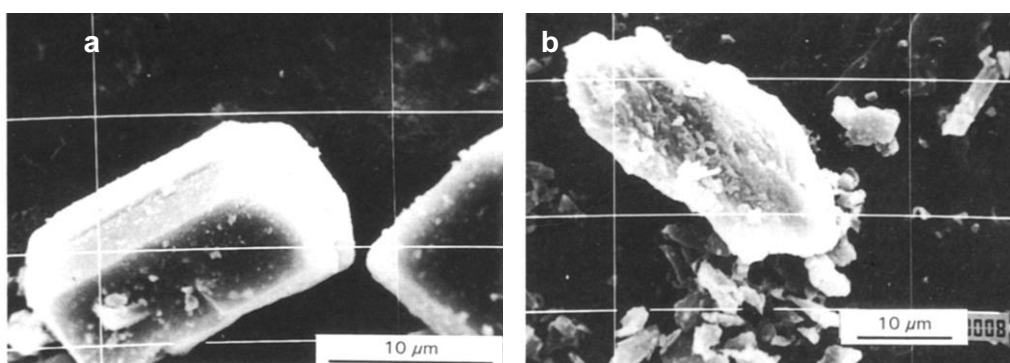
Figure 2-7: Calcium sulfate hemihydrate morphology at 10 µm (a) α-hemihydrate and (b) β-hemihydrate (adapted from Lewry & Williamson, 1994)

While the two forms of hemihydrate are chemically identical, their physical properties do differ. Thomas and Puleo (2009) report that the α-hemihydrate requires 0.3 g water/ g hemihydrate in order to be hydrated to the dihydrate form, which is less than the 0.6 g water/g hemihydrate required for the β-hemihydrate. Consequently, the α-form sets to produce a dihydrate that is denser. Thus, the α-hemihydrate produces gypsum that is stronger than that formed by the β-hemihydrate (Lewry & Williamson, 1994). Calcium sulfate hemihydrate can further be dehydrated to its anhydrous form, see Reaction 17. According to de Korte (2015), soluble $CaSO_4$ is formed when maintained under laboratory conditions of 50 °C in a vacuum of 100 % relative humidity. Heating of calcium sulfate hemihydrate to temperatures between 300 – 900 °C produces insoluble $CaSO_4$ (de Korte, 2015).

$$CaSO_4 \cdot 0.5H_2O \xrightarrow{+\Delta H} CaSO_4 + 0.5H_2O \qquad (17)$$
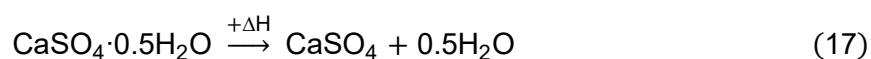
The hydration of calcium sulfate hemihydrate (Plaster of Paris) produces calcium sulfate dihydrate (gypsum) by the exothermic Reaction 18 at ambient conditions. Tydlitát et al. (2008) have reported hydration heats measured using an isothermal differential calorimeter to be 111.9 ± 0.50 J g^{-1} and 100.0 ± 0.50 J g^{-1} for α-hemihydrate and β-hemihydrate respectively. The process of hydration involves both heat generation and an increase in volume upon casting (Padevĕt et al., 2011).

$$CaSO_4 \cdot 0.5H_2O + 1.5H_2O \xrightarrow{-\Delta H} CaSO_4 \cdot 2H_2O \qquad (18)$$

Reaction 18 occurs in stages. Firstly, in an induction period during which nuclei form, dissolution of the hemihydrate results in a supersaturated solution of the dihydrate (Ludwig & Singh, 1978). The number of nuclei present dependents on the water to gypsum ratio and temperature amongst other properties (Tydlitát et al., 2008). The dihydrate then nucleates and precipitates into needle-like crystals that form an interlocking crystal mass (Ludwig & Singh, 1978). Nucleation and crystallisation is increased when influenced by external factors such as stirring (Ludwig & Singh, 1978). Finally, the reaction stops when there is no longer any hemihydrate present or when all the water present has been used.

Unmodified plaster begins to set 10 minutes after mixing with water and is complete after 45 minutes but the cast is only fully dry after 72 hours (Sharma & Prabu, 2013). Plaster of Paris possesses a desirable property in that it can be moulded into any desired shape (Sharma & Prabu, 2013).

The physical properties of each of the calcium sulfates is summarised in Table 2-3.

Table 2-3: Physical properties of calcium sulfates (de Korte, 2015)

Property	$CaSO_4 \cdot 2H_2O$	$CaSO_4 \cdot 0.5H_2O$	$CaSO_4$
Other names	Calcium sulfate dihydrate	Calcium sulfate hemihydrate	Calcium sulfate anhydrite III
	Gypsum	Plaster of Paris	Insoluble Anhydrite
Decomposition temperature (°C)	> 120	> 200	1450
Density (g cm⁻³)	2.31	α: 2.76	2.96
		β: 2.62	
Molar mass (g mol⁻¹)	172.17	145.15	136.14
Crystal water (wt-%)	20.9	6.21	0.00

Table 2-3 shows that the calcium sulfates differ in density, with the anhydrite possessing the highest density and the dihydrate the lowest. As expected, the dihydrate has the highest molar mass while the anhydrite, containing no additional water, has the lowest molar mass.

2.5. Comparison of aluminium and magnesium fuel

Aluminium is the most widely used metallic fuel in pyrotechnic compositions, which is closely followed by magnesium (Conkling, 1985). Aluminium is often used since it is relatively inexpensive, lightweight and available in a variety of particle shapes and sizes including flakes and atomised forms (Conkling, 1985). The atomised form is spherical in shape. It has a lower specific surface area and consequently a lower reactivity than the flake form. The batch to batch performance of the spherical form is more reproducible. It is therefore preferred in military applications where it is used to produce heat and light (Conkling, 1985). On the other hand, flaked aluminium is preferred by the fireworks industry where it is used to produce bright white sparks since the larger surface area makes it more reactive and sensitive to ignition (Conkling, 1985). Furthermore, aluminium is stable and safe when it is stored. Aluminium particles have an outer oxide coating that is non-porous and highly cohesive (Jennings-White & Kosanke, 1995). This coating needs to be disrupted for a reaction to occur and this raises the activation energy required (Jennings-White & Kosanke, 1995). Pyrotechnic compositions containing aluminium can be considered safe since they are less likely to undergo accidental ignition or corrosion (Jennings-White & Kosanke, 1995). However, hazards may arise if the oxide coating is disrupted.

Metals are capable of reacting with water to produce hydrogen, which is also the case for aluminium. The reaction is exothermic and poses the hazard of producing enough heat to induce an accidental ignition or corrosion of the metal (Jennings-White & Kosanke, 1995). Figure 2-8 shows the reaction between 12 µm-sized atomised aluminium with distilled water, both components of 2 g each.
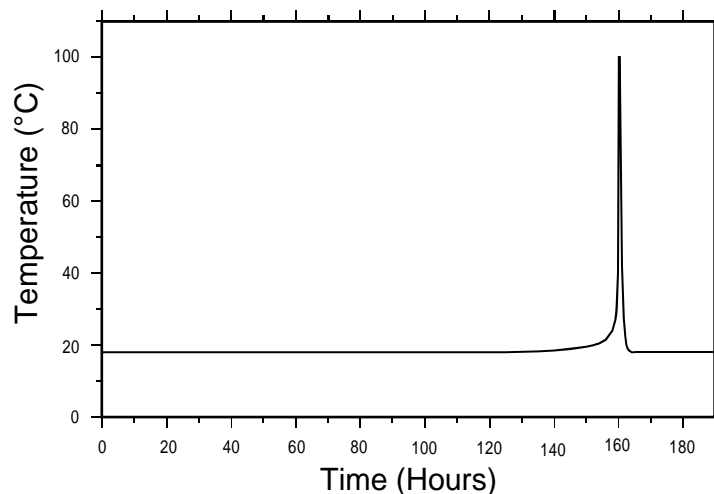
Figure 2-8: Exothermic reaction between aluminium and water (Jennings-White & Kosanke, 1995)

Figure 2-8 shows that the reaction is slow, only producing an exotherm after 159 hours. It has been reported that this is not a serious problem with atomised or flaked aluminium (Jennings-White & Kosanke, 1995). However, moisture must be avoided in formulations including nitrate oxidisers since the exothermic reaction between aluminium, water and potassium nitrate is capable of autoignition in confined spaces (Conkling, 1985).

On the other hand, magnesium is a very reactive metal and makes a good fuel in pyrotechnic compositions under certain conditions (Conkling, 1985). It burns with a bright white light. The activation energy required for a reaction with magnesium is much less than aluminium, making it easier to ignite (Jennings-White & Kosanke, 1995). Magnesium is oxidised by moist air and readily reacts with even weak acids (Conkling, 1985). However, magnesium reacts so greatly with water that they are considered incompatible (Jennings-White & Kosanke, 1995). Similarly, magnesium reacts readily with copper salts and they are considered incompatible (Jennings-White & Kosanke, 1995). This is because copper and magnesium form an electrochemical couple and undergo an exothermic displacement reaction (Jennings-White & Kosanke, 1995).

Table 2-4 shows a comparison of aluminium and magnesium properties.

Table 2-4: Properties of Aluminium and Magnesium (Conkling, 1985)

Property	Aluminium	Magnesium
Atomic weight (g mol^{-1})	27	24.3
Melting point (°C)	660	649
Boiling point (°C)	2467	1107
Heat of combustion (MJ kg^{-1})	130	103
Combustion product	Al_2O_3	MgO
(g fuel consumed per g O)	1.12	1.52

Magnesium has a significantly lower boiling point than aluminium (1107 °C vs 2467 °C). This will allow excess magnesium to vaporise and provide additional heat to the composition (Conkling, 1985).

2.6. Effect of density

An interesting finding was made by Pantoya & Granier (2005) when they compared the burn rates of pelletized thermite containing micron- and nano-sized aluminium fuel particles. The density of the thermite was varied and thereafter burn rates measured, as shown in Figure 2-9.
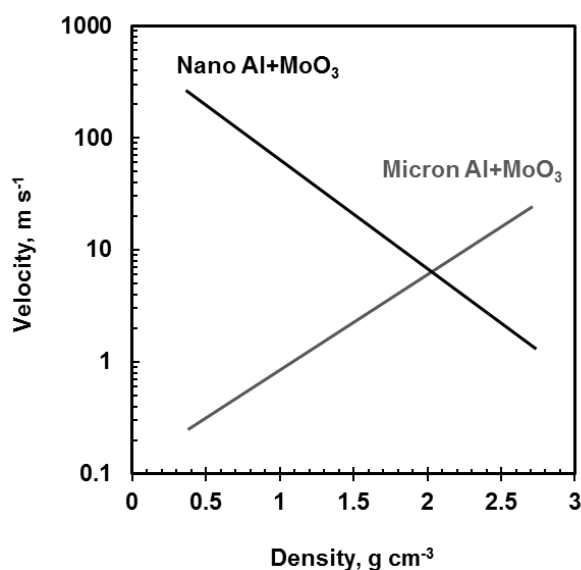
Figure 2-9: Comparison of combustion velocities for nano- and micron-sized thermite with varying densities (adapted from Pantoya & Granier, 2005)

It was found that as the density was increased, the burn rates of the thermite-containing micron-sized aluminium increased. Conversely, the burn rate of the thermite containing nano-sized aluminium decreased with an increase in density. The opposing trends observed in Figure 2-9 was explained by the manner in which flames propagate for each composition (Pantoya & Granier, 2005).

Figure 2-10 shows Differential Scanning Calorimetry (DSC) plots for each composition.
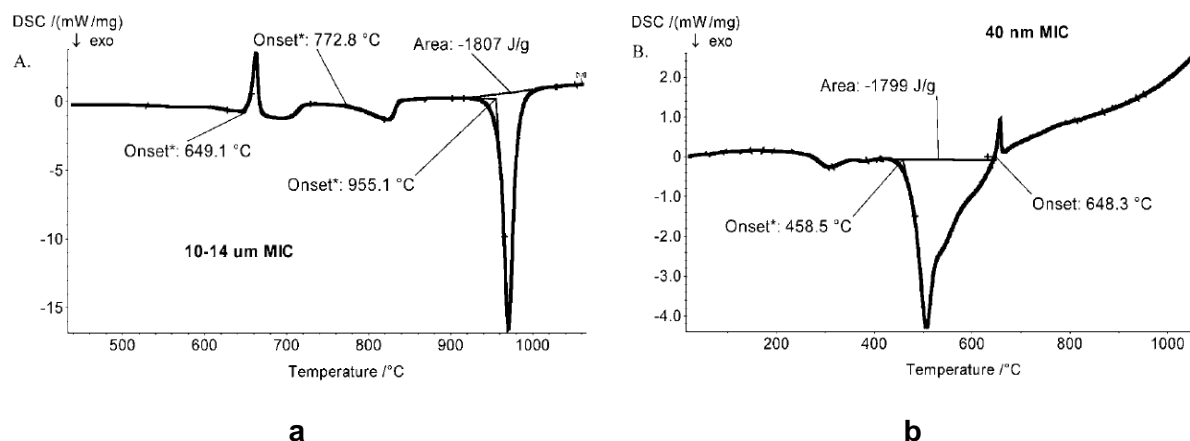
Figure 2-10: DSC plots comparing (a) micron-Al with MoO_3 with (b) nano-Al with MoO_3 (Pantoya & Granier, 2005)

Figure 2-10a shows a diffusion reaction dominates after the reactants change phase in the micron-sized composition. Increasing the density of the pellet reduces the volume of air voids between particles, increasing the thermal diffusivity and combustion velocities (Pantoya & Granier, 2005). Figure 2-10b shows the rate is initially controlled by the oxidation of solid aluminium for the nano-sized composition. The reaction then propagates through faster liquid-solid/liquid-gas diffusion mechanisms. The increased density by pressure applications induces a pre-combustion of the nano-aluminium, leaving less energy to promote higher combustion rates (Pantoya & Granier, 2005).

2.7. Additives considered for sulfate-based thermite compositions

It was assumed that the presence of pores would result in an inconsistent burn rate. It was suggested that the inclusion of additives could limit voids created by evaporation of water when casting. An open-cell porous structure could be filled by dropping a liquid oxidiser solution onto the structure (du Plessis, 2014). The solvent will remain trapped in the pores as the solute evaporates away. Alternatively, the additive may be included in the base material before casting so that it may fill the pores between particles.

2.7.1. Sulfur

The inclusion of a binder material possessing a low melting point within the powder thermite composition, such as sulfur, was suggested. Once the material is cast, it can be placed into an oven where the binder will melt and fill pores within the structure, without influencing the fuel or oxidiser particles.

There are various allotropes or forms of sulfur. The chemical and physical properties of sulfur differ and this is largely dependent on its temperature history (Meyer, 1976). The most stable form of sulfur is cyclooctasulfur, of which there are α, β and γ allotropes (Meyer, 1976). Monoclinic sulfur is obtained if a sample of sulfur is heated to just above its melting point before allowing it to slowly cool and crystallise (Thompson, 2009). Alternatively, plastic sulfur can be obtained if a sample of sulfur is heated to its boiling point and thereafter quickly cooled in water (Thompson, 2009). Rhombic sulfur can be obtained by dissolving a sample of sulfur with warm solvent and thereafter allowing the solvent to evaporate (Thompson, 2009). The melting point of sulfur is between 118 – 120 °C while it is insoluble with water (Sigma-Aldrich, 2015).

2.7.2. Copper sulfate pentahydrate

Copper sulfate pentahydrate ($CuSO_4 \cdot 5H_2O$) is one of the most widely used copper compounds because of its availability and cost (Richardson, 2012). The blue crystals can be ground to a light blue powder. Upon thermal treatment, the water of hydration are progressively lost, forming anhydrous copper sulfate ($CuSO_4$) at 245 °C. It converts to copper oxide (CuO) at temperatures between 600 – 650 °C.

Thermal analysis of copper sulfate pentahydrate has shown its decomposition to be as follows (Richardson, 2012),

$$CuSO_4 \cdot 5H_2O \xrightarrow{88\ °C} CuSO_4 \cdot 3H_2O \xrightarrow{114\ °C} CuSO_4 \cdot H_2O$$
$$\xrightarrow{245\ °C} CuSO_4 \xrightarrow{340\ °C} Cu(OH)_2 \cdot CuSO_4 \xrightarrow{600-650\ °C} CuO$$
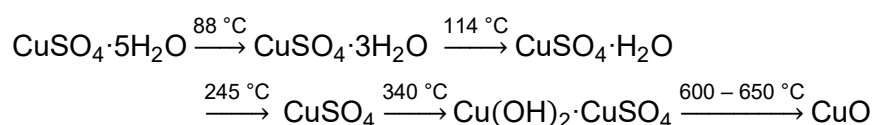
Copper sulfate pentahydrate dissolves in water, forming the hexaaqua(II) complex $[Cu(H_2O)_6]^{2+}$ (Zhang & Richardson, 2016). This dissolution process is endothermic, requiring a heat of solution of 0.662 MJ kg^{-1} water (Poling et al., 2008). Copper sulfate pentahydrate has a density of 2.28 g cm^{-3} and melts at approximately 110 °C (Sigma-Aldrich, 2016). Anhydrous copper sulfate can be prepared by the controlled heating of the pentahydrated form at 250 °C. Since $CuSO_4$ is extremely hygroscopic, absorbing moisture in air at temperatures < 30 °C to form $CuSO_4 \cdot 5H_2O$, it is often used as a dessicant (Richardson, 2012). The heat of solution for $CuSO_4$ is exothermic, releasing 2.70 MJ kg^{-1} water (Poling et al., 2008).

2.7.3. Sodium borosilicate glass spheres

Hollow glass spheres are a waterproof filler that can be used to decrease the density of a compositions. It is recommended that a maximum of 30 wt-% glass spheres be added to resin systems (AMT Composites, 2017). The siloxane coating of the glass spheres starts decomposing at temperatures > 150 °C while the melting point will be reached at > 350 °C (PQ Hollow Spheres, 2006).The glass spheres possess a bulk density of 1.14 g cm^{-3} (PQ Hollow Spheres, 2006).

2.7.4. Urea

At 20 °C, the solubility of urea in water is 51.6 g urea per 100 g of solution (Mavrovic et al., 2000). Urea reacts with gypsum in the presence of water forming the complex $CaSO_4 \cdot 4CO(NH_2)_2$ (Whittaker et al., 1933). The melting point of compound is between 132 − 135 °C and it has a density of 1.34 g cm^{-3} (Sigma-Aldrich, 2014).

2.8. Particle packing theory

The way particles pack may significantly influence the properties of the material. The packing density (ϕ) refers to the ratio of the volume of solids to the total volume occupied by the particles shown mathematically as follows,

$$\phi = \frac{V_s}{V_t} = \frac{V_s}{V_s + V_v} = 1 - \varepsilon \qquad (19)$$

Where, ϕ is the packing density (-), V_s and V_v are the volume of solids and voids respectively (m^3). The total volume is given by V_t (m^3) while the porosity is ε (-). Particle models are based on the assumption that smaller particles fill the spaces between larger particles, which is shown in Figure 2-11. In this way, the void fraction is reduced or the packing density is increased since the spaces between particles are filled with smaller particles (Mangulkar & Jamkar, 2013).
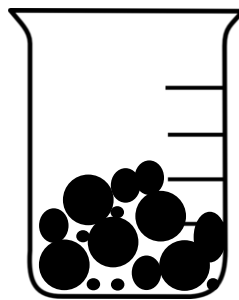
Figure 2-11: Depiction of packing density

Packing models can be described as either discrete or continuous. The discrete model assumes that the each particle will pack to its maximum density (Mangulkar & Jamkar, 2013). It can further be separated into binary, ternary and multimodal mixture models. The continuous model assumes that every possible particle size is present in the distribution (Mangulkar & Jamkar, 2013). Furnas (1931) was one of the first to develop packing theory based on spherical shaped particles. He assumed that smaller particles filled the spaces created between larger particles, without disturbing the packing of the larger particles (Mangulkar & Jamkar, 2013).

Furnas considered the ideal packing of a mixture of two different materials and, depending on the size of particles that are present, two cases were considered:
- "Fine grain dominant" where the volume fraction of small particles is large and
- "Coarse grain dominant" where the volume fraction of coarse particles is large.

These two cases are only possible if there is a large difference between the diameters of each particle; in other words, the condition of $d_1 << d_2$ should be met (Mangulkar & Jamkar, 2013). The diameter ratio (d_1/ d_2) should be considered if this condition is not satisfied. If $d_1 \sim d_2$, then either an interaction effect such as a wall or loosening effect may be experienced.

A wall effect is when a single coarse particle lies between many fine particles, resulting in a disturbance of the packing density of the fines (Mangulkar & Jamkar, 2013). A loosening effect is essentially the opposite of a wall effect. This occurs when a single fines particle lies between many coarse particles (Mangulkar & Jamkar, 2013). It results in a disturbance of the packing density, since the smaller particle is too large to fit between the voids between the coarse particles. Figure 2-12 is a representation of a wall effect and a loosening effect.
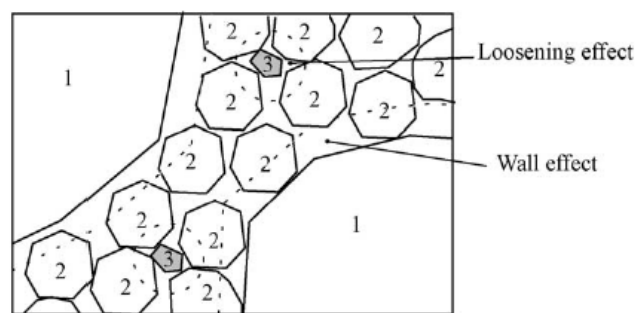
Figure 2-12: Packing density showing a wall effect and a loosening effect (Mangulkar & Jamkar, 2013)

Einstein's equation describes the relative viscosity for uniform-sized spherical particles

$$\eta_r = 1 + 2.5\phi \tag{20}$$

Where, η_r is the relative viscosity of the suspension relative to the neat liquid (-) while ϕ is the volume fraction (-). The Krieger-Dougherty equation (Krieger, 1972) expands on Einstein's equation but includes the maximum volume fraction, which is defined as the fraction of the dispersed phase that tends to an infinite viscosity

$$\eta_r = \left(1 - \frac{\phi}{\phi_{max}} \right)^{-[\eta]\phi} \tag{21}$$

Where, $[\eta]$ is the intrinsic viscosity and ϕ_{max} is the maximum dimensionless volume fraction corresponding to the random packed bed situation (where viscosity tends to infinity).

2.9. Characterisation techniques

2.9.1. Elemental composition

X-ray fluorescence (XRF) is a method used to determine the elemental composition of a sample. This is achieved when a sample is bombarded with high-energy but short-wavelength X-rays. Electrons are temporarily excited to a higher energy level, thereafter releasing characteristic X-ray (fluorescence) emissions when returning to ground state (Skoog et al., 2007).

2.9.2. Compound composition

X-ray diffraction (XRD) is a chemical analysis method used to determine the crystalline phase composition of a sample (Particle Analytical, 2016b). An X-ray beam of a defined wavelength (λ) is directed at a crystalline sample at an angle of θ. The samples produces a corresponding beam that is diffracted away from the sample at the same angle. In this way, the three-dimensional structure of a sample can be deduced. Diffraction from well-defined crystallographic planes results in constructive and destructive interference of the scattered radiation (Skoog et al., 2007). This phenomenon can be explained by Bragg's law, which is depicted by Figure 2-13.
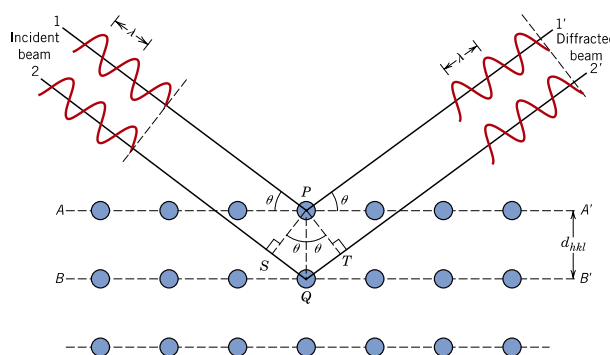
Figure 2-13: Bragg diffraction (Callister & Rethwisch, 2010)

Bragg's Law describes the conditions for constructive interference

$$n\lambda = 2d\ sin\theta \qquad (22)$$

Where, n is an integer (-), λ is the wavelength of the beam (nm), d is the interplanar distance of the crystal (nm) and θ is the angle of the incident beam (°).

Rearranging Equation 22 gives the condition required for constructive interference to occur; destructive interference will occur at all other angles.

$$sin\theta = \frac{n\lambda}{2d}$$

Results from XRD are shown in a diffractogram, which is a plot of intensity/counts as a function of diffraction angles (Particle Analytical, 2016b). Crystalline materials produce well-defined peaks; high-quality materials are shown by sharp peaks while poor-quality materials result in less well-defined peaks (Skoog et al., 2007).

2.9.3. Particle size distribution

The particle size distribution of a sample may be determined using various techniques, however for many of them it is common to suspend the particles in a fluid in which they are insoluble (Skoog et al., 2007). This ensures that there is a uniform concentration of the sample present before adding it to the sizing instrument while also preventing coagulation or agglomeration of particles (Skoog et al., 2007). An example of such an instrument is a Mastersizer, which functions on the principle of laser diffraction. A laser beam is passed through a sample and individual particles scatter the light depending on their size (Malvern Instruments Ltd, 2017). Large-sized particles scatter light at small angles to the laser beam while the opposite is true for small-sized particles, which scatters light at large angles to the laser beam (Malvern Instruments Ltd, 2017). The different angular intensities of the particles create a scattering pattern. The Mie theory of light scattering, assuming a spherical-shaped particle, is used to calculate the particle size in the Malvern Mastersizer 3000.

2.9.4. Morphology and shape

Scanning electron microscopy (SEM) is a technique that provides high-resolution information on the external morphology of material surfaces (Skoog et al., 2007). A beam of electrons is directed onto a sample, thereafter the reflected (or back-scattered) electrons are collected in a cathode ray tube (CRT) to produce an image (Callister & Rethwisch, 2010). Non-conductive samples are coated with a very thin metallic coating to ensure that the sample is electrically conductive (Callister & Rethwisch, 2010). Field Emission Scanning Electron Microscopy (FESEM) uses a field emission gun that provides a focused low-energy beam of electrons that produces an image with a higher resolution than conventional SEM (Universitat Politècnica de València, 2012).

2.9.5. Density and porosity

Density *(ρ)* is broadly defined as mass *(m)* over volume *(V)*, as shown in Equation 23

$$\rho = m/V \tag{23}$$

A pycnometer is an instrument that can be used to determine the density of materials. It is a flask that can be filled to a specific volume since it has a glass stopper that can remove excess volume (Blake, 2008). It is suitable for both porous and non-porous materials. Equation 24 can then be used to determine the density.

While the mass of an object can easily be determined, it is not as straightforward to determine volume. This is since the definition of volume varies slightly due to the inclusion or exclusion of pores within the material. Surface irregularities create different types of pores as shown in Figure 2-14.
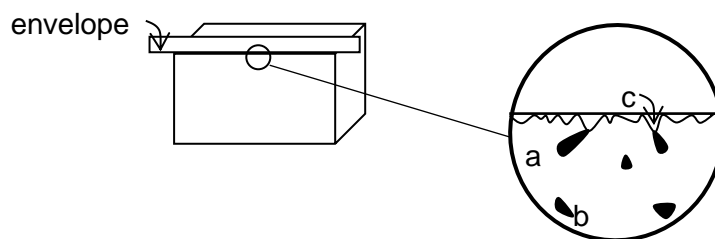
Figure 2-14: Surface irregularities showing (a) open pores, (b) closed/blind pores and (c) external voids (adapted from Webb, 2001)

Figure 2-14a shows that open pores are connected to the surface while closed/blind pores are inaccessible from the surface as seen in Figure 2-14b (Webb, 2001). Furthermore, surface irregularities can create external voids that are defined as the space between the envelope and surface (Webb, 2001). Additionally, there exists spaces between the solid granular/powder material that are interparticle voids. Taking these pores and voids into account results in varying descriptions for volume, consequently resulting in numerous classifications of density.

The various definitions for volume are summarised in Table 2-5, which shows the volumes that are included in each definition.

Table 2-5: Definitions of different volumes

Definition	Volume included in definition				
	Solid material	Open pore	Closed pore	Interparticle void	External void
Apparent volume	X	X	X	X	
Bulk volume	X	X	X	X	X
True volume	X				

Table 2-5 shows that the apparent volume is the total volume of the solid material including all sub-surface pores and voids but excluding external voids. Bulk volume, on the other hand, is the total volume including all pores and voids. The true volume of a sample includes only the volume of the solid material. Thus, the apparent density is calculated using the apparent volume. This is the volume that includes all sub-surface pores and spaces. Similarly, the bulk density is calculated using the bulk volume, which takes all pores and spaces into account. The true density is calculated using the true volume. The tap density is the bulk density of a sample after it has been vibrated to obtain an optimum arrangement of particles.

In theory, the porosity of a sample can be calculated using volumes as shown in Equation 24

$$Porosity = 1 - \frac{Volume\ of\ solids}{Total\ volume} \tag{24}$$

Experimentally, the porosity can be calculated using the concept of saturation shown in Equation 25

$$Porosity = \frac{Pore\ volume}{Total\ volume} \tag{25}$$

This can be achieved by adding a powder sample into a measuring cylinder. Thereafter, water of volume V_1 is added to just above the sample. After some time, the new volume V_2 is recorded. The difference between these volumes is the pore volume,

$$Pore\ volume = V_1 - V_2 \tag{26}$$

2.9.6. Specific surface area

The specific surface area (m^2 g^{-1}) of a sample may be determined using a Brunauer, Emmett and Teller (BET) instrument. In addition, the instrument may also determine the pore size distribution of a sample. A schematic diagram of the instrument is shown in Figure 2-15.
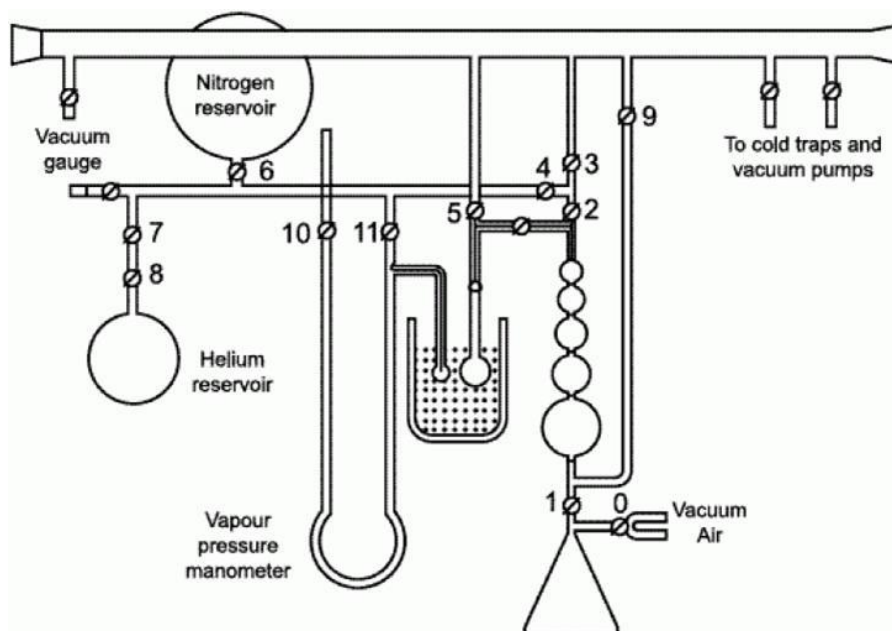
Figure 2-15: Schematic diagram showing the dynamic flow method used in BET instrument (Particle Analytical, 2016a)

Samples of approximately 1 – 2 g are prepared under a vacuum at higher temperatures in order to remove any gases remaining on the surface of the particles (Particle Analytical, 2016a). The vacuum may be applied by purging the system with an inert gas such as nitrogen while the higher temperatures may assist with the speed at which the impurities are removed (Particle Analytical, 2016a). Care should be taken to conduct the de-gassing at a temperature that will not alter the sample in any way. After this process, the mass of the sample is recorded. The sample is then lowered into a Dewar vessel containing liquid nitrogen. A certain volume of gas is allowed to enter the tube and the volume of the adsorbed gas (V_a) is measured. BET theory is the used to determine the specific surface area of the sample.

Brunauer, Emmett and Teller first developed BET theory, which is based on the physical adsorption of a gas on the surface of a solid. The amount of adsorbed gas is proportional to the monomolecular layer of gas on the surface of the solid (Particle Analytical, 2016a). The volume of adsorbed gas can be measured by either dynamic flow or volumetric flow gas adsorption methods.

The Brunauer, Emmett and Teller (BET) adsorption isotherm equation is

$$\frac{1}{V_a\left(\frac{P_0}{P} - 1\right)} = \left(\frac{C - 1}{V_m \, C}\right)\left(\frac{P}{P_0}\right) + \frac{1}{V_m \, C} \tag{27}$$

Where, V_a is the volume of adsorbed gas at STP (at 0 °C, 1 atm) (cm^3) while V_m is the volume of adsorbed gas at STP producing a monomolecular layer on the sample surface (cm^3). The saturated pressure of the adsorbate gas is given by P_0 (Pa) and the partial vapour pressure of the adsorbate gas in equilibrium with liquid nitrogen surface is given by P (Pa). A dimensionless constant is represented by C.

Three different measurements of V_a are recorded for three different P/P_0 values. Since Equation 27 can be likened to a straight line (Equation 8), $1/V_a(P/P_0 - 1)$ can be plotted against P/P_0. The slope (m) and y-intercept (c) of this straight line correspond to $m = (C - 1) / (V_m \, C)$ and $c = 1 / (V_m \, C)$.

The values of the slope and intercept from the plotted straight line can be used to determine V_m and C. The volume of the gas adsorbed (V_m) can be determined by

$$V_m = \frac{1}{Slope + Intercept} \tag{28}$$

The constant (C) in the BET adsorption isotherm equation can be determined by

$$C = \frac{Slope}{Intercept} + 1 \tag{29}$$

Using the calculated V_m, the specific surface area can thereafter be obtained

$$S = \frac{V_m \, N \, a}{V \, m} \tag{30}$$

Where, S is the specific surface area (m^2 g^{-1}), N is Avogadro's constant (6.022 x 10^{23} mol^{-1}), a is the cross sectional area of one adsorbate molecule (0.162 nm^2 for nitrogen) and m mass of the powder (g).

2.9.7. Organic and inorganic groups

Fourier Transform-Infrared Spectroscopy (FTIR) is able to characterise organic and, in some cases, inorganic substances. FTIR determines the extent to which infrared radiation is absorbed by materials at a range of wavelengths, thus identifying structures molecular components within the materials (Materials Evaluation and Engineering, 2001). This is achieved when the absorbed radiation excites molecules to higher vibrational states within the sample, thereafter releasing light at a particular wavelength that corresponds to the samples chemical structure (Materials Evaluation and Engineering, 2001). Wavenumbers (cm^{-1}), the inverse of wavelengths (cm), are plotted for convenience. Structural features such as the backbone or functional groups of a molecule can be identified by characteristic absorptions produced in the spectra (Coates, 2000). The fingerprint region in the range between $400 - 1500$ cm^{-1} is used to identify unknown samples while absorption bands between $1500 - 4000$ cm^{-1} are used to determine functional groups within a sample.

The Universal ATR attachment to a FTIR machine is able to characterise liquid and hard solid samples by analysing samples placed on the surface of a crystal while a force gauge allows reproducibility between samples (Perkin Elmer, 2005). Radiation is passed through a crystal, on which a sample is placed, thereafter undergoing total internal reflectance (Perkin Elmer, 2004). A part of the wave may travel through the crystal reaching the sample, where any absorption will produce a spectrum characteristic of the sample material. Some irregular-shaped solids may have poor contact with the crystal and thus results may vary (Perkin Elmer, 2004).

2.9.8. Heat of hydration

The hydration of calcium sulfate hemihydrate ($CaSO_4 \cdot 0.5H_2O$) to calcium sulfate dihydrate ($CaSO_4 \cdot 2H_2O$) is a slightly exothermic process. The hydration heat of a calcium sulfate hemihydrate-lime-metakaolin-water system was determined by Tydlitát et al. (2015) using an isothermal heat flow calorimeter. It is based on measurements of heat flow in a hydrated sample that is compared with that of a reference sample undergoing no hydration (Tydlitát et al., 2008). Samples of 0.8 g were placed into copper vessels in a heat calorimeter sealed with an insulated cover. The temperature was allowed to stabilise for an hour before water was added to the samples. Plastic tubules were used to mix the powders into a paste and the copper vessels were thereafter sealed by a resin plug. The calorimeter was closed with an insulated cover and the recording of voltage data (mV) was started to run for 20 h. The data was then multiplied by the calibration constant determined in each run, before determining the specific hydration heat power N (mW g^{-1}) and specific hydration heat Q (J g^{-1}).

2.9.9. Compressive strength

Standard test methods described for determining the compressive strength of cylindrical concrete samples include applying an axial load to a sample at a rate, based on the size and elastic modulus of the material, until the sample breaks (ASTM, 2017). The compressive strength can be calculated by dividing the maximum load obtained at failure by the cross-sectional surface area of the cylindrical sample (ASTM, 2017). It should be noted that the compressive strength obtained is highly dependent on sample preparation methods such as mixing, moisture conditions and the size of the sample.

Typical fracture patterns that may be obtained at a load failure are shown in Figure 2-16.
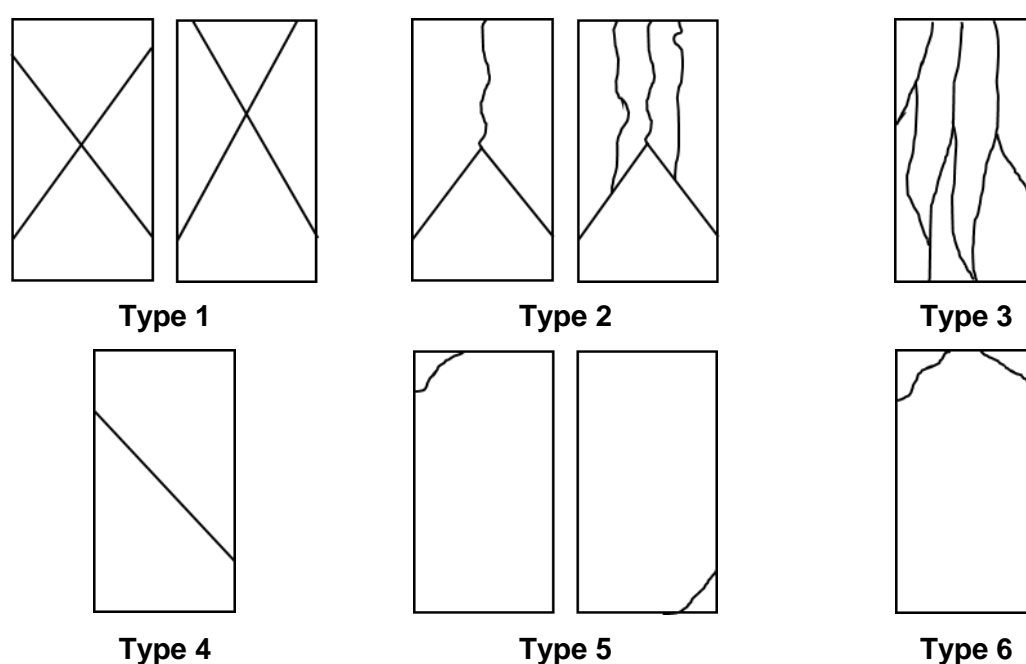
Figure 2-16: Typical fracture patterns at load failure (ASTM, 2017)

Figure 2-16 shows that Type 1, Type 2, Type 3 and Type 4 patterns are well-defined indicating cone, cone and split, columnar and shear fractures in each respectively. Type 5 and Type 6 fractures may be obtained before the final capacity of the sample is reached (ASTM, 2017). Type 1 shows well-formed cones on both ends of the cylinder while Type 2 shows a single well-formed cone with vertical cracks running to the other end. Type 3 displays vertical cracking through both ends of the cylinder with no cones present and Type 4 shows a diagonal fracture not reaching both ends with no cones present.

2.9.10. Energy output of a thermite composition

Oxygen bomb calorimeters are typically used to measure the calorific value of solid and liquid combustible samples by comparing the heat of combustion of a sample to that of a standard material with known calorific value (Parr, 2007). A schematic of the bomb calorimeter setup is shown in Figure 2-17.
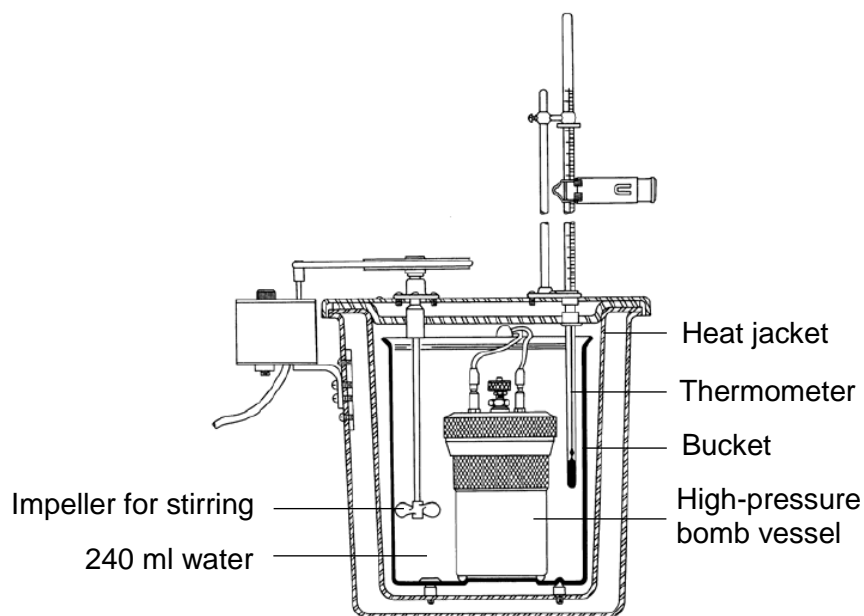
Figure 2-17: Oxygen bomb calorimeter setup (Parr, 2007)

Samples are burned in a high-pressure (typically oxygen) atmosphere in a metal vessel or bomb. A pressure range of between 20 – 35 atm is recommended (Parr, 2007). The bomb vessel is contained in a bucket with a known volume of water, with a surrounding heat jacket and thermometer to measure temperature changes within the bucket (Parr, 2007). Furthermore, electrodes ignite samples by passing a current through a fuse wire that is in contact with the sample. The burning of the fuse wire contributes towards the heat recorded for the system and should be accounted for after tests are completed.

Conducting the bomb calorimetry tests in an inert atmosphere would be beneficial to determine the energy output of the systems in isolation. Tichapondwa et al. (2015) ran anhydrous calcium sulfate and silicon ($CaSO_4$-Si) systems in a 3.0 MPa helium environment. Furthermore, the systems required approximately 2 g of starter in addition to electrically heated nichrome wire to assist with ignition (Tichapondwa et al., 2015).

2.9.11. Differential thermal analysis

Thermal analysis detects the physical and chemical changes of materials as a function of temperature (Materials Evaluation and Engineering, 2001). Differential thermal analysis measures the temperature difference between a sample material and a reference material under the same conditions (Bhadeshia, 2002). Figure 2-18 shows the main features of differential thermal analysis, including sample holders for the sample and reference materials containing thermocouples, a furnace, a temperature programmer to control the heating rate and a recording system (Bhadeshia, 2002).
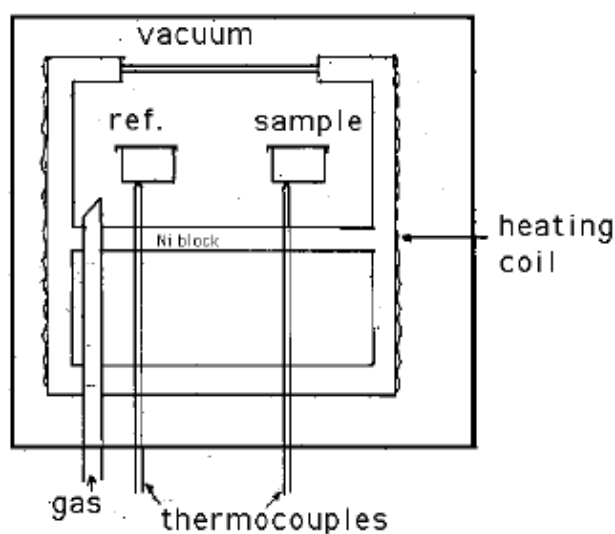
Figure 2-18: Differential thermal analyser setup (Bhadeshia, 2002)

An endotherm is produced if the sample temperature is less than the standard material and ΔT is negative. Examples of endothermic reactions include dehydration, fusion, evaporation amongst others (Tan et al., 1986). On the other hand, an exotherm is produced if the sample temperature exceeds that of the standard material, resulting in a positive ΔT. Examples of exothermic reactions include oxidation, crystalline formation and selected decomposition processes (Tan et al., 1986).

2.10. Hypothesis

The Council for Scientific and Industrial Research (CSIR) is currently working on developing metal-cutting thermites, where calcium sulfate is used as a suitable inorganic binder in the energetic material. It was of interest to determine the energetic properties of the binder alone and its suitability for use in metal-cutting. EKVI thermodynamic simulations predicted that 40 wt-% aluminium fuel and 60 wt-% calcium sulfate dihydrate oxidiser would release an enthalpy of 4.56 MJ kg^{-1} thermite. It is hypothesised that, under bomb calorimetry conditions of 3.0 MPa O_2 and a 240 mL pressure vessel, this base case thermite would result in an energy output of 8.67 MJ kg^{-1} thermite. Given this energy output, and large predicted adiabatic temperature of 2800 °C, it is hypothesised that it might be suitable as a metal-cutting tool.

2.11. Key questions

The key questions that would assist in proving or disproving the hypotheses are:

- What is the optimum fuel to oxidiser ratio that will result in the largest adiabatic flame temperature?
- What is the density of the cast thermites?
- What is the minimum and maximum amount of water that will enable flowability and setting?
- How long does the cast thermite take to set?
- Are there additives that can increase the rate at which the cast sets?
- What is the heat of reaction upon casting?
- What is the strength of the thermite after casting and setting?
- What burn rates and maximum surface temperatures can be achieved by the cast thermites?
- What is the effect of density on the burn rate of the thermite?
- What products are formed from the reaction between fuel and oxidiser?
- What is the energy output of the thermites?
- Can the thermite be used to melt aluminium?

Chapter 3: Experimental methods

EKVI and FactSage thermodynamic simulations were run to determine the optimum fuel to oxidiser ratio and the maximum adiabatic temperature of various compositions. Raw materials were characterised. Laboratory tests were conducted to determine optimum water ratios when casting and the heats of hydration. Compressive strength was measured. Linear burn rates and maximum surface temperatures were determined. Burn residues were collected and analysed. The energy output of the thermite reaction was obtained.

3.1. EKVI and FactSage thermodynamic simulations

EKVI System is a computer programme that consists of EKVIBase, a thermochemical database of $3000 - 4000$ chemical compounds in gas and condensed phases. EKVICalc was used to compute equilibrium calculations upon the assignment of reaction criteria, which included specifying reactants, pressure or volume, temperature and possible products (Noläng, 1996). The mass of solid fuel and oxidiser was allowed to vary between 0.1 and 0.9 g since the system does not allow running 0 g of any substance. Each run was set to atmospheric pressure conditions at 1 atm. The "find maximum temperature" function was turned on since the temperature was not specified. Thereafter, the "auto-select-species" function was turned on before the calculation was run.

FactSage is a software that consists of multiple thermochemical databases, which includes FactPS (pure substances) and FToxid (FACT oxides) amongst others. The programme calculates equilibrium conditions by minimising the total Gibbs energy of the system (Bale & Pelton, 2015). The Equilib module was used, since it is suitable for multiphase and multicomponent equilibria calculations, and the FactPS database was chosen. An initial temperature of 25 °C and an atmospheric pressure of 1 atm were selected. Reactant amounts were varied between 0 and 1 g and starting phases were set to solid in the reactants window. In the menu window the product species for gas, pure liquids and pure solids were ticked. The mass increments in which the reactants should vary and pressure was set. The heat of reaction ΔH was set to 0, which indicates adiabatic conditions, before the calculation was run.

Simulations were run to determine the following optimum compositions:
- Base1, a base case of calcium sulfate and aluminium;
- Blend2, using a calcium sulfate blend as oxidisers with aluminium;
- S4, the addition of sulfur to the base case;
- CSP5, the inclusion of copper sulfate pentahydrate to the base case;

- GSB − GS5, base case with sodium borosilicate glass spheres and
- Base1, Blend2, S4, CSP5 with urea loadings in the casting water.

3.2. Characterisation of raw materials

3.2.1. Elemental composition

Aluminium, calcium sulfate hemihydrate, copper sulfate pentahydrate were prepared as boric acid powder briquettes while anhydrous calcium sulfate, calcium sulfate dihydrate, sulfur and sodium borosilicate glass spheres were prepared as pressed powders. Both preparation methods gave similar results, they only differed in sample preparation time. The ARL Perform'X Sequential XRF instrument with Uniquant software was used. The values were normalised, as no LOI was done to determine crystal water and oxidation state changes. Calcium sulfate hemihydrate and copper sulfate pentahydrate were also roasted at 1000 °C to determine Loss on Ignition (LOI). Thereafter, 1 g of the roasted sample was placed in a platinum or copper (Pt/Cu) crucible with 6 g lithium tetraborate ($Li_2B_4O_7$) and fused. The ARL Perform'X Sequential XRF instrument was used for the analyses. Analyses were executed using the Quantas software. Both Uniquant and Quantas software are able to analyse elements between sodium (Na) and uranium (U) on the periodic table, however only elements above their detection limits were reported.

3.2.2. Compound composition

XRD (X-Ray Diffraction) analysis was used for the phase and compound identification of the raw materials. This method was also used for analysis of burn residues collected from open air burn tests. Compound compositions were determined by analysing samples using a PANalytical X'Pert Pro powder diffractometer. It was in 2θ configuration with an X'Celerator detector and variable divergence with fixed receiving slits with Fe filtered Co-Kα radiation (λ = 1.789Å). The phases were identified using X'Pert Highscore plus software.

3.2.3. Particle size distribution and D$_{50}$

Particle size distributions were determined using a Malvern Mastersizer 3000 instrument. On the Mastersizer 3000 V3 software, non-spherical particles were chosen. Samples were loaded onto the system by assigning a name, refractive index and densities obtained from Material Safety Data Sheets. Water was the dispersant that is used with the Hydro LV unit. The background measurement and sample measurement duration were set to 20 s each and to record 5 measurements with a delay time of 10 s. The only exception was for calcium sulfate

hemihydrate and copper sulfate pentahydrate, since they dissolve/react with water. The delay time was set to 3 s to ensure a lower error between runs. The obscuration limit and stirrer speed were set to 2.0 – 20 % and 3360 RPM respectively. Volume distribution was chosen as the result type.

3.2.4. Particle morphology and shape

Samples were prepared for the Scanning Electron Microscope (SEM) by applying a conductive carbon coating using an EMITECH K950X. Thereafter, images were taken on a Zeiss Ultra Plus 55 SEM. An EHT (extra high tension) voltage level of 1 kV was used.

3.2.5. Specific surface area

Surface area and porosity were obtained using a Micromeritics Tristar II instrument. Samples were degassed for 5 hours at 40 °C in the Micromeritics Vac Prep 061 Sample Degas System. After degassing, the Dewar flask was filled with liquid nitrogen and the samples were secured onto the instrument. The samples were run until completion.

3.2.6. Infrared spectroscopy

Fourier Transform-Infrared Spectroscopy (FTIR) was conducted on a PerkinElmer Spectrum 100 using the Universal ATR attachment for surface analysis of samples. The Spectrum V10.03.06 software was used for analysis. Ethanol and paper towels were used to clean the diamond crystal. A background scan was performed before covering the crystal with the sample powder. The force gauge was adjusted to between 99 – 101 N. The sample was then scanned and a spectrum obtained. The spectra were then subjected to baseline correction and smoothening.

3.2.7. Differential thermal analysis

Thermal analysis was conducted using a Shimadzu DTA 50 Differential Thermal Analyzer on approximately 20 mg of crushed thermite composition in an alumina pan. Similarly, approximately 20 mg of alumina (Al_2O_3) standard was used. An inert atmosphere of argon at a flow rate of 20 mL min^{-1} was used. A heating rate of 50 °C min^{-1} was set to reach a maximum temperature of 1200 °C with a sampling rate of 1 s. Runs were repeated at least three times per composition. Onset temperatures of melting and the reaction were determined using the TA 60 software.

3.3. Obtaining optimum compositions

3.3.1. Method for determining optimum compositions and water loadings

Different water loadings were added to approximately 1 g calcium sulfate hemihydrate to investigate the effect on mixing and setting. The mole ratio of calcium sulfate hemihydrate ($CaSO_4 \cdot 0.5H_2O$) to water (H_2O) was varied randomly between 1:2 and 1:10 in casts without fuel. Compositions were mixed and allowed to set. These included aluminium fuel, calcium sulfate hemihydrate oxidiser as well as additive powders. The calcium sulfate hemihydrate in the composition was thereafter hydrated to form calcium sulfate dihydrate. Optimum fuel and oxidiser loadings obtained from EKVI simulations at the maximum adiabatic reaction temperature are listed below:

- Base1: 60 wt-% $CaSO_4 \cdot 2H_2O$, 40 wt-% Al
- Blend2: 30 wt-% $CaSO_4$, 30 wt-% $CaSO_4 \cdot 2H_2O$, 40 wt-% Al
- S4: 50 wt-% $CaSO_4 \cdot 2H_2O$, 20 wt-% S, 30 wt-% Al
- CSP5: 50 wt-% $CaSO_4 \cdot 2H_2O$, 10 wt-% $CuSO_4 \cdot 5H_2O$, 40 wt-% Al

The hydrated compositions were allowed to set. Observations on the setting of casts immediately after mixing and every hour after that for 4 h were made. A mole ratio higher than the best setting cast without fuel was chosen for future casting with fuel and additives, due to the added powders present.

3.4. Characterisation of thermite powders before casting

3.4.1. Method for determining bulk and tapped density

The powder thermite compositions of Base1, Blend2, S4 and CSP5 were weighed out individually and passed through a 125 µm aperture sieve. Compositions were as described in Section 3.3.1., where the calcium sulfate hemihydrate content would be hydrated to form the The powder was transferred into a glass vial by means of a funnel, making sure the powder was disturbed as little as possible. The glass vial was then sealed with a lid and tapped continuously from a constant height of approximately 3 cm above a straight base. The height of the powder was recorded on the vial at 0, 10, 50, 100, 150, 200 and 300 tap intervals. The optimum water mass for each composition was added to the vials, before being mixed. The height of the thermite paste was recorded on the glass vial, which was allowed to set for 2 – 3 days. Thereafter, the final height of the cast was recorded and the volume change upon setting determined. At least three repeats were conducted per Base1, Blend2, S4 and CSP5 composition. Bulk density was determined at the height at tap-0 while the packing density was determined at the height of tap-300.

3.5. Characterisation of thermite powders during casting

3.5.1. Experimental setup of heat calorimeter tests

The experimental setup of an isothermal heat calorimeter is shown in Figure 3-1,
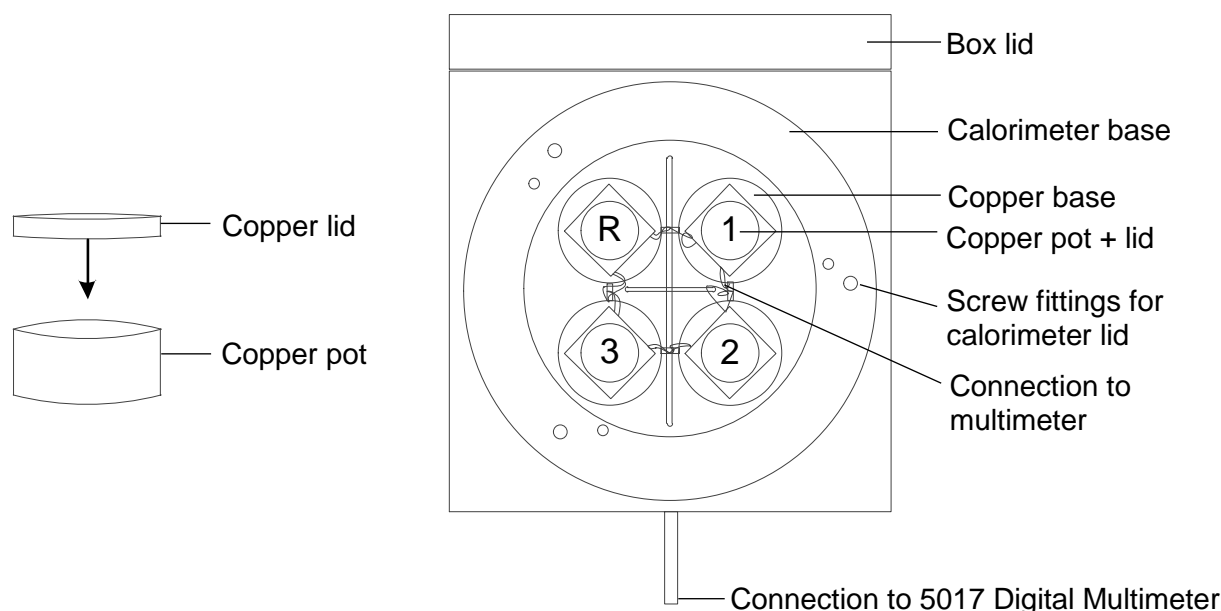
Figure 3-1: Experimental setup of heat calorimeter used for hydration heat tests

3.5.2. Method for determining hydration heat of reaction during casting

An isothermal heat flow calorimeter developed by Prof. H. Pöllmann at Martin Luther University of Halle-Wittenberg was used to determine the heat flow of the thermite systems, see Figure 3-1 setup. This was performed in a strictly temperature-regulated room at 21 °C. OMI MESICON software (Ecker, 2000) was used to record heat flow data (mW g^{-1}) every 15 s (Tydlitát et al., 2015) with an integration time of 2 s. Samples of 1 – 2 g thermite were placed in clean copper pots. Runs were performed in triplicate with an empty reference pot for each composition. The pots were placed in the heat calorimeter and the lids sealed with silicon paste. The heat calorimeter cover was then screwed shut before allowing the temperature to stabilise for 30 min. Thereafter, 1.0 – 1.5 g water was added to the thermite and mixed for about 1 min with a spatula until well-mixed. The pots were re-sealed and the heat calorimeter lid closed before running for 20 h (Tydlitát et al., 2015). This was repeated for each composition. The heat of hydration for each of the compositions Base1, Blend2, S4 and CSP5 were determined from the heat flow values obtained.

3.6. Characterisation of casts after setting

3.6.1. Experimental setup of compressive strength tests

Figure 3-2 shows the experimental setup used for compressive tests conducted with a 5 kN tensile tester.

5 kN load displaces 0.5 mm min^{-1}

Flat metal attachment

Cylindrical cast

Flat metal base attachment
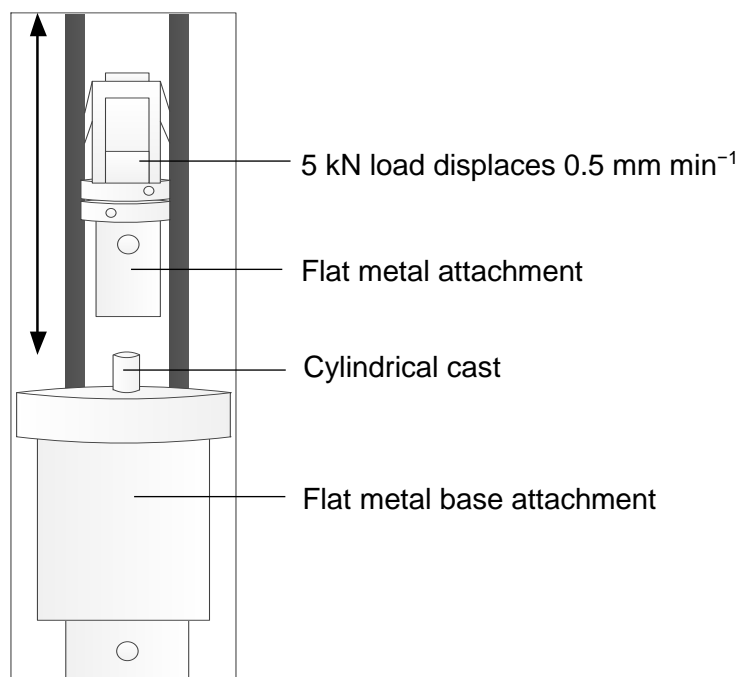
Figure 3-2: Experiment setup of 5 kN tensile tester for compressive tests

3.6.2. Method for determining compressive strengths of casts

Cylindrical shaped casts were made for compression tests using an LDPE pipe that had been cut into approximately 4 cm lengths. A slit was cut in the side of the pipes in order to facilitate easy removal of the casts. Sellotape was used to seal the slit. The bottom opening of the pipe was thoroughly sealed with a piece of plastic and tape. A sponge was used as a support structure to house the cylinder moulds. Thermite compositions were mixed with water and added to the pipe and allowed to set. See Section 3.7.2 for the method of casting used. After setting, the cylinders of thermite were removed and sanded down with fine sandpaper so that both the top and bottom surface were smooth, flat and also parallel to one another. The mass of the casts was recorded. A 5 kN LRX Plus tensile tester was used to determine compressive strengths, see Figure 3-2. A compression rate of 0.5 mm min^{-1} was chosen. The sample was placed between the base support and the load before moving the load very close to the sample but not touching. The compression of the sample was commenced and the machine was stopped as soon as the cast fractured. Compressive strength was determined using the first load at which the cast broke.

3.7. Casting of thermite

3.7.1. Casting samples for burn testing

Figure 3-3 shows the mould used and the experimental setup for casting samples initiated by different methods.

Cast mould   Thermite initiated with magnesium strip   Thermite initiated with barium nitrate sparkler
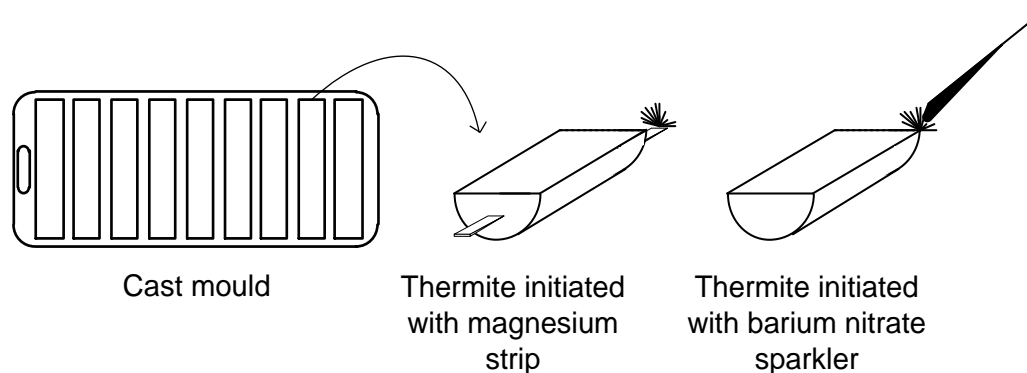
Figure 3-3: Casting procedure for burn test samples

3.7.2. Method for casting base case and compositions with additives

The mass of the raw material components of each thermite composition was calculated so that the final mass of the cast thermite was 5 g after setting. Thus, the mass of $CaSO_4 \cdot 0.5H_2O$ was calculated from the mass of $CaSO_4 \cdot 2H_2O$ that should be present in the 5 g cast based on Reaction 17. For convenience, bulk amounts of fuel and oxidiser powders for each composition were prepared by weighing and brushing through a 125 μm aperture sieve. The homogenous powder mixture was then weighed out individually from the bulk amount for each composition. The thermite powder was placed into a mould and the optimum mass of water was added. Optimum mole ratios of 1:10 calcium sulfate hemihydrate to water for Base1, S4 and CSP5 and 1:17 for Blend2 were used. The composition was mixed well with a spatula until a paste was formed. At least 4 casts were made per composition to check the repeatability of the performance. Casts were left in the fume hood to set for at least 3 days before being used in tests.

3.7.3. Method for casting low density compositions

The density of the casts were lowered in two ways: (a) by the inclusion of glass spheres, and (b) by adding excess water to the powder.

Glass spheres were added to a fixed amount of 5 g thermite made up of 60 wt-% $CaSO_4 \cdot 2H_2O$ and 40 wt-% Al. This resulted in compositions GSB, GS1, GS2, GS3, GS4 and GS5 where GSB was the control, containing 0 wt-% glass spheres, and GS5 contained 23 wt-% glass spheres. Aluminium and calcium sulfate hemihydrate powders were mixed with the glass spheres in a 750 W Pyramid spice grinder for 2 min. Water was then added to the powders and cast into a mould. The glass spheres casts were allowed 3 days to fully set and dry before being used for burn tests.

For the water addition experiments a constant 5 g of thermite, made up of 60 wt-% $CaSO_4 \cdot 2H_2O$ and 40 wt-% Al, was used. Aluminium and calcium sulfate hemihydrate powders were weighed, sieved and brushed through a 125 µm aperture. The homogenous powder mixture was then placed into a mould and the optimum water ratio was added to prepare Sample WR1. The process was repeated with excess quantities of water (Samples WR2 and WR3). After evaporation the excess water that was initially present produced additional pores within the base thermite cast. Like the glass spheres casts, the excess water casts were allowed to fully set and dry over a period of three days or more before being used for burn tests.

3.8. Burn tests

3.8.1. Experimental setup of burn tests

The experimental setup for the open air burn tests is shown in Figure 3-4.
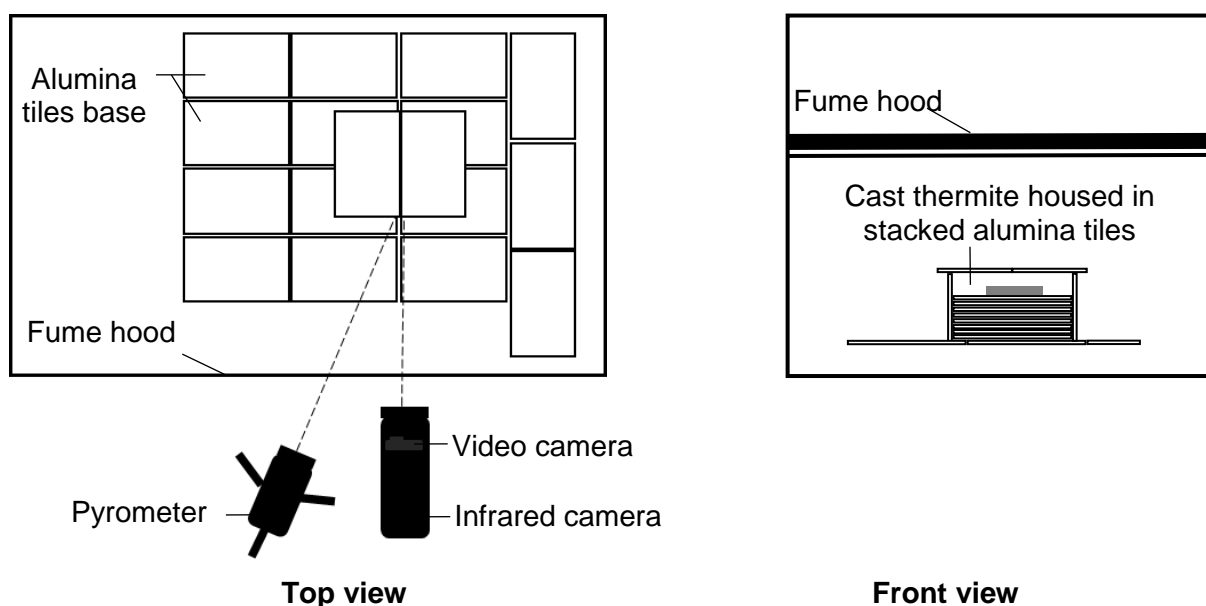
Figure 3-4: Experimental setup of open air burn tests

3.8.2. Method for open air burn tests

Open air burn tests were conducted in the fume hood located in the UP Pyrotechnics Laboratory. Alumina tiles were placed on the base of the fume hood on which 8 tiles of length and width 15 cm and 10 cm were stacked, as shown in Figure 3-4. More tiles were used to surround the stack of tiles in order to contain potential sputtering during the burn tests and to enable burn residue to be collected. This left an opening in the front of the tile-stack for placement of the cast. However, before proceeding, a photo was taken for designating the data to be recorded and the cast was then placed in the middle of the tile on the top of the stack. A Dias Infrared Systems Pyroview 380Lc/50Hz/30°x23° infrared (IR) camera and Raytek RAYMM1MHVF1L pyrometer were focussed on the middle part of the cast. The pyrometer was set to record temperature data points every 100 ms. Additionally, a PowerShot SX 260 HS camera was directed at the casts to obtain a video recording of the burns with the "movie digest" setting turned on. Safety gloves and glasses were worn. The fume hood was closed and the pyrometer programme was started. Next, the IR camera programme was set to start recording and the camera was turned on. A sparkler composed of barium nitrate was lit using a gas lighter and was used to ignite the sample. The camera and each of the programmes were stopped after the cast had finished burning. Observations of the test were recorded and burn residues collected. Burn rates were obtained from IR camera videos by dividing the cast length by the burning time. The burning time was obtained from when the sample was ignited to when the flame stopped propagating forward.

3.8.3. Safety, Health and Environment (SHE) assessment

Prior to the beginning of experimental work, an "Experimental and Safety Laboratory Report" was drawn up highlighting proposed experimental procedures, key hazards and safety measures. Raw materials were stored in a cool, dry, well-ventilated area in tightly sealed containers according to Material safety Data Sheet (MSDS) recommendations. Oxidisers and fuels were stored separately in the laboratory to prevent unplanned ignitions. None of the raw materials were disposed of down the drain; instead they were burnt with compositions. Burn residues were disposed of in a dustbin as they no longer posed a burning hazard. Personal protective equipment (PPE) including an anti-static cotton lab coat, dust mask, nitrile gloves, closed safety shoes and safety glasses were worn at all times. Casts were initially mixed without fuel and once a working method was obtained, fuel was added. Heat protective leather gloves and UV-protective safety glasses were used during burn tests. A safe distance away from the casts was maintained during burn tests. Alumina tiles were placed on the base of the fume hood to catch any sparks/sprays of thermite.

3.9. Determining energy output of compositions

3.9.1. Method for determining the energy output of thermites

The Parr 6200 bomb calorimeter and Parr 6510 water handling system were turned on. Next, the "calorimeter operation" was chosen on the bomb calorimeter interface. The operation mode of "determination" was selected. Thereafter, the "heater and pump" button was turned on so that the jacket temperature could reach a suitable temperature for testing. This took at least 20 min to reach so this step was started as soon as possible (Parr, 2010). Meanwhile, a helium gas supply was opened and set to 3.0 MPa (Parr, 2010). An inert gas was chosen so that only the energy of the thermite system could be obtained.

Samples of ~0.59 g were weighed in the sample pot. A combination of two different starter compositions were used to assist in igniting the calcium sulfate dihydrate-aluminium based thermite, since the nichrome wire alone does not possess enough energy to do so. Approximately 0.11 g Pb-SiO_2 and 0.21 g Al-Fe_2O_3 starter compositions were used. The Al-Fe_2O_3 starter was placed above half the test thermite. Next, roughly half the Pb-SiO_2 starter was poured next to the Al-Fe_2O_3 starter, making sure to overlap with each other. The nichrome wire was then connected so that it lay vertically in the thermite, ideally in the overlapping section of the starters. It was important to ensure that the nichrome did not touch the sample pot. The remaining Pb-SiO_2 starter was poured over the nichrome wire making sure that the wire was in contact with the starter to ensure ignition. The sample holder was placed carefully in the bomb vessel, which was thereafter sealed with a small amount of water in the lid. Once fully sealed, the helium attachment was connected to the bomb vessel and "O_2 fill" was pressed on the calorimeter interface.

The glass water flask must be filled before filling the calorimeter bucket. The tap was turned clockwise and, once the flask was full, then clockwise again to stop the water supply. The tap was turned clockwise again after the water level stabilised so as to empty the collected water into the calorimeter bucket. The bucket filled with water was then placed in the calorimeter using the indentations in the calorimeter as a guide as to which direction it should be placed. Next, the bomb was carefully placed over the circular indentation in the bucket. The electrodes were then carefully attached in place, ensuring that they were out of the way of the stirrer blades. Lastly, the calorimeter lid was closed and "start" was pressed. The name and mass of the sample was input and the run began. The calorimeter discharged a signal to indicate when ignition occurred. A misfire was reported in the event of the temperature rise being less than 0.5 °C (Parr, 2010). A gross heat value (MJ kg^{-1}) was recorded in the event of a successful run.

3.10. Determining the cutting ability of the cast thermite compositions

3.10.1. Experimental setup of metal-cutting tests

Figure 3-5 shows the procedure for preparing samples before proceeding with metal-cutting tests. Figure 3-6 shows the jig setup, indicating the placement of the prepared samples and aluminium blocks in metal-cutting tests.
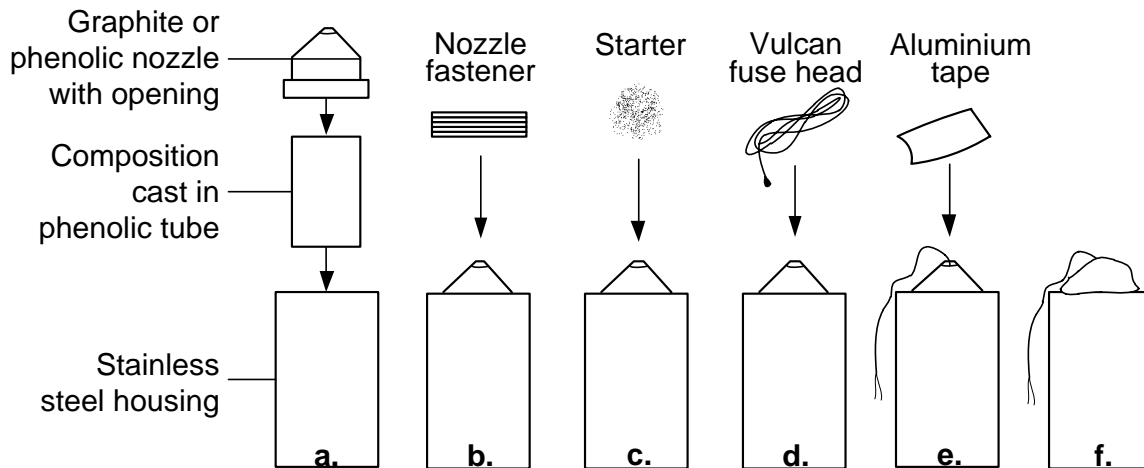
Figure 3-5: Sample preparation for metal-cutting tests
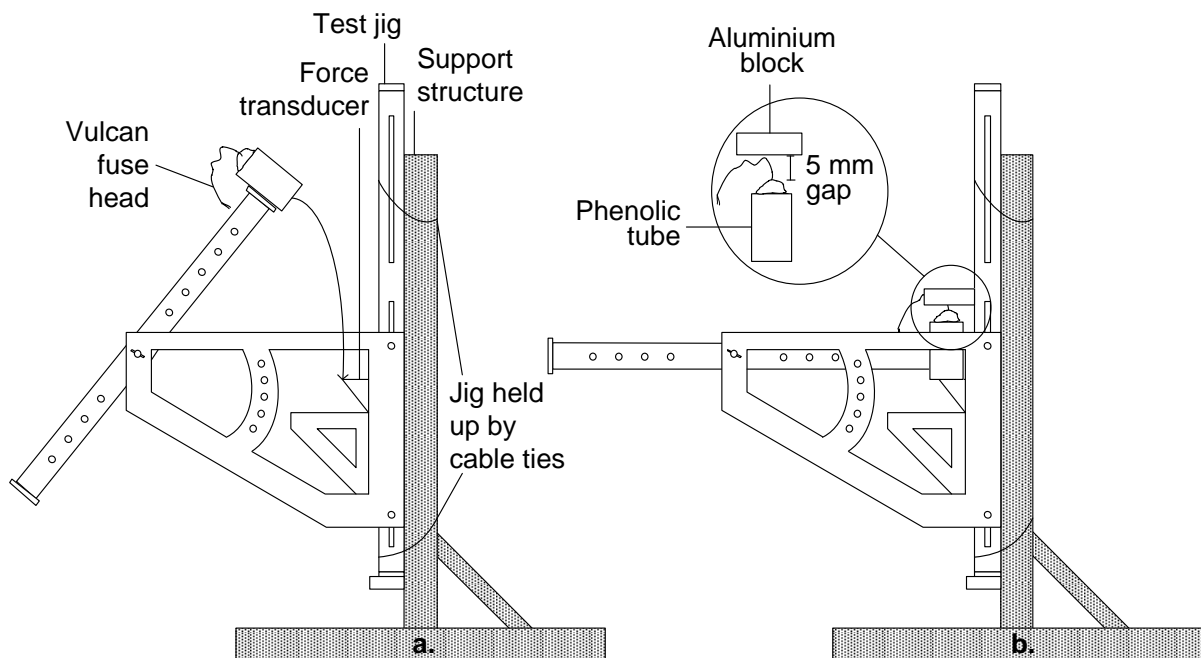
Figure 3-6: Jig setup for metal-cutting tests showing sample and aluminium block placement

3.10.2. Method for metal-cutting tests

3.10.2.1. Test setup

Phenolic tubes with a diameter of 15 mm and a depth of 28 mm were oven-dried at 30 °C for a few days before use. The method described in Section 3.7.2 was used to cast thermite compositions directly into the phenolic tubes. After the compositions set, the tubes were sealed with a lid containing a nozzle opening as shown in Figure 3-5a. They were manufactured to possess a nozzle diameter of 6 mm. The filled phenolic tubes were then placed in a stainless steel housing, and Figure 3-5a shows the nozzle was screwed in place with a fastener. A starter composition composed of 41 wt-% copper oxide (CuO), 33 wt-% molybdenum trioxide (MoO_3) and 25 wt-% magnalium (Mg and Al alloy) was used. About 0.4 – 0.6 g starter was poured into the opening of the nozzle. An electrical Vulcan fuse head was carefully placed in the opening so that it came in contact with the starter. Aluminium tape was placed over the nozzle opening to keep the fuse head in place and to assist in pressure build-up after ignition. The test jig was fastened to the metal support structure with cable ties as shown in Figure 3-6a. The prepared sample was screwed onto the jig above the force transducer, and placed perpendicular to the ground. An 80 mm diameter aluminium block (with varying thickness) was weighed and labelled. It was then clamped onto the jig. A distance of 5 mm was maintained between the block of aluminium and the nozzle. Graphite nozzles were used first, as they do not corrode very easily. Phenolic nozzles corrode more easily than graphite, resulting in a larger nozzle diameter throughout a burn.

3.10.2.2. Remote firing procedure

The D10 firing cable was rolled out from the test jig to the shelter. The D10 cable was tested for continuity using a Blast Current Indicator (BCI) and Alex 7 initiation device at the test jig. It was then connected to the Vulcan fuse head. The GoPro camera and HBM U93 force transducer were set to record. At the shelter, the circuit was tested for continuity. A countdown to fire was given and the Alex 7 initiation device was fired. After firing, the sample was allowed to cool. The sample was then changed and the process repeated. If a misfire was declared, a period of 10 min was allowed to pass before entering the danger area. Continuity was tested again before firing. The burning time of the compositions was determined from the sound files obtained from the camera.

3.10.2.3. Safety, Health and Environment (SHE) assessment

Open air burn tests have shown that the thermite compositions burned > 1266 °C while the EKVI simulations indicated much higher values. It was expected that the burning performance of the thermite be improved and magnified in the confined environment of the tube. Laboratory tests showed that alumina tiles and clay bricks retained heat after burn tests. It was expected that the aluminium block would remain hot long after the tubes had been fired. The light and sparks emitted from the burning thermite can be harmful to one's eyes and skin. The tubes could malfunction by exploding, if the nozzle becomes clogged and the pressure build-up becomes too large. The explosion could cause harm by shrapnel travelling over a distance. A safe distance away from the firing area was therefore maintained.

Chapter 4: Thermodynamic simulations

4.1. EKVI simulations

4.1.1. Base case of calcium sulfate with aluminium

Calcium sulfate dihydrate (gypsum) with aluminium was the system of interest, since the former, i.e. Plaster of Paris, reacts with water to form gypsum. For comparison, the reaction of the different forms of calcium sulfate (anhydrite, hemihydrate and dihydrate) with aluminium were simulated in EKVI. Figure 4-1 shows the adiabatic reaction temperature for $CaSO_4$-Al, $CaSO_4 \cdot 0.5H_2O$-Al and $CaSO_4 \cdot 2H_2O$-Al systems.
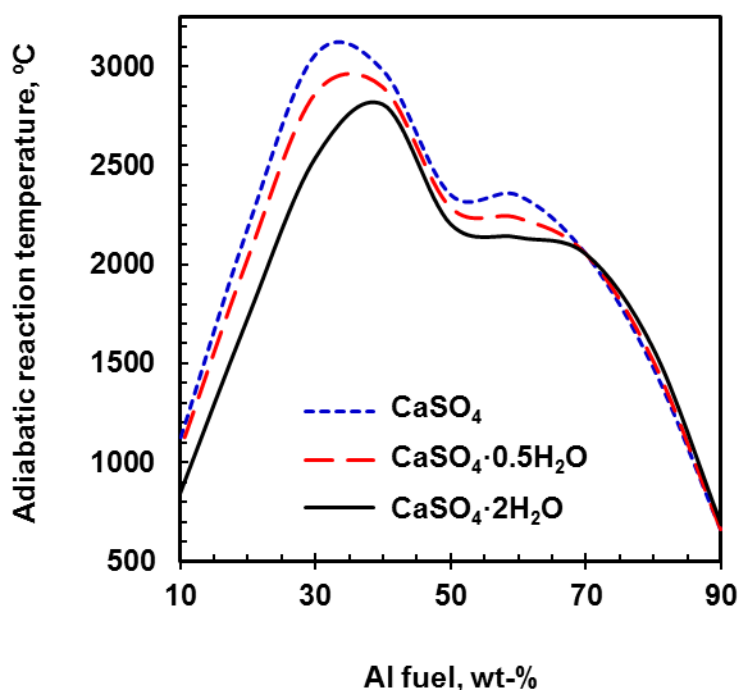
Figure 4-1: Temperature of different calcium sulfate forms with aluminium in EKVI

Figure 4-1 shows that the maximum adiabatic reaction temperature varies only slightly between each calcium sulfate form. The highest temperature is reached by the anhydrite, which occurs at approximately 3100 °C at a composition of 67 wt-% $CaSO_4$ and 33 wt-% Al. The hemihydrate reaches the next highest temperature of approximately 2900 °C at 64 wt-% $CaSO_4 \cdot 0.5H_2O$ and 36 wt-% Al. The maximum temperature reached by the dihydrate is approximately 2800 °C. This occurs at a composition of 60 wt-% $CaSO_4 \cdot 2H_2O$ and 40 wt-% Al. It is expected that the dihydrate would produce the lowest maximum temperature, since the water of hydration present require more energy to be driven off in the reaction.

It is interesting that two peaks in temperature are observed in all three systems. This indicates that there may be a product(s) that is producing a large amount of energy at these fuel loadings. As mentioned previously, the first temperature peak for the $CaSO_4$-Al, $CaSO_4 \cdot 0.5H_2O$-Al and $CaSO_4 \cdot 2H_2O$-Al systems occur at approximately 33 wt-%, 36 wt-% and 40 wt-% respectively. The second temperature peak is observed at ~59 wt-% for all systems.

Figure 4-2 shows a comparison of the specific enthalpy change for $CaSO_4$-Al, $CaSO_4 \cdot 0.5H_2O$-Al and $CaSO_4 \cdot 2H_2O$-Al systems at varying aluminium loadings.
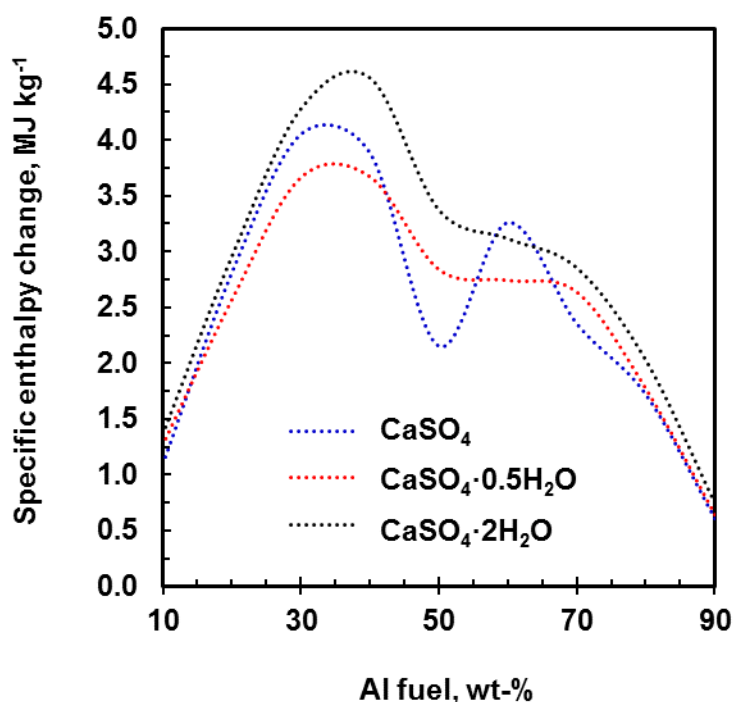
Figure 4-2: Specific enthalpy change for different calcium sulfate forms with aluminium in EKVI

Figure 4-2 shows that the specific enthalpy change follows a similar trend to that of the temperature plot in Figure 4-1 in that two peaks are produced at a lower and higher fuel loading. However, while the reaction temperature decreases from anhydrite to dihydrate the enthalpy change does not decrease. In fact, the largest enthalpy change is released by the $CaSO_4 \cdot 2H_2O$-Al system.

The maximum enthalpy or energy output is 4.60 MJ kg^{-1} at 38 wt-% Al and 62 wt-% CaSO$_4$·2H$_2$O. This follows literature trends that have found that hydrated salts produce more energy than non-hydrated salt (Comet et al., 2015). It is assumed that this is beneficial for the cast thermite since more energy is available to melt and cut metal. The next highest enthalpy change of 4.10 MJ kg^{-1} is for the anhydrite system, occurring at 33 wt-% Al and 67 wt-% CaSO$_4$. Similarly, the maximum enthalpy change for the hemihydrate system is 3.80 MJ kg^{-1} at 36 wt-% Al and 64 wt-% CaSO$_4$·0.5H$_2$O.

Figure 4-3 shows the total condensed products for different calcium sulfate forms with aluminium.
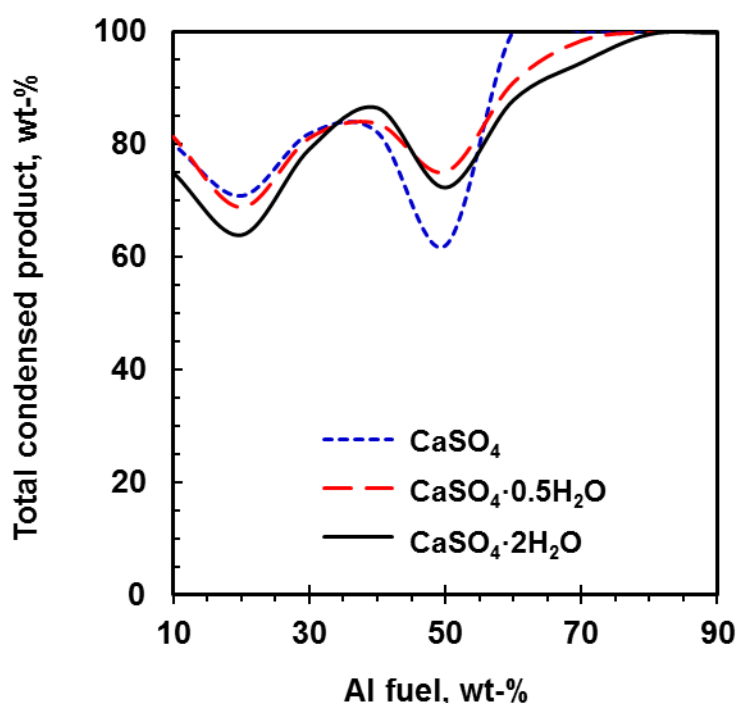
Figure 4-3: Comparison of total condensed products for various calcium sulfate-aluminium systems in EKVI

Condensed products were found to be the dominating reaction product species for the various calcium sulfate-aluminium systems shown in Figure 4-3. The reaction is gasless at 60 wt-% Al for CaSO$_4$-Al, while this only occurs after about 80 wt-% Al for CaSO$_4$·0.5H$_2$O-Al and CaSO$_4$·2H$_2$O-Al systems. The presence of gases would be beneficial in creating a jet to assist with cutting. The inferred gaseous product content indicates that there are maxima at approximately 20 wt-% Al and 50 wt-% Al for CaSO$_4$·2H$_2$O-Al and CaSO$_4$-Al systems respectively.

Figure 4-4 displays the total gaseous products in (a) moles (mol per 100 g thermite) and (b) volume (m^3 per 100 g thermite).
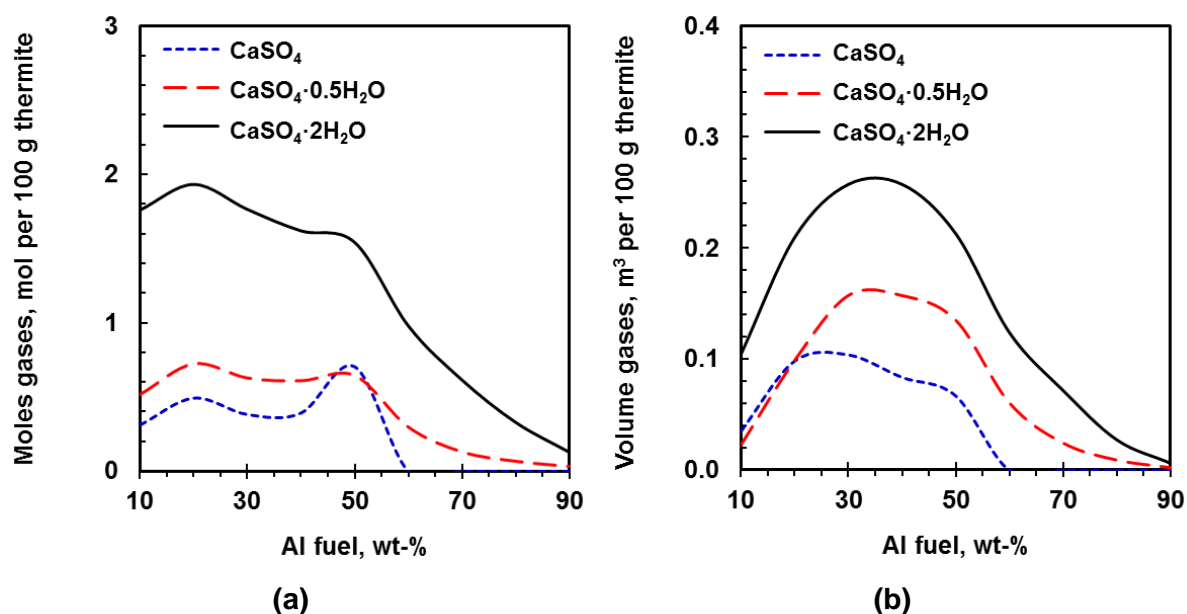
Figure 4-4: The (a) moles and (b) volume of total gases for various calcium sulfate-aluminium systems in EKVI

Figure 4-4a shows $CaSO_4 \cdot 2H_2O$-Al system releases the largest molar amount of total gaseous products when compared to the other systems. A maximum of 1.93 mol gas per 100 g thermite is produced at 20 wt-% Al. Similarly, the $CaSO_4 \cdot 0.5H_2O$-Al system contains a maximum at 50 wt-% producing 0.70 mol gas per 100 g thermite.

The volume of gases was then considered. Figure 4-4b shows the largest volume of gaseous products is produced for the $CaSO_4 \cdot 2H_2O$-Al system. A maximum volume of gas of 0.26 m^3 per 100 g thermite was produced at approximately 36 wt-% Al. The least gas was produced by the $CaSO_4$-Al system.

The gaseous products for the reaction between the dihydrate and aluminium is shown in Figure 4-5.
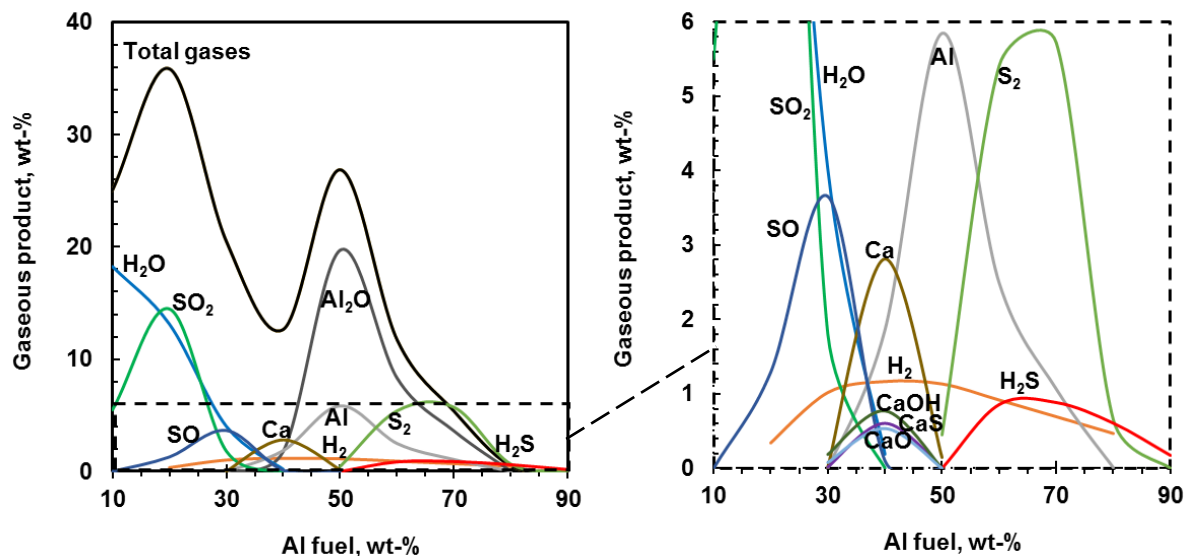
Figure 4-5: Gaseous products from CaSO$_4$·2H$_2$O-Al system in EKVI

Figure 4-5 shows the gaseous products from the CaSO$_4$·2H$_2$O-Al system. There are many gaseous products present for the system, and the product content < 8 wt-% is enlarged on the right of Figure 4-5 for better viewing. Two main peaks are seen in the gaseous products profile, which correspond to the production SO$_2$ and H$_2$O at the first peak at around 20 wt-% Al and Al$_2$O at the second peak at around 50 wt-% Al.

The total gases at the optimum fuel loading of 40 wt-% Al is approximately 12 wt-%. This is made up of 2 wt-% hydrogen (H$_2$), 2 wt-% aluminium oxide (Al$_2$O), 2 wt-% aluminium (Al), 1 wt-% sulfur (S), 0.9 wt-% hydrogen sulfide (HS), 3 wt-% calcium (Ca), 0.8 wt-% calcium hydroxide (CaOH), 0.6 calcium sulfide (CaS) and 0.5 wt-% calcium oxide (CaO).

The condensed products profile for from the $CaSO_4 \cdot 2H_2O$-Al system is shown in Figure 4-6.
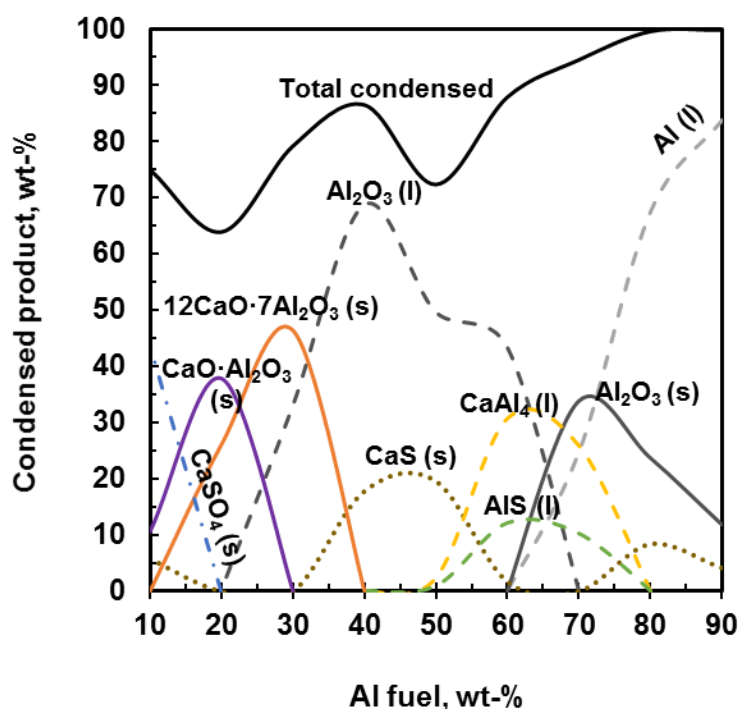
Figure 4-6: Condensed products from $CaSO_4 \cdot 2H_2O$-Al system in EKVI

Similarly, Figure 4-6 shows that, on a mass basis, there are more condensed than gaseous products. There is a total of 87 wt-% condensed products at the optimum fuel loading of 40 wt-% aluminium. At this optimum point, approximately 69 wt-% aluminium oxide (Al_2O_3 (l)) and 18 wt-% calcium sulfide (CaS (s)) are present. In addition to these products is $12CaO \cdot 7Al_2O_3$ (s) or dodecacalcium hepta-aluminate, which seems to contribute a great amount of energy to the first peak before the optimum point is reached.

Interestingly, the $12CaO \cdot 7Al_2O_3$ product is observed in both condensed product plots of the anhydrite-aluminium ($CaSO_4$-Al) and hemihydrate-aluminium ($CaSO_4 \cdot 0.5H_2O$-Al) systems seen in Figure 4-7.
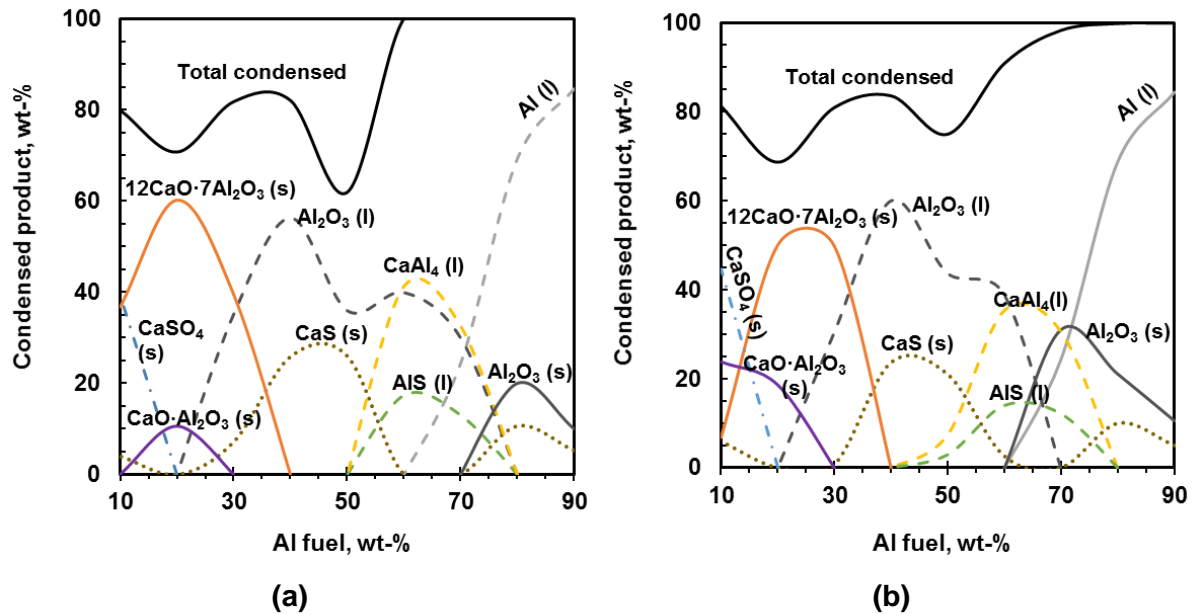
Figure 4-7: Condensed products from (a) $CaSO_4$-Al and (b) $CaSO_4 \cdot 0.5H_2O$-Al systems in EKVI

Figure 4-7a shows the $CaSO_4$-Al system containing ~84 wt-% total solids at the first peak seen in Figure 4-1. The main condensed species present at the optimum fuel loading of 32 wt-% Al are 46 wt-% Al_2O_3 (l), 14 wt-% CaS (s) and 24 wt-% $12CaO \cdot 7Al_2O_3$ (s), also known as mayenite. Similarly, Figure 4-7b shows the hemihydrate-aluminium ($CaSO_4 \cdot 0.5H_2O$-Al) system containing ~83 wt-% total solids at the first peak seen in Figure 4-1. The condensed species present at this optimum fuel loading of 35 wt-% Al are 45 wt-% Al_2O_3 (l), 10 wt-% CaS (s) and 34 wt-% $12CaO \cdot 7Al_2O_3$ (s).

It is noted that maximum amounts of $12CaO \cdot 7Al_2O_3$ (40 wt-%, 60 wt-% and 54 wt-%) are produced at 20 – 30 wt-% Al loadings for $CaSO_4 \cdot 2H_2O$-Al, $CaSO_4$-Al and $CaSO_4 \cdot 0.5H_2O$-Al systems in Figure 4-6 and Figure 4-7. The dodecacalcium hepta-aluminate ($12CaO \cdot 7Al_2O_3$) is also known as mayenite. It is a high-energy releasing product and would therefore be beneficial to produce. It was suggested that an oxidiser such as calcium bismuthate could be used with aluminium fuel to produce mayenite.

Figure 4-8 shows the gaseous products for $CaSO_4$-Al and $CaSO_4 \cdot 0.5H_2O$-Al systems run in EKVI.
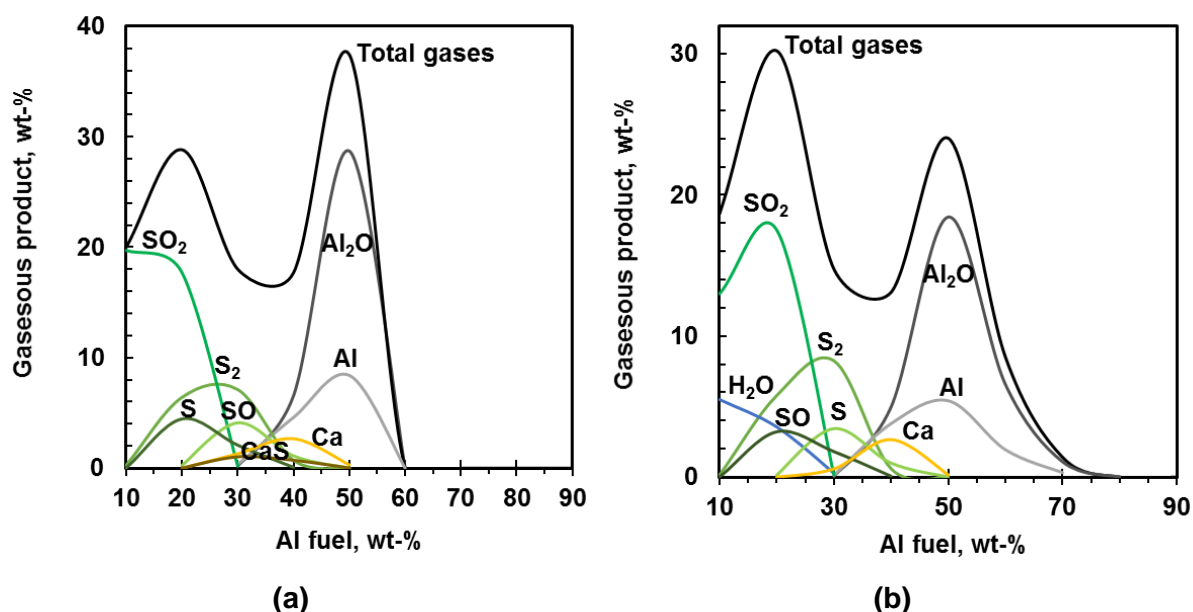
Figure 4-8: Gaseous products from (a) $CaSO_4$-Al and (b) $CaSO_4 \cdot 0.5H_2O$-Al systems in EKVI

There are fewer products for $CaSO_4$-Al and $CaSO_4 \cdot 0.5H_2O$ in Figure 4-8a and Figure 4-8b when compared with the $CaSO_4 \cdot 2H_2O$-Al system in Figure 4-5. The reduction of water present in the oxidiser also resulted in fewer total gases produced; a total of 60 wt-% gaseous products were produced for $CaSO_4$-Al while 90 wt-% was produced for $CaSO_4 \cdot 2H_2O$-Al. Two peaks are present for both systems corresponding to the main products of SO_2 and Al_2O/Al.

4.1.1.1. Dominant reactions at key fuel contents

The reactions dominating at key fuel loadings were deduced from the product spectra shown in Figure 4-5 and Figure 4-6 for the $CaSO_4 \cdot 2H_2O$-Al system. These are determined at maxima in adiabatic reaction temperatures. Reaction 31 and Reaction 32 show the dominant reactions around 15.5 wt-% Al and 17.3 wt-% Al respectively, where the main condensed products are dodecacalcium hepta-aluminate and monocalcium aluminate. The gaseous reaction products are water and sulfur-based compounds.

$$14\ Al_{(s)} + 12\ CaSO_4 \cdot 2H_2O_{(s)} \rightarrow 12\ CaO \cdot 7Al_2O_{3\ (s)} + 9\ SO_{2\ (g)} + 3\ H_2S_{(g)} + 21\ H_2O_{(g)} \quad (31)$$

$$4\ Al_{(s)} + 3\ CaSO_4 \cdot 2H_2O_{(s)} \rightarrow CaS_{(s)} + 2\ CaO \cdot 7Al_2O_{3\ (s)} + 2\ SO_{2\ (g)} + 6\ H_2O_{(g)} \quad (32)$$
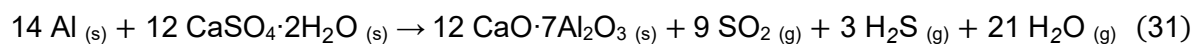
Reaction 33 shows the dominant reactions at 9 wt-% Al. The main condensed product is monocalcium aluminate with sulfur monoxide, hydrogen sulfide and water as gaseous products.

$$6 \; Al_{(s)} + CaSO_4 \cdot 2H_2O_{(s)} \rightarrow 3 \; CaO \cdot Al_2O_{3 \, (s)} + SO_{(g)} + S_{2 \, (g)} + H_2S_{(g)} + 5 \; H_2O_{(g)} \qquad (33)$$
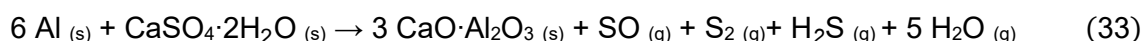
Reaction 34 shows the dominant reaction circa 38.5 wt-% Al. The main condensed products are solid calcium sulfide and molten aluminium oxide while the gaseous products include calcium and hydrogen vapours.

$$8 \; Al_{(s)} + 2 \; CaSO_4 \cdot 2H_2O_{(s)} \rightarrow \; CaS_{(s)} + 4 \; Al_2O_{3 \, (l)} + Ca_{(g)} + \; 4 \; H_{2 \, (g)} \qquad (34)$$
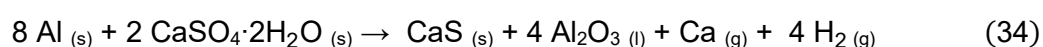
4.1.2. Using a calcium sulfate blend with aluminium

The effect of a calcium sulfate blend as oxidiser was investigated to determine how the temperature and enthalpy change would be affected. Fuel loadings of 30 wt-% and 40 wt-% aluminium resulted in the highest adiabatic reaction temperature and are thus of interest. Figure 4-9 shows a comparison between temperature and enthalpy change of $CaSO_4$-$CaSO_4 \cdot 2H_2O$-Al systems at 30 wt-% and 40 wt-% Al.
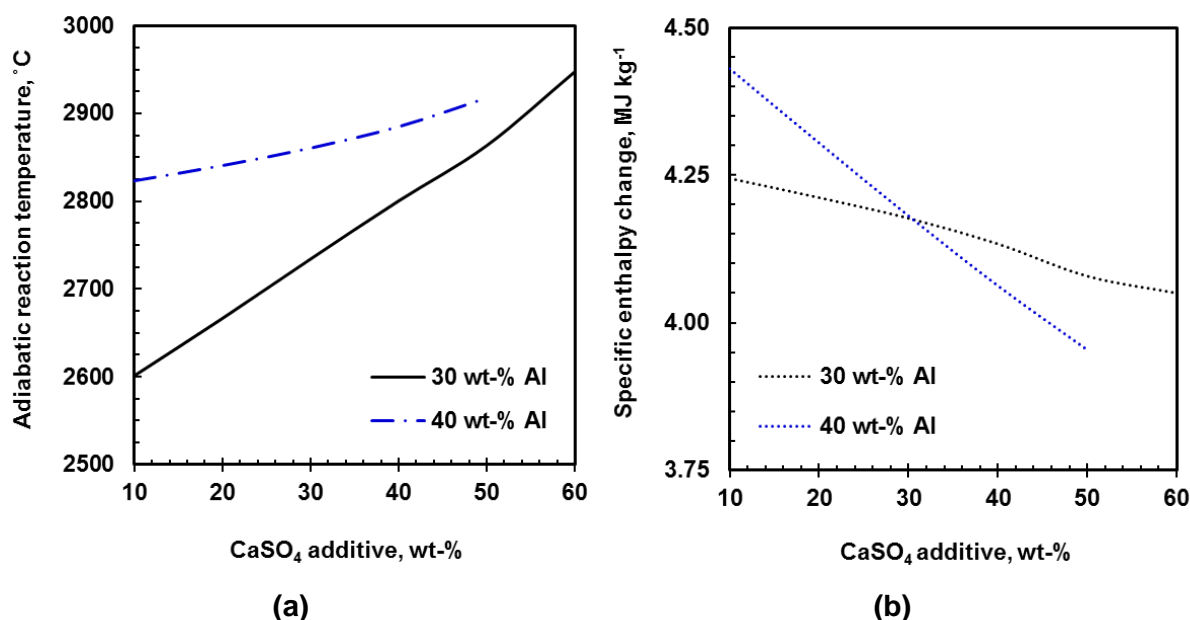
Figure 4-9: The (a) adiabatic reaction temperature and (b) system enthalpy change of calcium sulfate blends (anhydrite, dihydrate) and aluminium in EKVI

Figure 4-9a shows that a maximum reaction temperature of 2950 °C is reached at a composition of 60 wt-% $CaSO_4$, 10 wt-% $CaSO_4 \cdot 2H_2O$ and 30 wt-% Al. The 40 wt-% Al system reaches a maximum temperature of 2920 °C occurring at a composition of 50 wt-% $CaSO_4$ and 10 wt-% $CaSO_4 \cdot 2H_2O$. It can be seen that an increase in $CaSO_4$ oxidiser results in a higher adiabatic reaction temperature.

On the other hand, Figure 4-9b shows an opposing trend where an increase in $CaSO_4$ oxidiser results in a decrease in enthalpy change. A maximum enthalpy change of 4.25 MJ kg^{-1} is reached at a composition of 10 wt-% $CaSO_4$, 60 wt-% $CaSO_4 \cdot 2H_2O$ and 30 wt-% Al. It should be noted that the enthalpy change range is small and varies between 4.05 MJ kg^{-1} and 4.25 MJ kg^{-1}. Similarly, the 40 wt-% Al system reaches a maximum enthalpy change of 4.43 MJ kg^{-1} at a composition of 10 wt-% $CaSO_4$ and 50 wt-% $CaSO_4 \cdot 2H_2O$. The enthalpy range differs slightly to that of the 30 wt-% system, since it is larger between 3.95 MJ kg^{-1} and 4.43 MJ kg^{-1}.

Gaseous products from the calcium sulfate blend-aluminium system ($CaSO_4$-$CaSO_4 \cdot 2H_2O$-Al) are shown in Figure 4-10a and Figure 4-10b, which are for constant fuel loadings of 30 wt-% and 40 wt-% aluminium respectively.

(a)   **(b)**

Figure 4-10: Gaseous products from calcium sulfate blend (anhydrite, dihydrate) and (a) 30 wt-% aluminium, (b) 40 wt-% aluminium in EKVI

Figure 4-10a shows the gaseous products for the 30 wt-% Al system, where the $CaSO_4$ content varies between 10 – 60 wt-% while the $CaSO_4 \cdot 2H_2O$ content varies between 60 – 10 wt-%. The total gaseous products for the oxidiser content described varies in the range of 18 – 20 wt-%. The major gaseous products include disulfur (S_2), sulfur (S), sulfur oxide (SO), bisulfide (HS), sulfur dioxide (SO_2) and water (H_2O).

Similarly, Figure 4-10b shows the gaseous products for the 40 wt-% Al system. For the blend of oxidisers in this case, the $CaSO_4$ content varies between 10 – 50 wt-% while the $CaSO_4 \cdot 2H_2O$ content varies between 50 – 10 wt-%. The total gaseous products range between 14 – 17 wt-%. The major gaseous products in Figure 4-10b differ to those seen in Figure 4-10a; they include aluminium(I) oxide (Al_2O), aluminium (Al), calcium (Ca) and sulfur (S).

Condensed products from the $CaSO_4$-$CaSO_4 \cdot 2H_2O$-Al system are shown in Figure 4-11a and Figure 4-11b, which are for constant fuel loadings of 30 wt-% and 40 wt-% aluminium respectively.

Figure 4-11: Condensed products from calcium sulfate (anhydrite, dihydrate) with (a) 30 wt-% and (b) 40 wt-% aluminium reactants in EKVI

Figure 4-11a shows the condensed products for the 30 wt-% Al system. The $CaSO_4$ content varies between 10 – 60 wt-% while the $CaSO_4 \cdot 2H_2O$ content varies between 60 – 10 wt-%. The total condensed products in this system varies in the range of 80 – 82 wt-%, considerably

less than the total gaseous products. The major condensed products include dodecacalcium hepta-aluminate (12CaO·7Al$_2$O$_3$ (s)), aluminium oxide (Al$_2$O$_3$ (l)) and calcium sulfide (CaS (s)).

Similarly, Figure 4-11b shows the condensed products for the 40 wt-% Al system. For the blend of oxidisers in this case, the CaSO$_4$ content varies between 10 – 50 wt-% while the CaSO$_4$·2H$_2$O content varies between 50 – 10 wt-%. The total condensed products in this system varies in the range of 83 – 86 wt-%, considerably more than the total gaseous products. The major condensed products include aluminium oxide (Al$_2$O$_3$ (l)) and calcium sulfide (CaS (s)).

4.1.3. Addition of sulfur

Fuel loadings of 30 wt-% and 40 wt-% aluminium resulted in the highest adiabatic reaction temperature and specific enthalpy change and are thus of interest. Figure 4-12a and Figure 4-12b shows a comparison of the temperature and enthalpy change reached by a calcium sulfate dihydrate, sulfur and aluminium system (CaSO$_4$·2H$_2$O-S-Al) at 30 wt-% and 40 wt-% Al.
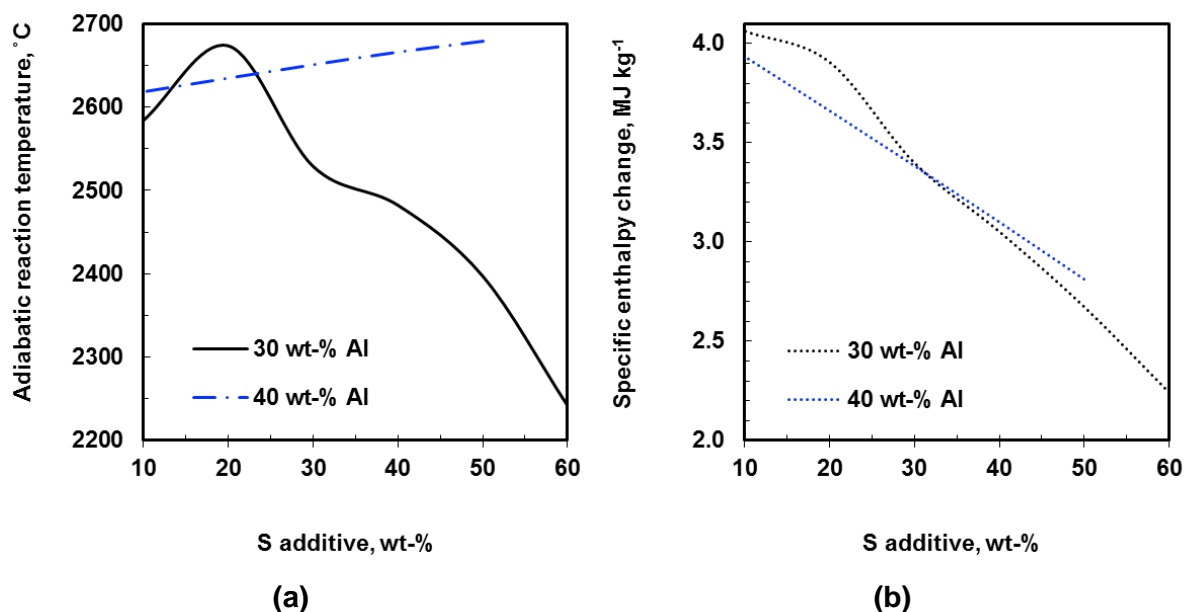
Figure 4-12: The (a) adiabatic reaction temperature and (b) system enthalpy change of calcium sulfate dihydrate, sulfur and aluminium in EKVI

Figure 4-12a shows that a maximum adiabatic reaction temperature of approximately 2680 °C is reached by both compositions. For the 30 wt-% Al system, the maximum temperature is reached at 50 wt-% CaSO$_4$·2H$_2$O and 20 wt-% S. After this maximum, increased sulfur loadings results in a significant decrease in adiabatic reaction temperature. In contrast, the

maximum temperature occurs at 10 wt-% $CaSO_4 \cdot 2H_2O$ and 50 wt-% S for the 40 wt-% Al system. The decrease in S loading from this maximum point decreases the temperature gradually. The main difference between the plots at these fuel loadings is attributed to the reaction occurring between S and Al. The reaction is not favourable at higher loadings of S for the 30 wt-% Al system. It can be seen that the reaction between S and Al is promoted at additional the greater fuel loading of 40 wt-% Al.

Figure 4-12b shows that an increase in S loading results in a decrease in reaction temperature for both systems. A maximum enthalpy change of 4.06 MJ kg^{-1} is reached at a composition of 60 wt-% $CaSO_4 \cdot 2H_2O$, 10 wt-% S and 30 wt-% Al. The enthalpy change ranges between 2.24 MJ kg^{-1} and 4.06 MJ kg^{-1}. Similarly, the 40 wt-% Al system reaches a maximum enthalpy change of 3.94 MJ kg^{-1} at loadings of 50 wt-% $CaSO_4 \cdot 2H_2O$ and 10 wt-% S. The enthalpy change ranges between 2.81 MJ kg^{-1} and 3.94 MJ kg^{-1}.

The gaseous products from the calcium sulfate dihydrate, sulfur and aluminium system ($CaSO_4 \cdot 2H_2O$-S-Al) are shown in Figure 4-13a and Figure 4-13b, which are for fuel loadings of 30 wt-% and 40 wt-% aluminium respectively.

(a)   **(b)**
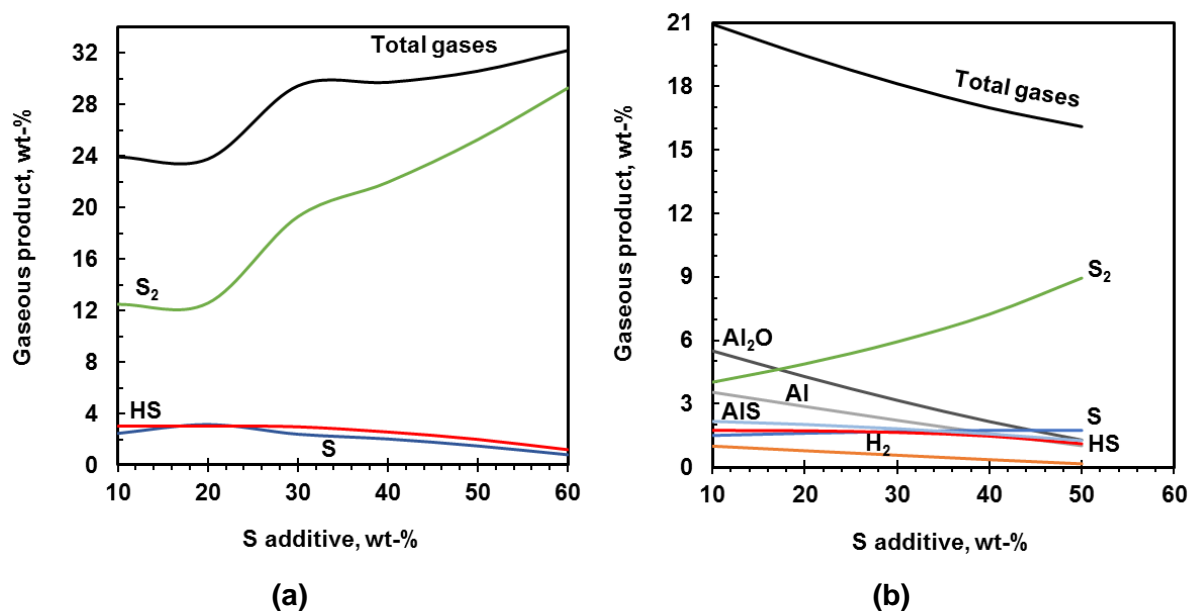
Figure 4-13: Gaseous products from calcium sulfate dihydrate, sulfur and (a) 30 wt-% aluminium, (b) 40 wt-% aluminium reactants in EKVI

Figure 4-13a shows the gaseous products for the 30 wt-% Al system, where the S content varies between 10 – 60 wt-% while the $CaSO_4 \cdot 2H_2O$ content varies inversely between 60 – 10 wt-%. The total gaseous content increases with decreasing S loading. The major

gaseous products for the 30 wt-% Al system include disulfur (S_2), hydrogen sulfide (HS) and sulfur (S).

Similarly, Figure 4-13b shows the gaseous products for the 40 wt-% Al system, where the $CaSO_4 \cdot 2H_2O$ content varies between 10 – 50 wt-% while the S content varies inversely between 50 – 10 wt-%. In contrast with Figure 4-13a, the total gaseous content increases with increasing $CaSO_4 \cdot 2H_2O$ loading. The major gaseous products for the 40 wt-% Al system include disulfur (S_2), aluminium(I) oxide (Al_2O), aluminium (Al), aluminium sulfide (AlS), hydrogen (H_2), sulfur (S) and hydrogen sulfide (H_2S).

Figure 4-14a and Figure 4-14b shows the condensed products for $CaSO_4 \cdot 2H_2O$-S-Al systems containing 30 wt-% Al and 40 wt-% Al respectively.
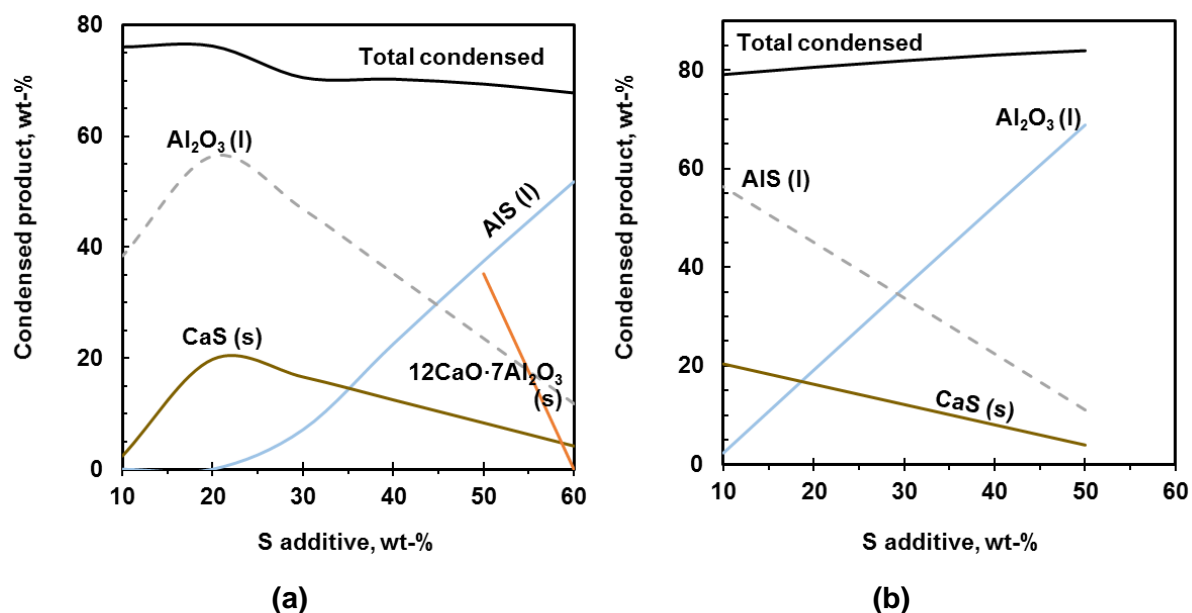
Figure 4-14: Condensed products from calcium sulfate dihydrate, sulfur and (a) 30 wt-% aluminium, (b) 40 wt-% aluminium reactants in EKVI

Figure 4-14a shows the condensed products for the 30 wt-% Al system, where the S content varies between 10 – 60 wt-% and $CaSO_4 \cdot 2H_2O$ content varies inversley between 60 – 10 wt-% while the. Similary, Figure 4-14b shows the condensed products for $CaSO_4 \cdot 2H_2O$-S-Al with 40 wt-%. The only exception of products between the two compositions is the presence of dodecacalcium hepta-aluminate ($12CaO \cdot 7Al_2O_3$ (s)) at the greater S loadings in the 30 wt-% Al composition.

4.1.4. Addition of copper sulfate pentahydrate

The addition of copper sulfate pentahydrate to the base case of calcium sulfate dihydrate and aluminium was then considered. Anhydrous copper sulfate ($CuSO_4$) was used in simulations to obtain a similar result, since the EKVI database does not possess copper sulfate pentahydrate ($CuSO_4 \cdot 5H_2O$). Fuel loadings of 30 wt-% and 40 wt-% aluminium resulted in the highest adiabatic reaction temperature and specific enthalpy and are thus of interest. Figure 4-15a and Figure 4-15b shows a comparison of the reaction temperature and enthalpy change reached by the calcium sulfate dihydrate, copper sulfate and aluminium system ($CaSO_4 \cdot 2H_2O$-$CuSO_4 \cdot 5H_2O$-Al) for fuel loadings of 30 wt-% and 40 wt-% Al.
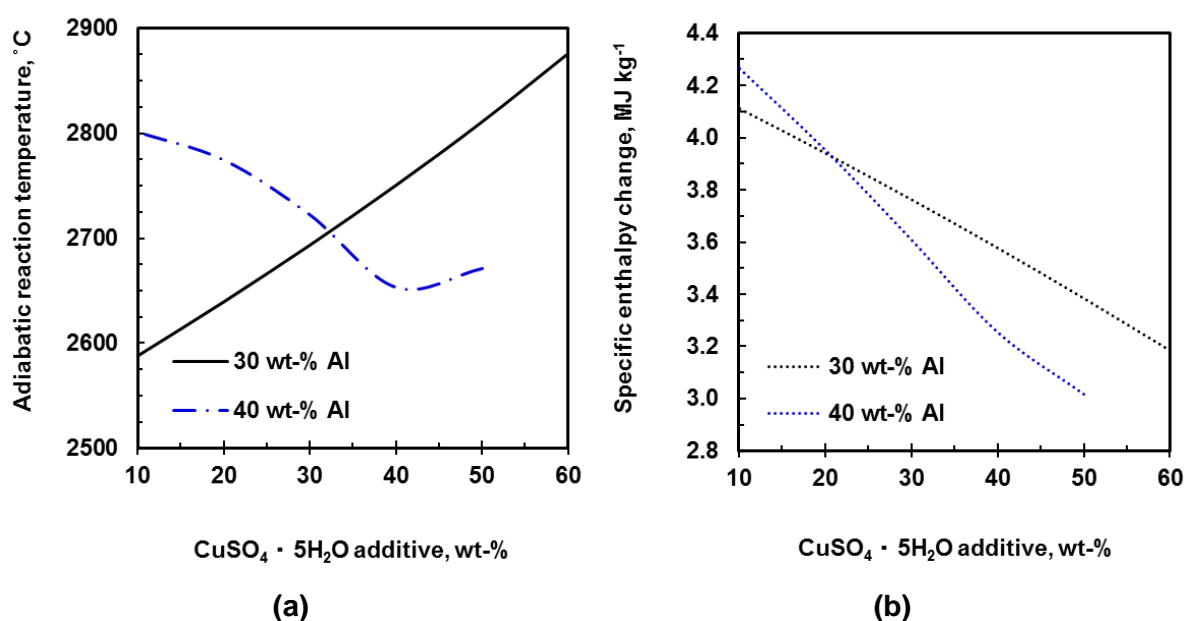
Figure 4-15: The (a) adiabatic reaction temperature and (b) system enthalpy change of calcium sulfate dihydrate, copper sulfate and aluminium in EKVI

Figure 4-15a shows the maximum reaction temperature reached by the 30 wt-% Al system is 2876 °C at 10 wt-% $CaSO_4 \cdot 2H_2O$ and 60 wt-% $CuSO_4$. The 40 wt-% Al system reaches 2801 °C at 50 wt-% $CaSO_4 \cdot 2H_2O$ and 10 wt-% $CuSO_4$. Figure 4-15b shows that the 40 wt-% Al system possesses a larger specific enthalpy change than the 30 wt-% Al system, with a maximum at the composition corresponding to the maximum temperature.

The gaseous products from the calcium sulfate dihydrate, copper sulfate pentahydrate and aluminium system ($CaSO_4 \cdot 2H_2O$-$CuSO_4$-Al) are shown in Figure 4-16a and Figure 4-16b, which are for fuel loadings of 30 wt-% and 40 wt-% aluminium respectively.

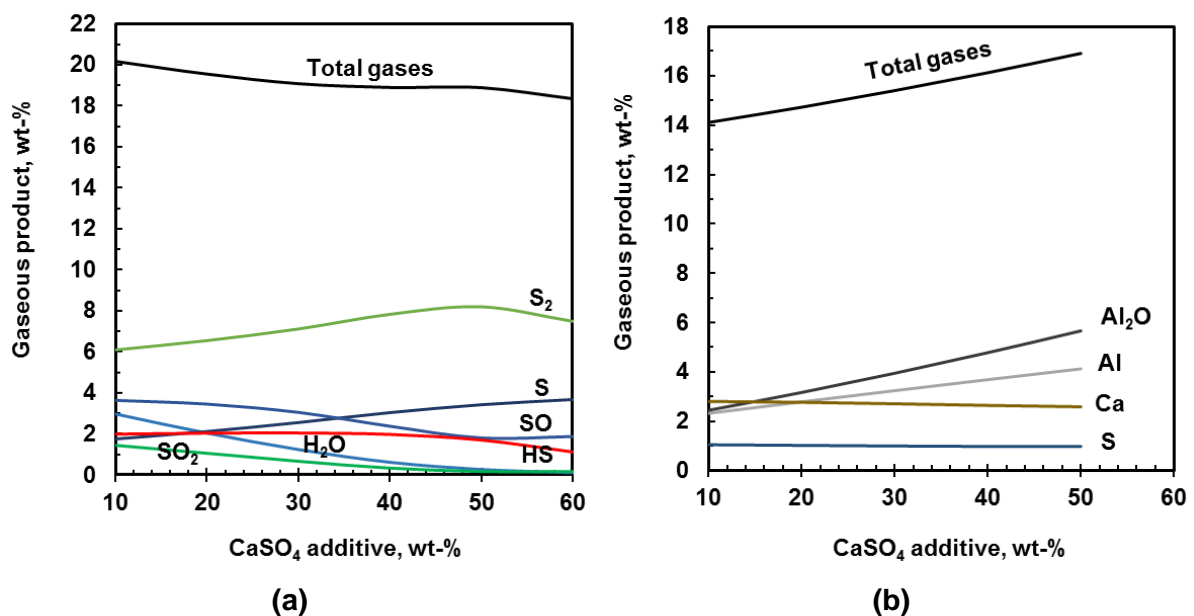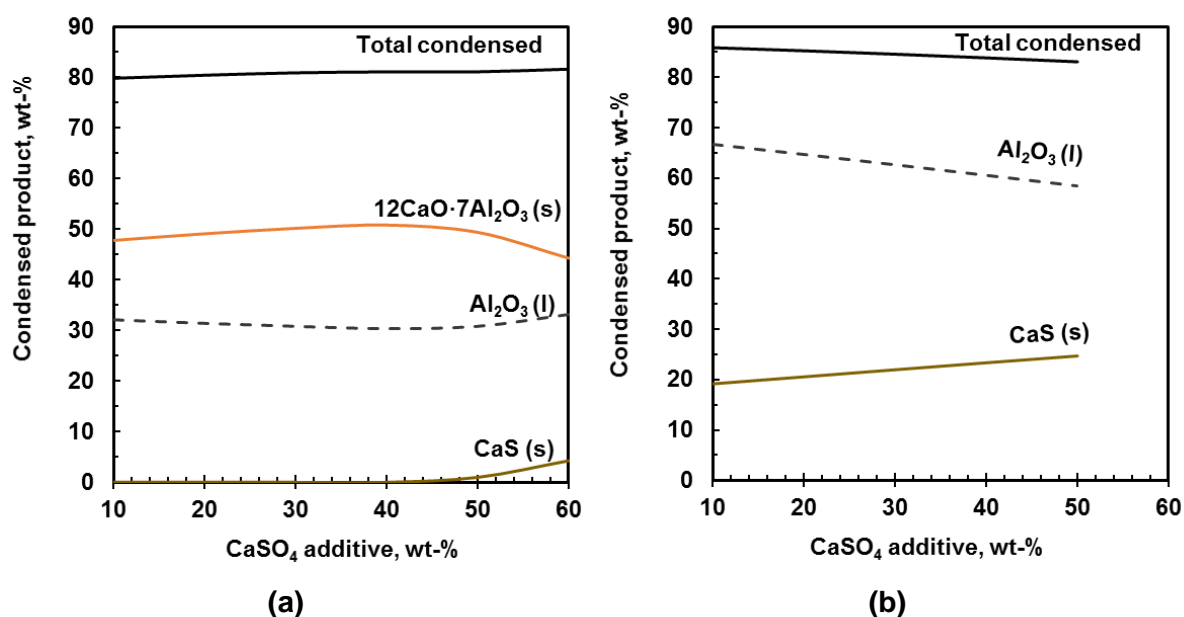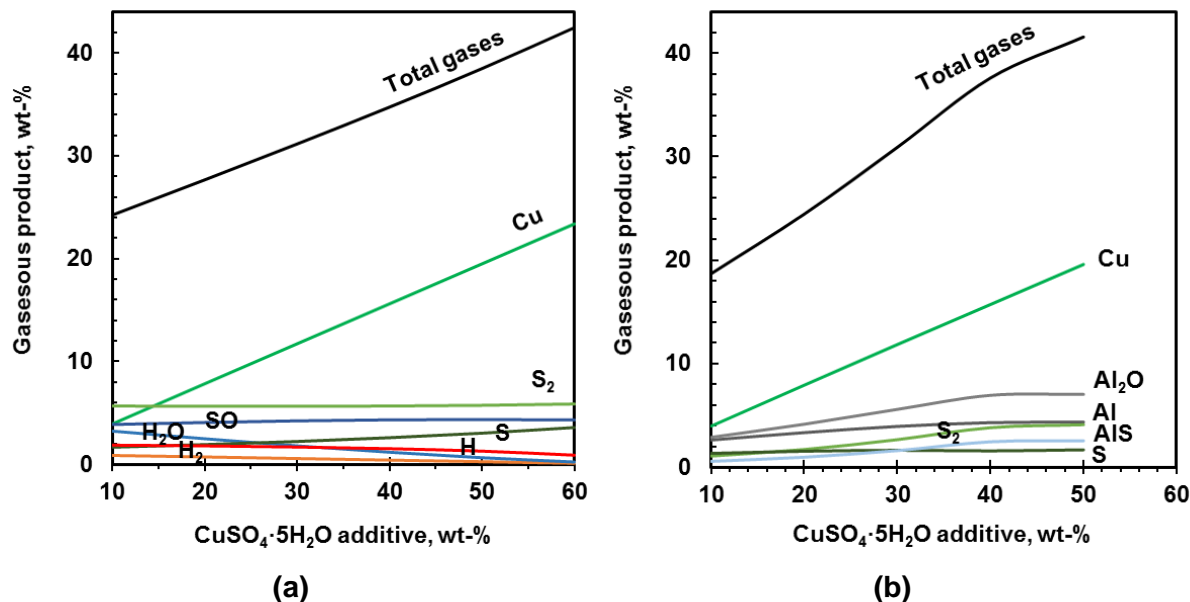**Figure 4-16:** Gaseous products from calcium sulfate dihydrate, copper sulfate and (a) 30 wt-% aluminium, (b) 40 wt-% aluminium reactants in EKVI

Figure 4-16a shows the gaseous products for the 30 wt-% Al system, where the $CaSO_4 \cdot 2H_2O$ content varied between 10 – 60 wt-% while the $CuSO_4$ content varied inversely between 60 – 10 wt-%. The total gaseous content decreases with increasing fuel loading. The major gaseous products for the 30 wt-% Al system includes copper (Cu), disulfur (S_2) and sulfur (S). Similarly, Figure 4-16b shows the gaseous products for the 40 wt-% Al system, where the $CaSO_4 \cdot 2H_2O$ content varied between 10 – 50 wt-% while the $CuSO_4$ content varied inversely between 50 – 10 wt-%. The total gaseous content also decreased with increasing oxidiser loading. The major gaseous products for the 40 wt-% Al system includes copper (Cu), aluminium oxide (Al_2O) and aluminium (Al).

Figure 4-17a and Figure 4-17b shows the condensed products for $CaSO_4 \cdot 2H_2O$-$CuSO_4$-Al systems containing 30 wt-% Al and 40 wt-% Al respectively.
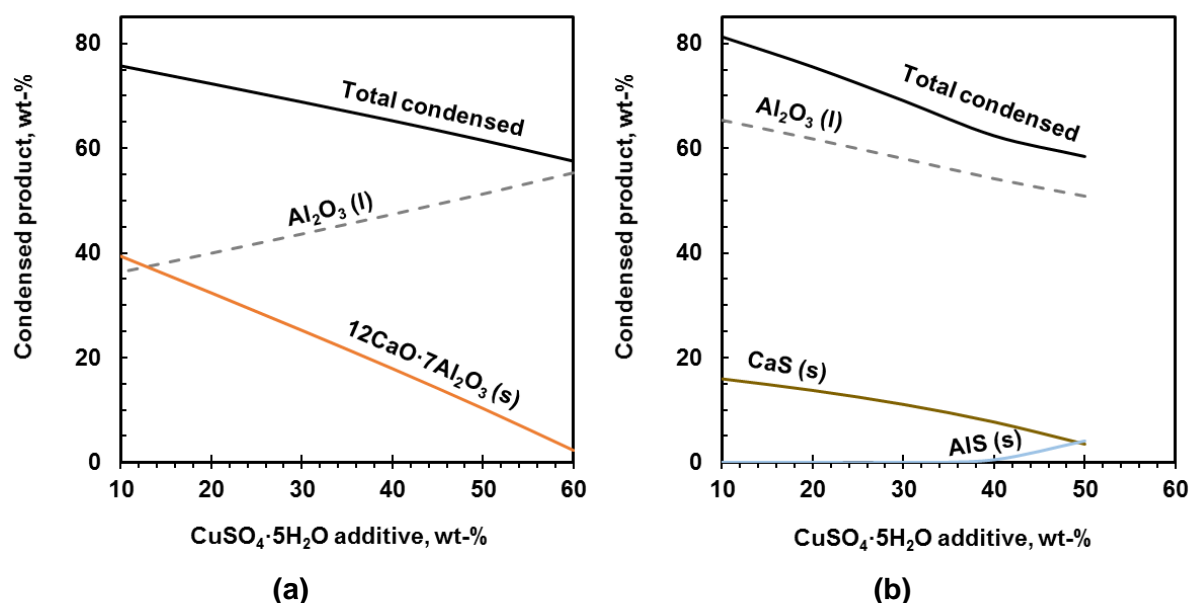
Figure 4-17: Condensed products from calcium sulfate dihydrate, copper sulfate pentahydrate reactants with (a) 30 wt-% aluminium and (b) 40 wt-% aluminium in EKVI

Both Figure 4-17a and Figure 4-17b show that the total condensed products increase with increasing oxidiser content. Major products for both compositions include aluminium oxide (Al_2O_3).

4.1.5. Lowering density with glass spheres

Sodium borosilicate glass spheres were simulated with the base case in EKVI. The composition of the glass spheres was obtained from elemental analysis (XRF) since it had not been specified by the supplier. A constant mass of base case thermite was maintained and glass spheres were added in addition to 100 wt-% thermite. It was recommended that no more than 30 wt-% glass spheres should be added to resin systems (AMT Composites, 2017).

The adiabatic reaction temperature and system enthalpy change for the glass spheres compositions are shown in Figure 4-18a and Figure 4-18b respectively.

(a)   **(b)**
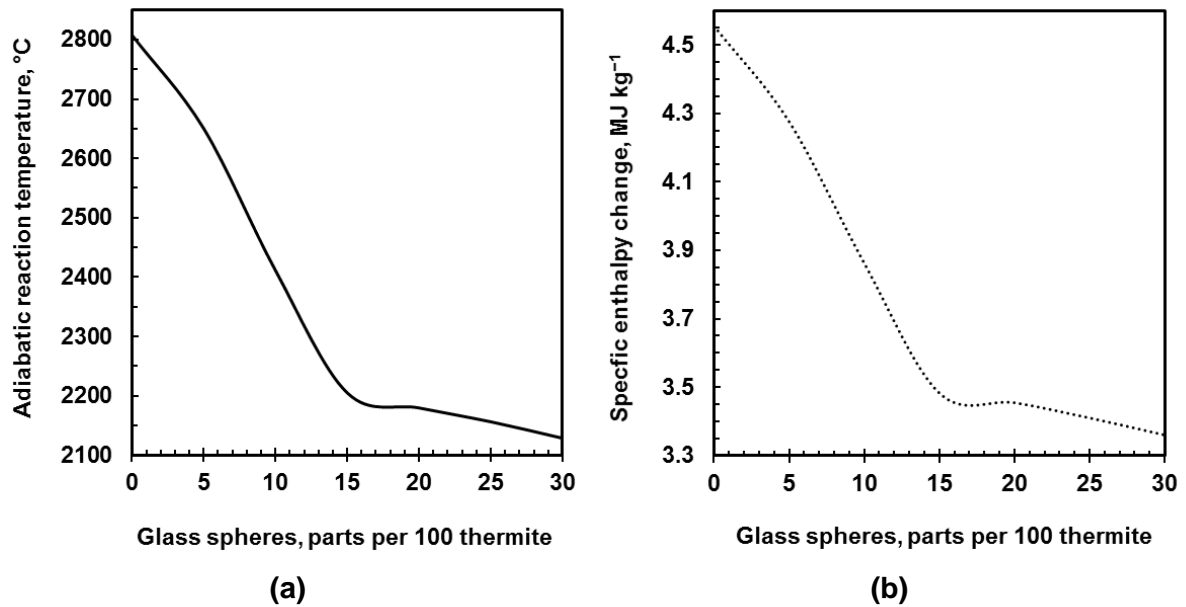
Figure 4-18: The (a) adiabatic reaction temperature and (b) specific enthalpy change of calcium sulfate dihydrate, sodium borosilicate glass spheres and aluminium in EKVI

The inclusion of glass spheres to the base case thermite decreased the reaction temperature and specific enthalpy change as seen in Figure 4-18a and Figure 4-18b respectively. There is a significant decrease in the performance of the casts after a 15 wt-% loading of glass spheres.

The gaseous and condensed products predicted for the glass spheres system is shown in Figure 4-19.

(a)   **(b)**
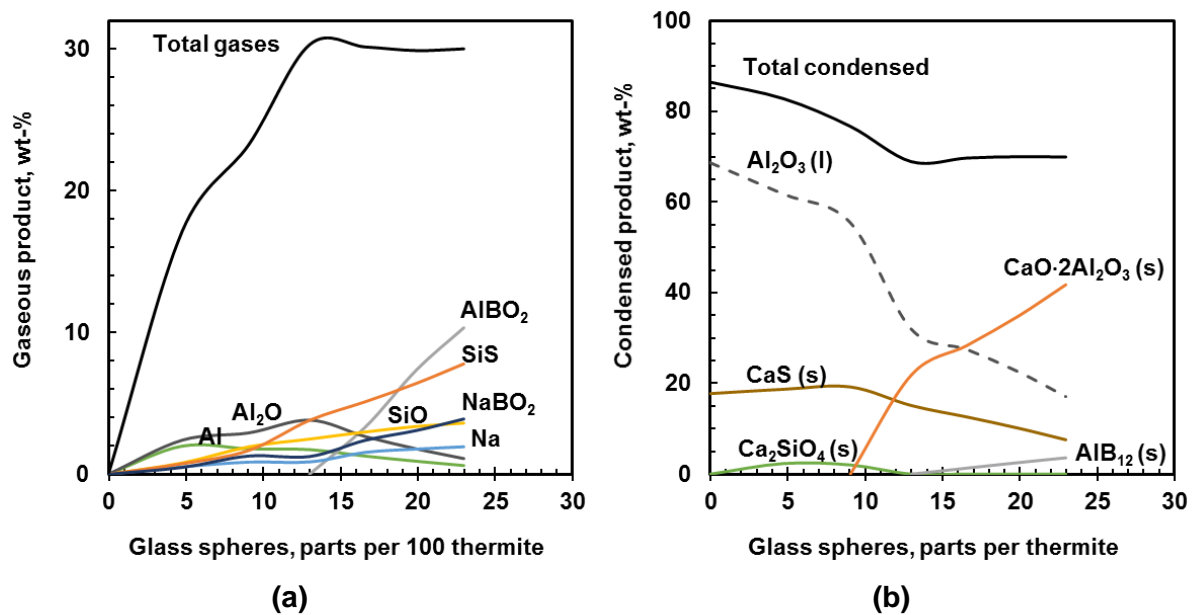
Figure 4-19: The (a) gaseous and (b) condensed products of calcium sulfate dihydrate, sodium borosilicate glass spheres and aluminium in EKVI

Figure 4-19a shows that the total gaseous products increase until a glass spheres loading of about 15 wt-% before remaining relatively constant. The total condensed products in Figure 4-19b decrease to the same point and also remain constant after 15 wt-% glass spheres. Major gaseous products include oxoboranyloxyaluminum ($AlBO_2$) and siliconmonosulfide (SiS) at higher loadings, while major condensed products are aluminium oxide (Al_2O_3) and monocalcium dialuminate ($CaO \cdot 2Al_2O_3$).

4.1.6. Summary of EKVI results

A summary of the optimum compositions obtained from EKVI are shown in Table 4-1.

Table 4-1: Summary of compositions, reaction temperature and system enthalpy from EKVI

Sample ID	Composition (wt-%)	Max T (°C)	Enthalpy (MJ kg^{-1})
Base1/GSB	60 $CaSO_4 \cdot 2H_2O$, 40 Al	2808	4.56
Blend2	30 $CaSO_4$, 30 $CaSO_4 \cdot 2H_2O$, 40 Al	2861	4.18
S4	50 $CaSO_4 \cdot 2H_2O$, 20 S, 30 Al	2674	3.91
CSP5	50 $CaSO_4 \cdot 2H_2O$, 10 $CuSO_4$, 40 Al	2801	4.27
GS1	5 $SiO_2/Na_2O/B$, 57 $CaSO_4 \cdot 2H_2O$, 38 Al	2650	4.28
GS2	10 $SiO_2/Na_2O/B$, 55 $CaSO_4 \cdot 2H_2O$, 36 Al	2411	3.86
GS3	15 $SiO_2/Na_2O/B$, 52 $CaSO_4 \cdot 2H_2O$, 35 Al	2205	3.48
GS4	20 $SiO_2/Na_2O/B$, 50 $CaSO_4 \cdot 2H_2O$, 33 Al	2180	3.45
GS5	25 $SiO_2/Na_2O/B$, 50 $CaSO_4 \cdot 2H_2O$, 33 Al	2156	3.41

4.2. FactSage simulations

4.2.1. Urea additive to Base1, Blend2, S4 and CSP5

EKVI's database did not contain urea so FactSage was used to simulate Base1, Blend2, S4 and CSP5 compositions with urea. Figure 4-20 shows the adiabatic reaction temperature for thermite compositions with urea ($CO(NH)_2$).
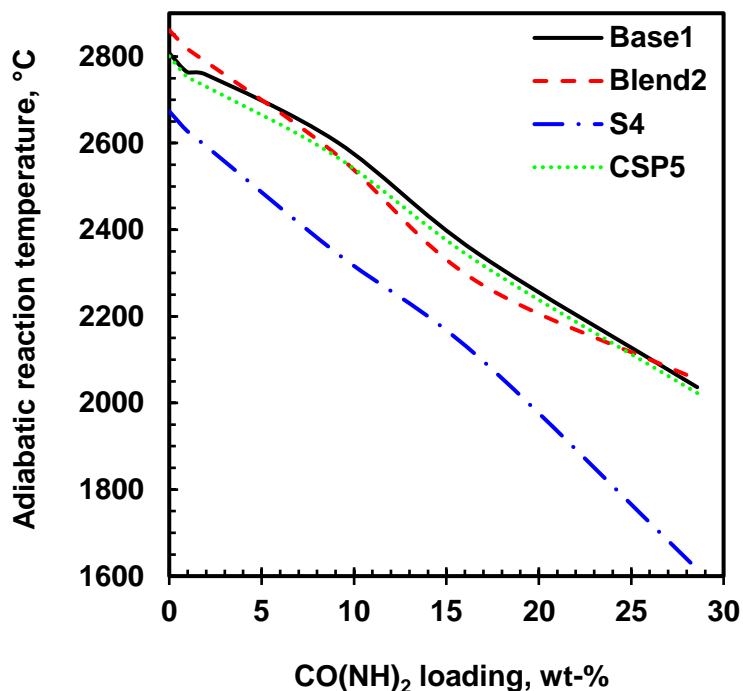
Figure 4-20: Adiabatic reaction temperature of Base1, Blend2, S4 and CSP5 compositions with urea in FactSage

Figure 4-20 shows that the addition of urea to all the compositions results in a reduction in adiabatic reaction temperature. Base1, Blend2 and CSP5 compositions display similar trends, while the S4 composition showed a lower adiabatic reaction temperature to the other compositions.

Figure 4-21 shows the gaseous and condensed products for Base1, Blend2, S4 and CSP5 compositions containing urea obtained from FactSage simulations.

(a)

(b)

(c)

(d)

(e)

(f)

(g)   (i)
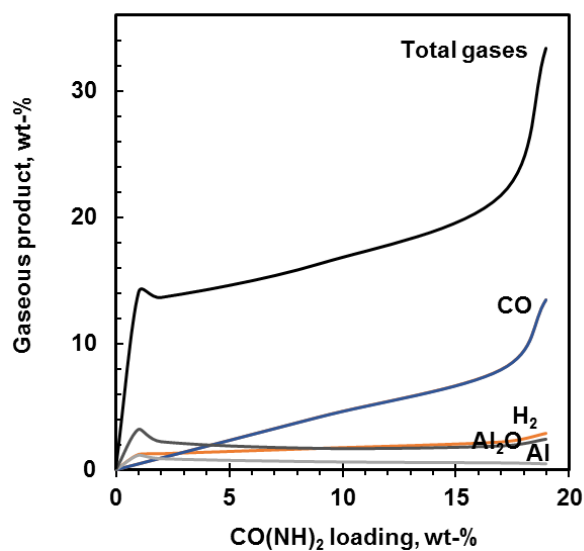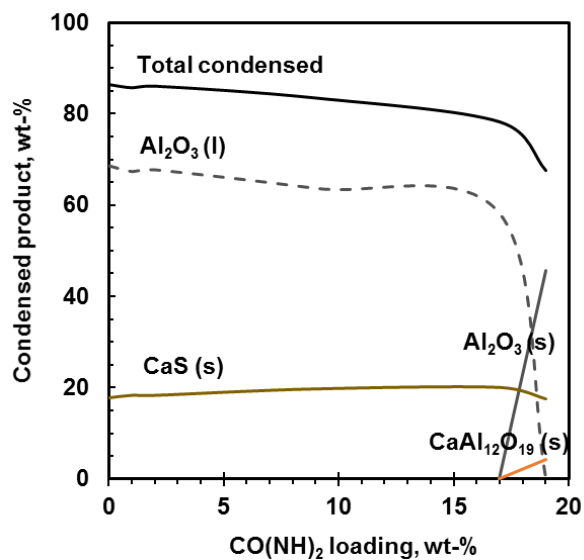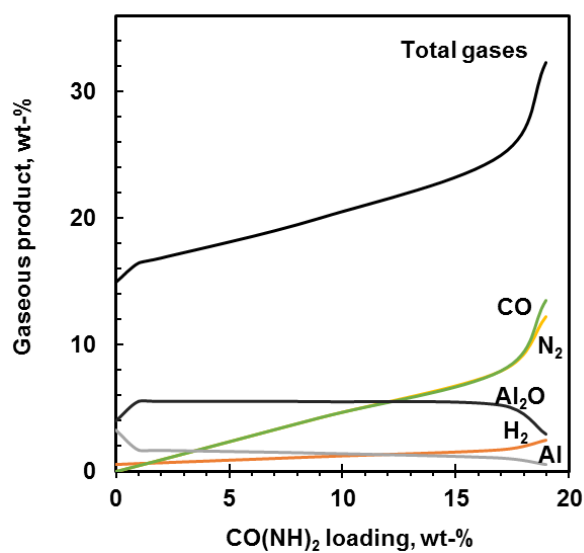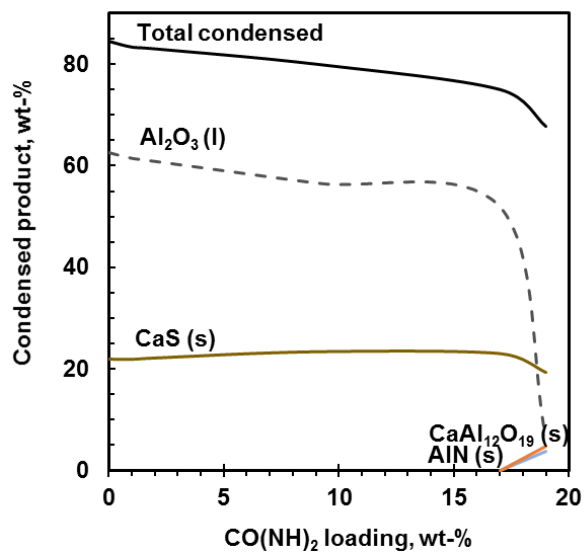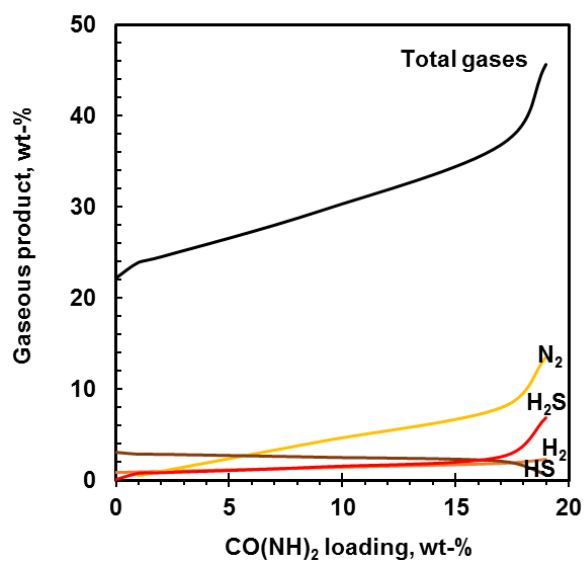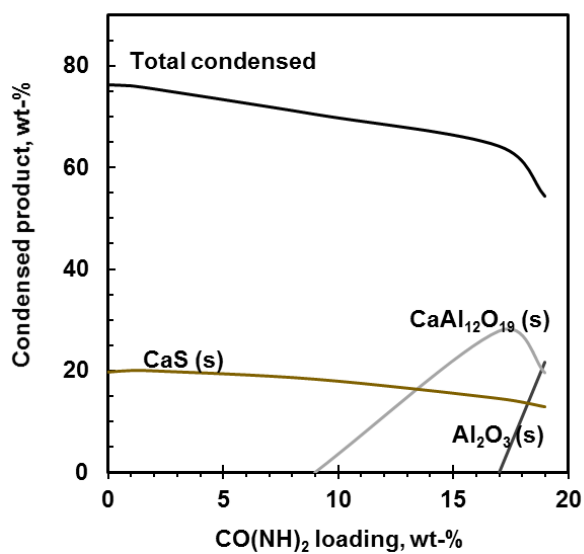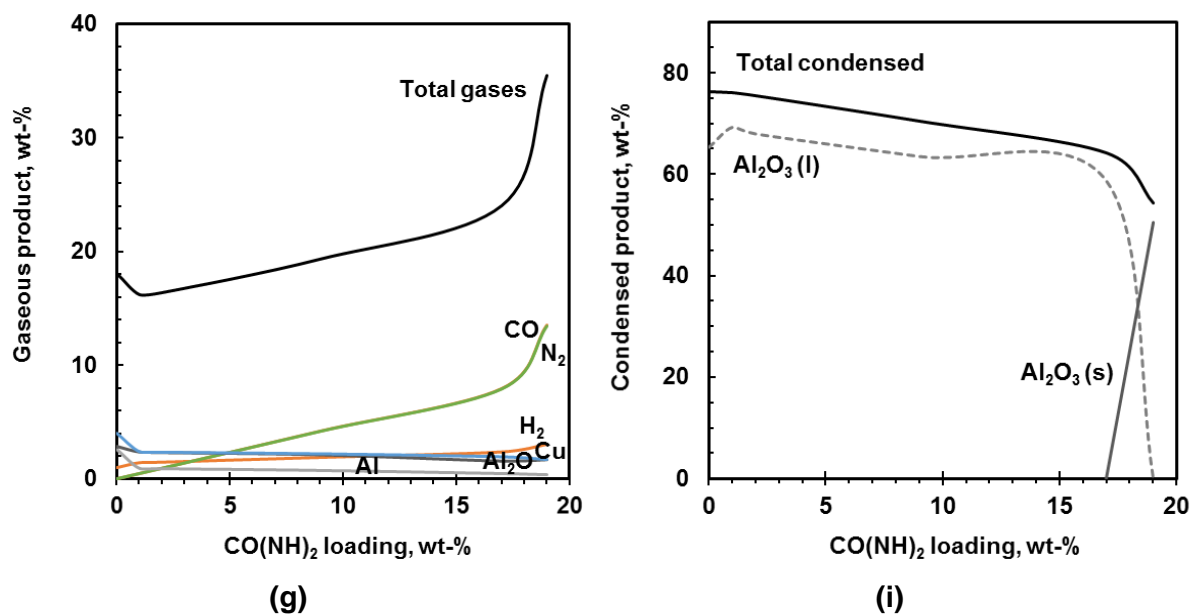
Figure 4-21: Gaseous and condensed products of (a) & (b) Base1, (c) & (d) Blend2,
(e) & (f) S4 and (g) & (i) CSP5 compositions containing CO(NH)$_2$ in FactSage

It can be seen that increasing the urea loading resulted in an increase in gaseous products
while there was a decrease in condensed products for all systems. The major gaseous
products present in Base1, Blend2, S4 and CSP5 containing urea in Figure 4-21a, Figure
4-21c, Figure 4-21e and Figure 4-21g respectively are hydrogen (H$_2$), aluminium oxide (Al$_2$O),
carbon monoxide (CO), nitrogen (N$_2$). Main condensed products for the compositions with
urea include aluminium trioxide (Al$_2$O$_3$), calcium sulfide (CaS) and monocalcium hexa-
aluminate (CaO·6Al$_2$O$_3$).

Chapter 5: Characterisation of raw materials

5.1. Elemental composition

Table 5-1 and Table 5-2 show the elemental composition of aluminium and calcium sulfate hemihydrate respectively.

Table 5-1: Mass elemental composition of atomised aluminium by XRF analysis

Element*	Al	Mg	Fe	Si	Na	P	V	Ga	Ti	Total
wt-%	99.59	0.2	0.07	0.04	0.04	0.01	0.01	0.01	0.01	99.98

*Impurities < 0.01 wt-% include Zr, Mn, Ca, K & Pr

Table 5-2: Mass elemental composition of calcium sulfate hemihydrate by XRF analysis

Element*	CaO	SO_3	MgO	SiO_2	Al_2O_3	Fe_2O_3	Cr_2O_3	LOI	Total
wt-%	39.60	54.30	1.67	0.52	0.11	0.06	0.01	3.71	99.97
wt-% (theoretical)	38.63	55.16						6.21	100

*Impurities < 0.01 wt-% include TiO_2, MnO, Na_2O, K_2O, P_2O_6, NiO, V_2O_6, ZrO_2 & CuO

Table 5-1 shows that the raw material Al contains no significant contaminants. Loss on ignition studies on $CaSO_4 \cdot 0.5H_2O$ showed that the raw material lost 3.71 wt-% upon roasting at 1000 °C, which should theoretically be 6.21 wt-%. The measured CaO and SO_3 content measured compared relatively well with theoretical values. The presence of 1.67 wt-% MgO was the most significant impurity. The remaining XRF analysis of raw materials is compiled in Appendix A.

5.2. Compound composition

Figure 5-1 is a diffractogram obtained from X-Ray diffraction analysis of the raw materials.
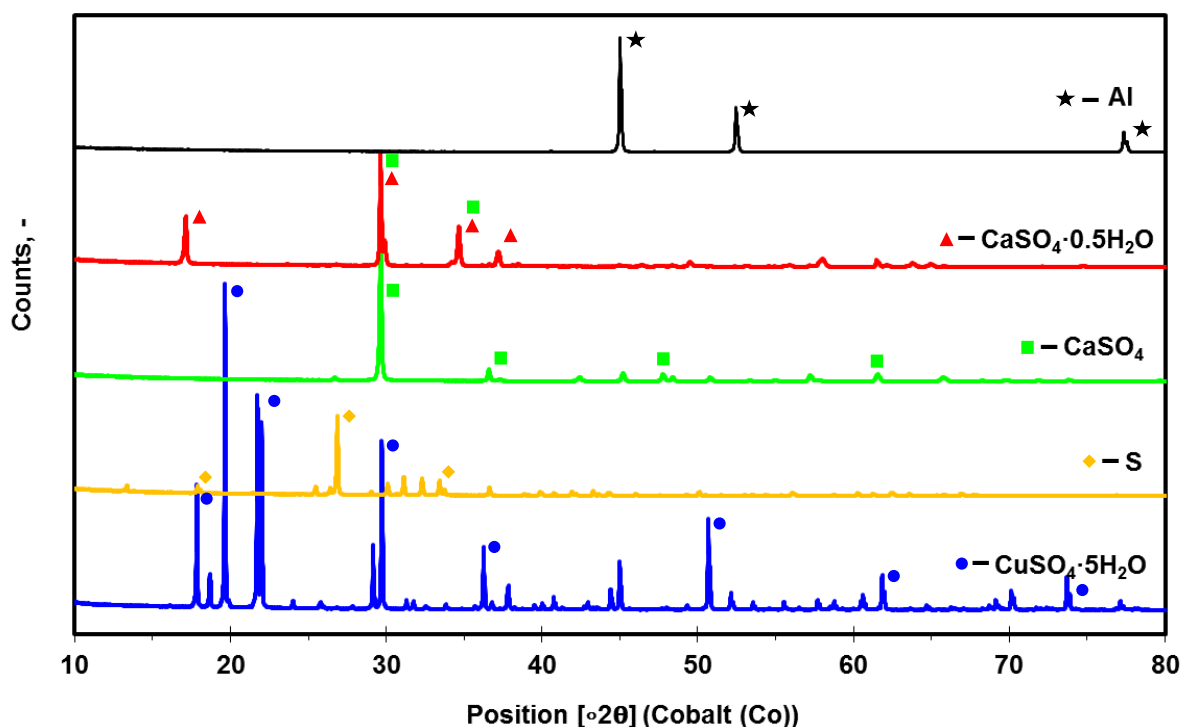
Figure 5-1: Diffractogram of raw materials

Figure 5-1 shows that aluminium, anhydrous calcium sulfate, sulfur and copper sulfate pentahydrate raw materials were essentially crystallographically pure. On the other hand, the raw Plaster of Paris contained up to 85 wt-% bassanite ($CaSO_4 \cdot 0.5H_2O$) according to the analysis.

5.3. Particle size distribution and D$_{50}$

Figure 5-2 shows the particle size distributions for the raw materials aluminium (Al), calcium sulfate hemihydrate ($CaSO_4 \cdot 0.5H_2O$), calcium sulfate anhydrite ($CaSO_4$), sulfur (S), sodium borosilicate glass spheres ($SiO_2/Na_2O/B$) and urea ($CO(NH)_2$). Copper sulfate pentahydrate ($CuSO_4 \cdot 5H_2O$) was run in the Mastersizer, however dissolved too quickly to obtain a reliable result. The relatively large error bars for $CaSO_4 \cdot 0.5H_2O$, $CaSO_4$ and $CO(NH)_2$ in Figure 5-2b, Figure 5-2c and Figure 5-2f are attributed to the materials dissolving or reacting in the water dispersant used in the Mastersizer and are presented only as a rough estimate of the particle size distribution. There was no access to dry dispersion techniques, which would have provided a more accurate result.

(a) Al

(b) CaSO$_4$·0.5H$_2$O

(c) CaSO$_4$

(d) S

(e) SiO$_2$/Na$_2$O/B

(f) CO(NH)$_2$
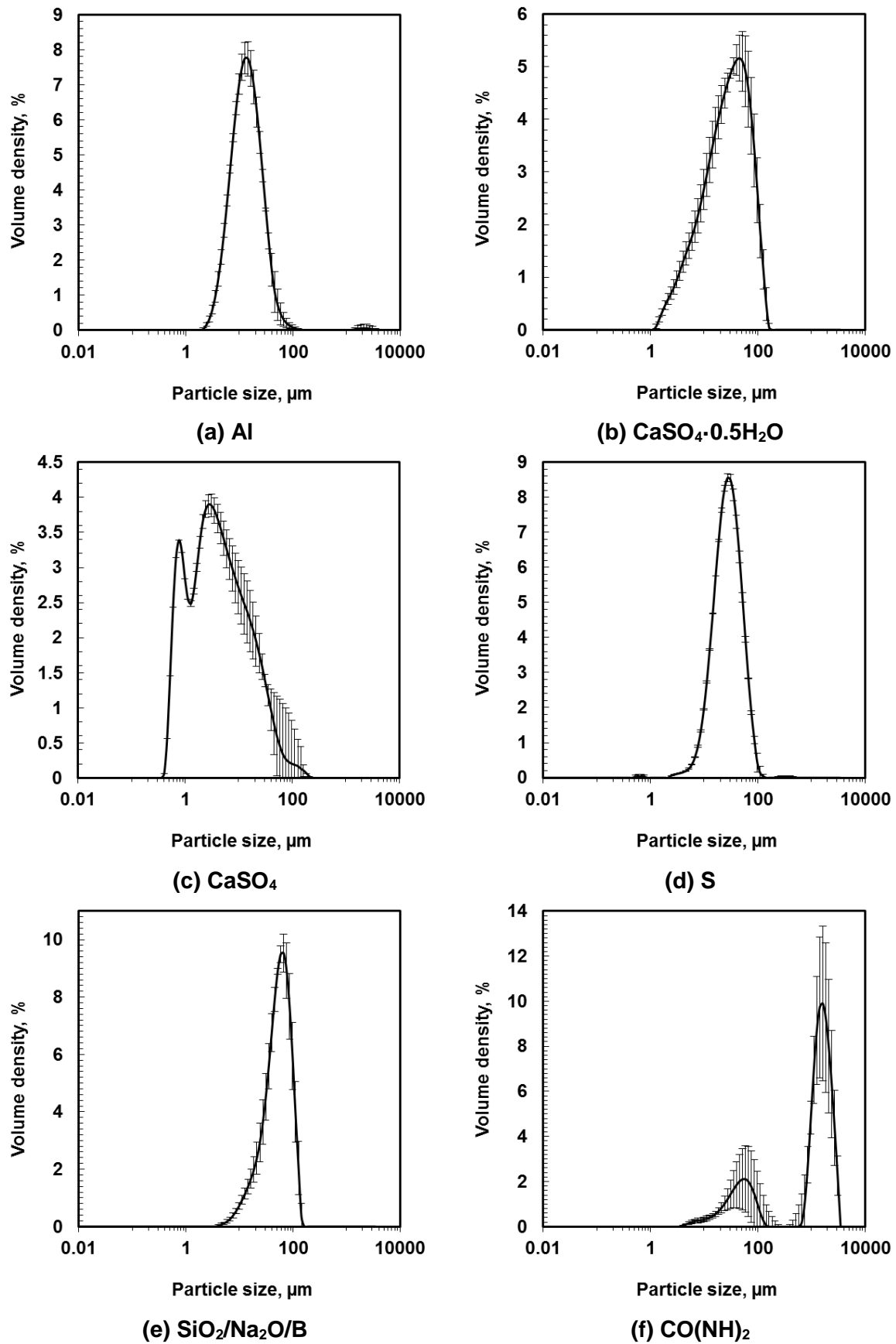
Figure 5-2: Particle size distributions (a) – (f) of raw materials

Table 5-3 shows a summary of the average particle size (D_{50}) as well as D_{10} and D_{90} values obtained from Mastersizer runs.

Table 5-3: Summary of D_{10}, D_{50} and D_{90} of raw materials

Raw material	D_{10} (µm)	D_{50} (µm)	D_{90} (µm)
Al	5.5 ± 0.2	13 ± 0	29 ± 3
$CaSO_4$	0.90 ± 0.26	4.5 ± 2	23 ± 8
$CaSO_4·0.5H_2O$	6.0 ± 1.0	30 ± 5	85 ± 7
S	13 ± 0	29 ± 0	60 ± 1
$SiO_2/Na_2O/B$	22 ± 3	57 ± 5	103 ± 7.
$CO(NH)_2$	39 ± 3	1430 ± 3	2530 ± 3

5.4. Particle morphology and shape

Scanning Electron Microscopy (SEM) images for the raw materials in Figure 5-3.
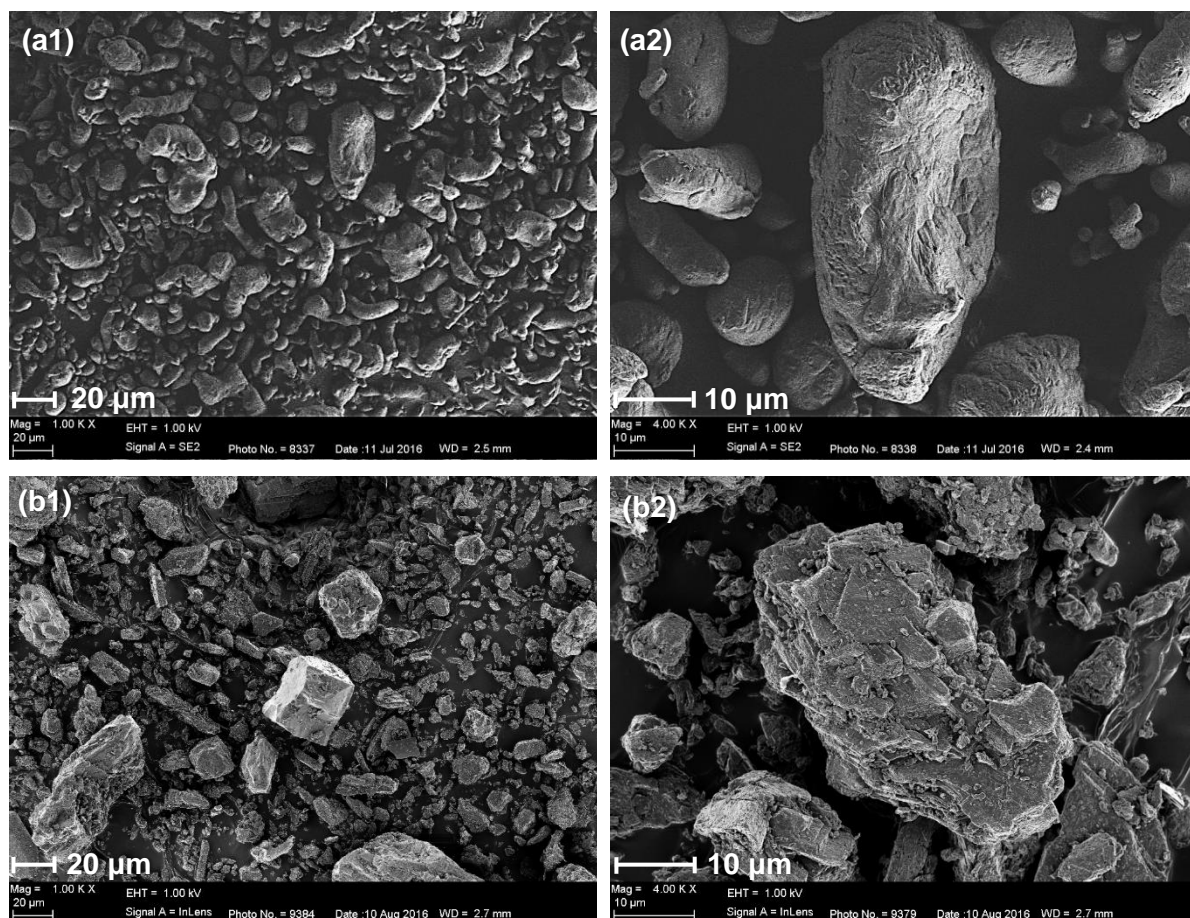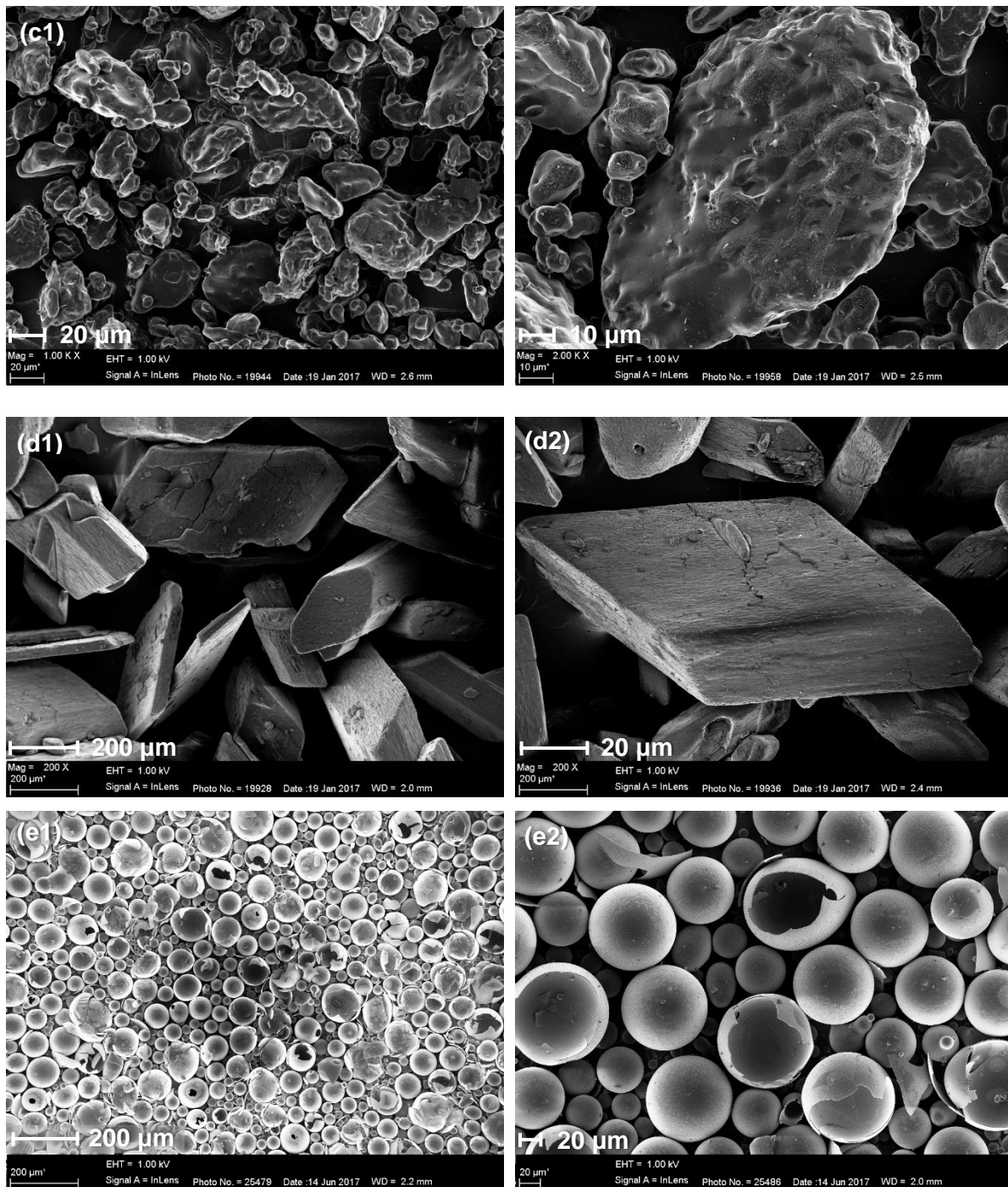
Figure 5-3: SEM images of raw materials (a) Al, (b) CaSO$_4$·0.5H$_2$O, (c) S, (d) CuSO$_4$·0.5H$_2$O and (e) SiO$_2$/Na$_2$O/B

Figure 5-3a shows aluminium particles that were oval, cylindrical and globular in shape. Calcium sulfate hemihydrate particles are seen in Figure 5-3b, which varied between idiomorphic and flaky crystals. This means that the calcium sulfate from the supplier contained both the α-hemihydrate and β-hemihydrate. Sulfur particles are shown in Figure 5-3c, indicating their round and flat crystal morphology. Figure 5-3d shows the orthorhombic- and trigonal-shaped crystals of copper sulfate pentahydrate. Sodium borosilicate glass spheres are shown in Figure 5-3e. It is observed that not all the glass spheres are intact as some have cracked and broken into pieces.

5.5. Specific surface area

The BET surface areas of raw materials is shown in Table 5-4. The largest specific surface area of 2.52 m^2 g^{-1} is for anhydrous calcium sulfate $CaSO_4$. The smallest specific surface area of 0.17 m^2 g^{-1} is for aluminium.

Table 5-4: BET surface area of raw materials

Raw material	Al	$CaSO_4$	$CaSO_4 \cdot 0.5H_2O$	S
BET surface area (m^2 g^{-1})	0.17	2.52	2.13	1.45

5.6. Infrared spectroscopy

Fourier Transform-Infrared spectroscopy (FTIR) was performed on the raw materials and associated spectra are shown in Figure 5-4.
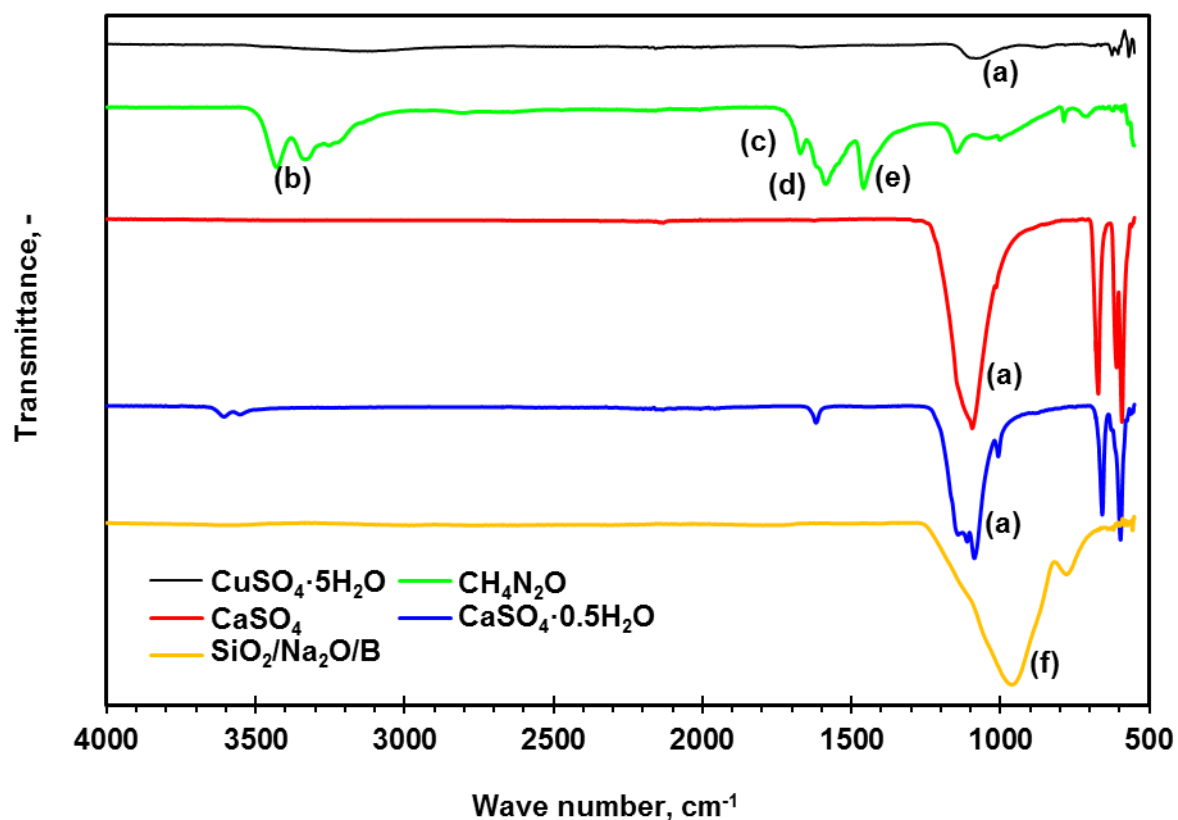
Figure 5-4: FTIR spectroscopy of raw materials

Table 5-5 shows the structural features of the raw materials corresponding to the bands in Figure 5-4.

Table 5-5: Characteristic features of raw materials from FTIR analysis

Band ID	Wave number (cm^{-1})	Functional group
(a)	1080/680 – 610	SO_4^{2-}
(b)	3500 – 3100	N-H stretch
(c)	1690 – 1640	C=O stretch
(d)	1640 – 1550	N-H bending
(e)	1453	C-N stretch
(f)	1100 – 900	SiO_4^{4-}

5.7. Differential thermal analysis

The thermal decomposition of the raw materials was determined using differential thermal analysis shown in Figure 5-5.
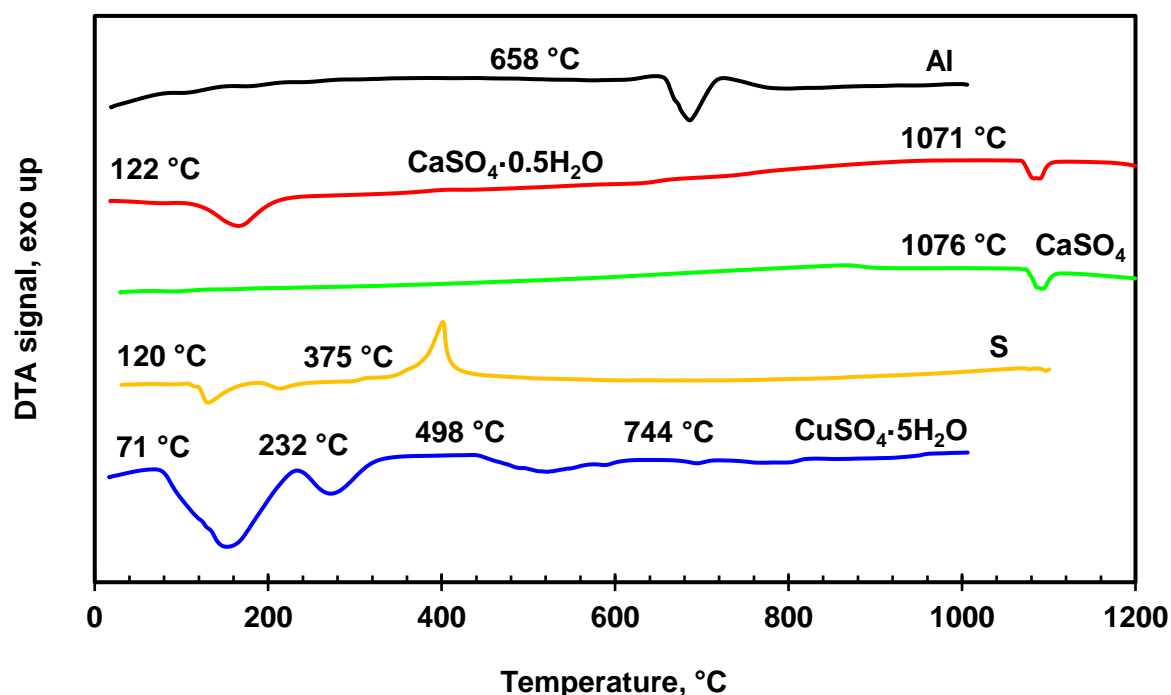
Figure 5-5: Differential thermal analysis of raw materials

Differential thermal analysis in Figure 5-5 shows that aluminium onset temperature for the melting endotherm was about 658 °C. The first endotherm produced by calcium sulfate hemihydrate at 122 °C is attributed to the loss of water from the compound. Next at the second, anhydrous calcium sulfate decomposed at a much higher temperature of 1071 °C. The raw material anhydrous calcium sulfate decomposed similar to calcium sulfate hemihydrate after it has lost its water. Sulfur melted at the endotherm onset temperature of 120 °C but was found to produce an exotherm at 375 °C. This may have been because of a leak in the argon gas line, as the runs were repeated and the same exotherm was observed. If there was a leak and oxygen had infiltrated the system, then sulfur may have reacted with oxygen to release energy in forming sulfur dioxide. A large exotherm was present at 71 °C for copper sulfate pentahydrate indicative of at least three and a half water of hydration being drawn off, according to measurements described by El-Houte et al (1989). The half molecule of water is drawn off at around 85 °C. The smaller endotherm at 232 °C could be the loss of the last remaining water in the compound. There is another endotherm present at 744 °C indicating the formation of CuO.

Chapter 6: Results and discussions

6.1. Determining optimum compositions

6.1.1. Casting at different water loadings without fuel

Different water loadings were added to calcium sulfate hemihydrate to investigate its effect on mixing and setting. The mole ratio of calcium sulfate hemihydrate ($CaSO_4·0.5H_2O$) to water (H_2O) was varied randomly in casts without fuel. Table 6-1 shows the mole ratios, mass ratios and observations of the cast made with time.

Table 6-1: Observations of casting without fuel at different water loadings

Mole ratio[a]	Mass ratio[b]	Observations T₀ = 0 s	T₁ = 1 h	T₂ = 2 h	T₃ = 3 h
1:2	1:0.26	Granular, crumbs. Not enough water.	Granular	Granular	Granular
1:4	1:0.52	Very thick, already a paste	Firm	Firm	Firm
1:6	1:0.74	Starting to form paste.	Setting	Firm	Firm
1:8	1:1	Good mixing.	Less watery than 1	Setting with some water.	Less water remaining than 1:10.
1:10	1:1.23	Watery, excess water.	Watery	Setting, with some water	Some water remaining

[a]Mole hemihydrate to mole water; [b]Mass hemihydrate to mass water

Even though all water loadings were in excess of the theoretical mass of water required, it was found that they made a difference to the mixing and setting of the cast. Table 6-1 shows that a mole ratio of 1:2, i.e. mass ratio of 1:0.26, was insufficient to combine $CaSO_4·0.5H_2O$ to form a paste that would set as whole solid cast. It was further noted that it was difficult to shape compositions that were too thick, as they set too fast and a smooth surface could not be obtained.

Table 6-1 shows that the best water loading for mixing of the cast without fuel was the mole ratio of 1:8, i.e. a mass ratio of 1:1. Considering that fuel and additives were still to be added, it was assumed that a mole ratio of calcium sulfate hemihydrate to water of 1:10 would be even better suited.

The calcium sulfate dihydrate casts were crushed gently with a pestle in a mortar. Figure 6-1 shows Scanning Electron Microscopy (SEM) images of the calcium sulfate dihydrate casts without fuel at the two optimum water loadings.
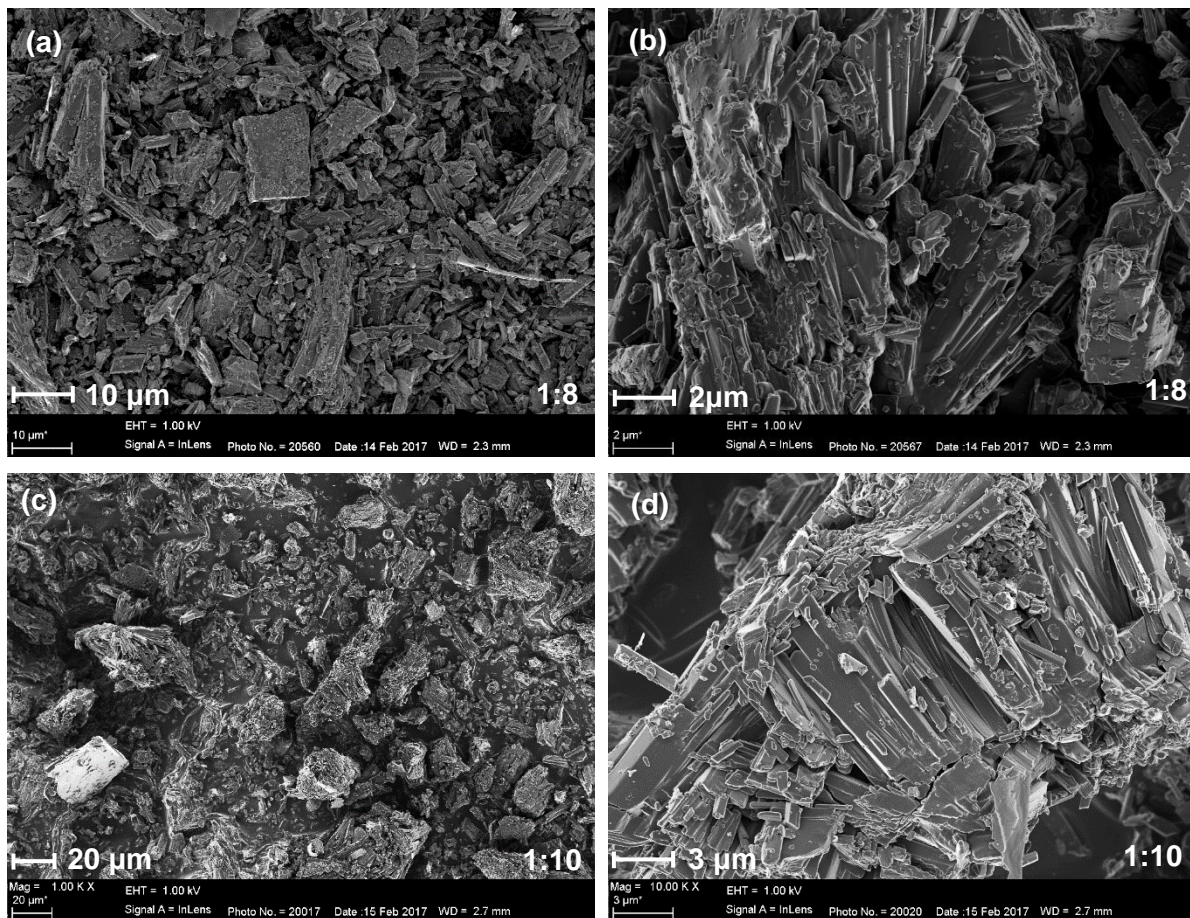
Figure 6-1: SEM images of calcium sulfate dihydrate at mole ratios (a), (b) 1:8 and (c), (d) 1:10

It can be seen that calcium sulfate hemihydrate (shown in Figure Figure 5-3b) had converted to calcium sulfate dihydrate shown in Figure 6-1. This is due to the presence of the interlocking mass of crystals that is characteristic of $CaSO_4 \cdot 2H_2O$ crystals.

6.1.2. Optimum compositions and water loadings with fuel used for casting

Base1 was the base case composition containing 60 wt-% calcium sulfate dihydrate with 40 wt-% aluminium. This was determined from EKVI simulations where the content of oxidiser and fuel was varied and the optimum composition corresponded to the maximum reaction temperature. The same was done to obtain the optimum compositions for S4 and CSP5.

For the case of Blend2, however, the composition corresponding to the maximum reaction temperature did not hold well enough upon casting. It seemed to contain too little $CaSO_4 \cdot 0.5H_2O$ that could react with water to form the stronger $CaSO_4 \cdot 2H_2O$ and broke when being removed from the mould. The optimum composition of Blend2 was obtained by casting various compositions from EKVI with water. The best setting and strongest cast with the highest reaction temperature was 30 wt-% $CaSO_4 \cdot 2H_2O$, 30 wt-% $CaSO_4$ and 40 wt-% Al.

The fuel, oxidiser and additive contents, for the Base1, Blend2, S4 and CSP5 compositions, are shown in Table 6-2. Additionally, the optimum mole ratio of calcium sulfate hemihydrate ($CaSO_4 \cdot 0.5H_2O$) to water (H_2O) to ensure good mixing and ease of casting is included. This is based on subjective assessments by the author.

Table 6-2: Optimum compositions and water loadings for Base1, Blend2, S4, and CSP5

Sample ID	Al (wt-%)	$CaSO_4 \cdot 2H_2O$ (wt-%)	$CaSO_4$ (wt-%)	S (wt-%)	$CuSO_4 \cdot 5H_2O$ (wt-%)	Mole ratio $CaSO_4 \cdot 0.5H_2O$: H_2O
Base1	40	60	-	-	-	1:10
Blend2	40	30	30	-	-	1:17
S4	30	50	-	20	-	1:10
CSP5	40	50	-	-	10	1:10

The optimum compositions on a weight percent basis are shown in Table 6-2. Additionally, the optimum water loading for Blend2 is greater than that of the other compositions. This is because it contains the least $CaSO_4 \cdot 2H_2O$ and thus the least $CaSO_4 \cdot 0.5H_2O$, from which the water loading was calculated.

Most laboratory tests were conducted using a total cast thermite mass of 5 g. As such, a summary of the mass compositions of Base1, Blend2, S4 and CSP5 is given in Table 6-3.

Table 6-3: Optimum mass compositions for 5 g total thermite after casting

Sample ID	Al (g)	$CaSO_4 \cdot 0.5H_2O$ (g)	$CaSO_4$ (g)	S (g)	$CuSO_4 \cdot 5H_2O$ (g)	Total (g)	H_2O (g)
Base1	2	2.53	-	-	-	4.53	3.14
Blend2	2	1.26	1.5	-	-	4.76	2.66
S4	1.5	2.11	-	1	-	4.61	2.62
CSP5	2	2.11	-	-	0.5	4.61	2.62

Table 6-3 shows that the total mass of thermite before casting was less than 5 g. Assuming 100 % conversion of calcium sulfate hemihydrate to calcium sulfate dihydrate, the addition of water would result in a maximum 5 g of cast thermite. The mass of $CaSO_4 \cdot 0.5H_2O$ was thus calculated from the mass of $CaSO_4 \cdot 2H_2O$ that should be present in the optimum composition.

Observations were made while mixing, casting and setting of the compositions. Casts were allowed to set for at least 3 days before conducting any tests. A composition based on magnesium as fuel instead of aluminium, called "Mg3", was attempted in addition to the abovementioned compositions with additives. The magnesium reacted too quickly with the water that was added to the system and formed many gas bubbles. The consequent cast foamed while setting and resulted in an extremely porous cast. This was discontinued from testing.

Sulfur is incompatible with water and consequently did not combine well with the water while casting. However, at the optimum composition in S4, water loading and with some mixing the powders did combine better. At times a layer of sulfur was present on the top of the sulfur casts, which may have been due to the incompatibility or difference in density resulting in settling out. It was noted that the presence of copper sulfate pentahydrate ($CuSO_4 \cdot 5H_2O$) resulted in the CSP5 casts setting much faster than the other compositions. It was also observed that with the CSP5 formulation strong casts were obtained. Copper sulfate is a stronger oxidant than calcium sulfate. The fortuitous discovery that it significantly accelerates the setting time of the gypsum, and also yields strong casts, obviated the need to consider other additives that could affect the setting rate.

6.2. Effect of additives on base case

6.2.1. Bulk and tapped density of powder compositions before casting

Bulk and tap density of the powder compositions were determined in glass vials with an inner diameter of 13 mm, outer diameter of 15 mm and height of 50 mm. The change in volume during the setting process was also conducted in these vials.

Powder compositions were tapped in the glass vials, and their heights were recorded at regular intervals. Figure 6-2a shows the densities corresponding to the tapped heights of each powder composition while Figure 6-2b shows a comparison of the bulk and tapped densities.
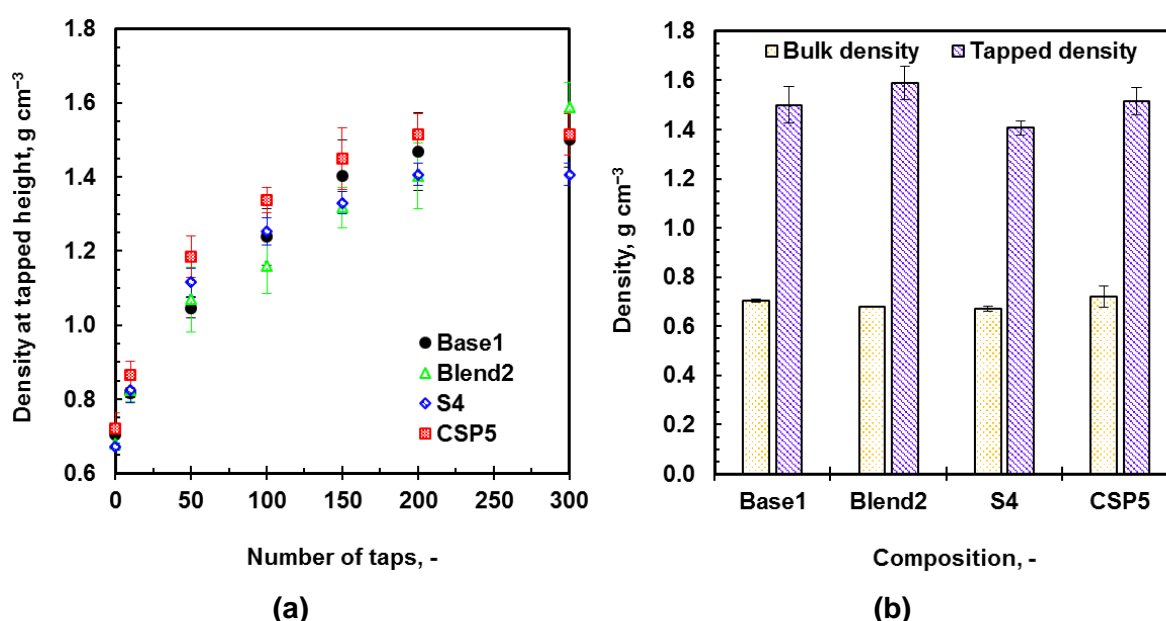
Figure 6-2: Calculated densities showing (a) density changes at different taps and
(b) comparison of bulk and tapped density (at tap-0 and tap-300)

It can be seen in Figure 6-2a that the density of each composition remained constant after about 200 taps. The bulk density was calculated at the height of the composition at tap-0 whiled the tapped density was calculated at the height of the composition at tap-300. Figure 6-2b shows the bulk and tapped density of Base1 was calculated to be 0.71 ± 0.01 g cm^{-3} and 1.50 ± 0.07 g cm^{-3} respectively. Similarly, for the Blend2 composition, the bulk and tapped density was 0.68 ± 0.00 g cm^{-3} and 1.59 ± 0.07 g cm^{-3}. For the S4 composition, the bulk and tapped density was 0.67 ± 0.01 g cm^{-3} and 1.41 ± 0.03 g cm^{-3}. Lastly, the bulk and tapped density for the CSP5 composition was 0.72 ± 0.04 g cm^{-3} and 1.52 ± 0.06 g cm^{-3} respectively.

The flowability of powders were investigated using the bulk and tapped density data. Carr's compressibility index and the Hausner ratio are measures of a powder's tendency to be compressed. These values indicate the extent of particle interactions and their tendency to settle, where free-flowing powders have insignificant interactions while poor-flowing powders have more significant interactions (The United States Pharmacopeia, 2010). The compressibility index was calculated by $(V_o - V_f) / V_o$ expressed as a percentage, where V_o is the initial or bulk volume and V_f is the final or tapped volume. The Hausner ratio was the ratio of the initial bulk volume to the final tapped volume (V_o / V_f). The bulk density and tapped density of free-flowing powders will not differ greatly. On the other hand, poorer-flowing powders will exhibit a larger difference between bulk and tapped densities (The United States Pharmacopeia, 2010).

Figure 6-3a and Figure 6-3b show Carr's compressibility index and the Hausner ratio of the powders respectively.
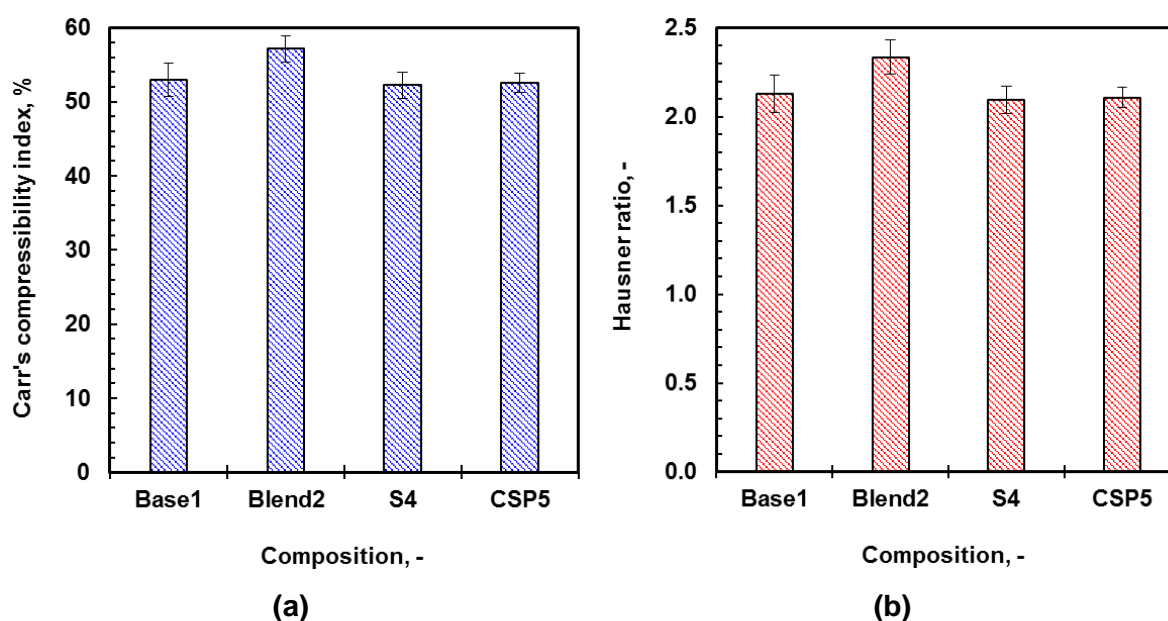
Figure 6-3: Flowability of powders determined by (a) Carr's compressibility index and (b) Hausner ratio

Both Figure 6-3a and Figure 6-3b indicate that all compositions possess very very poor flow character. This is since the compressibility index is greater than 38 % and the Hausner ratio is greater than 1.60 for all compositions (The United States Pharmacopeia, 2012). The very poor flow character of the powders indicates that there are more interactions between the particles. It could imply that the particles vary in shape and size, leading to better packing and fewer voids between particles.

The optimum amount of water (mass ratio of hemihydrate to water of 1:1.23) was added to the glass vials and the compositions were mixed. The initial volume of the cast was marked and after setting for at least 3 days, the final volume of the cast was recorded. The change in volume of the casts upon setting was determined and is shown in Figure 6-4.
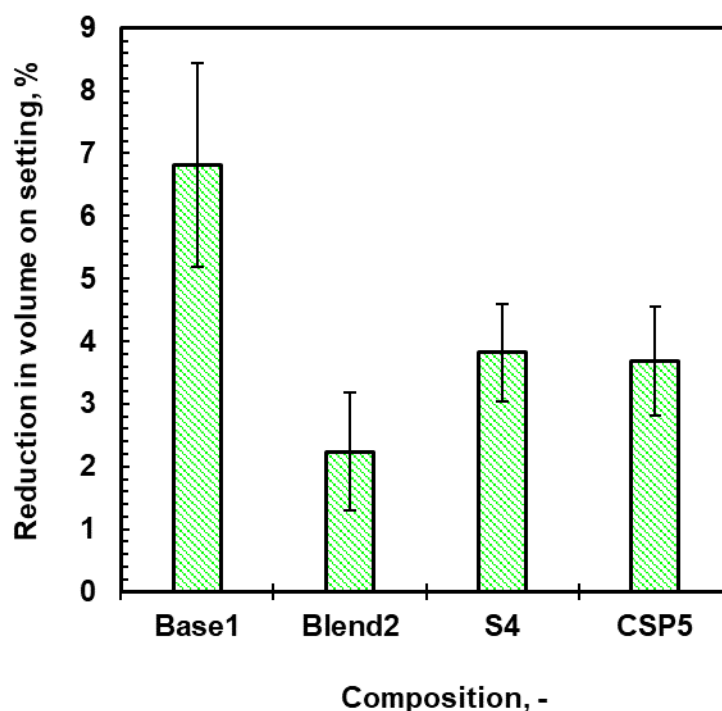
Figure 6-4: Change in volume of castings upon setting

Figure 6-4 shows that the largest volume change of 6.82 ± 1.62 cm^3 was for Base1 while the smallest volume change of 2.24 ± 0.95 cm^3 was for Blend2. This was expected, since the volume change occurs due to the dissolution of the hemihydrate in water. Thereafter, it recrystallises as dense, interlocking and fibrous calcium sulfate dihydrate when reacting with the water. The form changes from irregular particles to well-formed clusters of needle-like crystals. Blend2 contains less calcium sulfate hemihydrate than Base1 and thus fewer particles will be shifted during the reaction. Additionally, since aluminium reacts only very slowly with water, and calcium sulfate anhydrite is only slightly soluble in water, there are no other reactions taking place that could contribute to the volume change.

6.2.2. Hydration heat on setting of casts from heat calorimeter

The heat released when hydrating calcium sulfate hemihydrate to form calcium sulfate dihydrate was measured for each of the compositions using an isothermal heat calorimeter. The heat flow of the hydration was recorded over time and is shown in Figure 6-5.
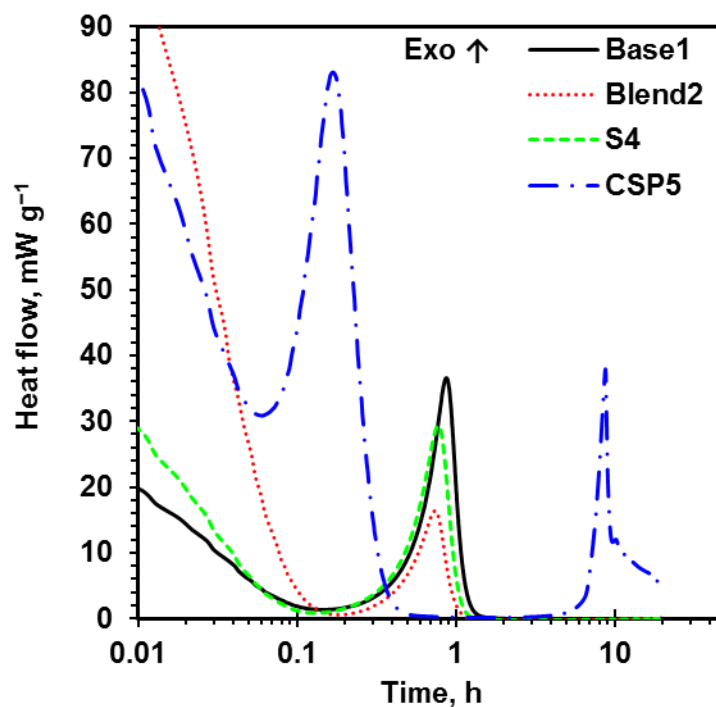
Figure 6-5: Heat flow observed during casting of various compositions over 20 h

Figure 6-5 shows the heat flow recorded over the total 20 h of the runs for each composition. There is an initial steep slope at t = 0.01 h, which is due to the heat transferred to the copper pots after the lids were removed and water was added. Both body heat and heat from the surroundings from opening the heat calorimeter lid contributed to this heat transfer, since the setup is extremely sensitive to changes.

Figure 6-5 shows the peak heat flow for Base1, Blend2 and S4 compositions occurred within an hour. The peak heat flow of Base1 was 38 ± 4.3 mW g^{-1} at 53 ± 0.17 min. Similarly, the peak heat flow for Blend2 was 17 ± 1.9 mW g^{-1} at 46 ± 2.0 min and S4 was 30 ± 3.0 mW g^{-1} at 46 ± 0.58 min. In contrast, the heat release of CSP5 differed vastly from the other compositions since it had two peak heat flows, the first occurring within 10 ± 2.1 min at 86 ± 10 mW g^{-1} and the second occurring at 8.8 ± 0.034 h at 39 ± 4.8 mW g^{-1}. Observations while casting in the laboratory revealed that CSP5 set faster than the other compositions and this was confirmed by heat calorimetry results. It is speculated that the second heat flow peak can be attributed to an interaction of the copper sulfate, in the composition, with the surface

of the copper pot. It was observed that the copper pots were shiny when the compositions were removed from the pots after 20 h.

The heat of hydration was calculated by obtaining the area under the heat flow curves at the peak heat flow. The peak heat flow, peak heat flow time and heat of hydration for the different compositions are summarised in Table 6-4.

Table 6-4: Summary of heats of hydration from isothermal heat calorimeter

Sample ID with reactants	Peak heat flow (W kg^{-1})	Peak heat flow time (min)	Hydration heat at 25 °C (J g^{-1})
Base1: Al+CaSO$_4$·2H$_2$O	38 ± 4	53 ± 0	59 ± 8
Blend2: Al+CaSO$_4$·2H$_2$O+CaSO$_4$	17 ± 2	46 ± 2	27 ± 4
S4: Al+CaSO$_4$·2H$_2$O+S	30 ± 3	46 ± 1	45 ± 5
CSP5: Al+CaSO$_4$·2H$_2$O+CuSO$_4$·5H$_2$O	86 ± 10	10 ± 2	49 ± 4

Literature has shown the hydration heat of α-hemihydrate and β-hemihydrate at 25 °C to be 112 ± 1 J g^{-1} and 100 ± 1 J g^{-1} respectively (Tydlität et al., 2008). Table 6-4 shows that Base1, containing hydrated CaSO$_4$·0.5H$_2$O and Al, released a heat of hydration of 59 ± 8 J g^{-1}. Blend2 released the smallest hydration heat at 27 ± 4 J g^{-1} while S4 resulted in a hydration heat of 45 ± 5 J g^{-1}. The first heat flow peak produced by CSP5 resulted in a heat of hydration of 49 ± 4 J g^{-1}. The second heat flow of CPS5 did not appear to be complete even after 20 h, indicating that it was probably associated with corrosion of the copper pots. Within the uncertainties associated with the measurements, the values for the hydration energies scale with the calcium sulfate hemihydrate content in each formulation.

6.2.3. Compressive strength after casting

Cylindrical casts were used to test the compressive strength. The compressive strength (MPa) of Base1, Blend2, S4 and CSP5 is shown in Table 6-5.

Table 6-5: Compressive strengths of Base1, Blend2, S4 and CSP5

Sample ID	Base1	Blend2	S4	CSP5
Compressive strength (MPa)	2.85 ± 0.20	2.33 ± 0.28	3.38 ± 0.31	4.61 ± 0.24

It was found that the inclusion of additives to the base case affected the compressive strength of the cast. Table 6-5 shows the compressive strength, or the load at which the cast broke, of composition Base1 was 2.85 ± 0.20 MPa. The inclusion of the copper sulfate pentahydrate additive in CSP5 produced a cast with the highest compressive strength of 4.61 ± 0.24 MPa. The reason for this is not currently understood. Unexpectedly, the addition of sulfur in S4 also increased the compressive strength of the base case, but to a lesser extent than CSP5, to 3.38 ± 0.31 MPa. In contrast, the addition of anhydrous calcium sulfate in Blend2 resulted in a casting with a lower compressive strength than Base1 of 2.33 ± 0.28 MPa. This was expected since the interlocking crystal structure of $CaSO_4·2H_2O$ is inherently strong and, since Blend2 contains less $CaSO_4·2H_2O$, Blend2 would be less strong that the other compositions.

Figure 6-6 shows the fracture pattern obtained at load failure for (a) Base1, (b) Blend2, (c) S4 and (d) CSP5 respectively. A cone fracture was observed for all compositions.
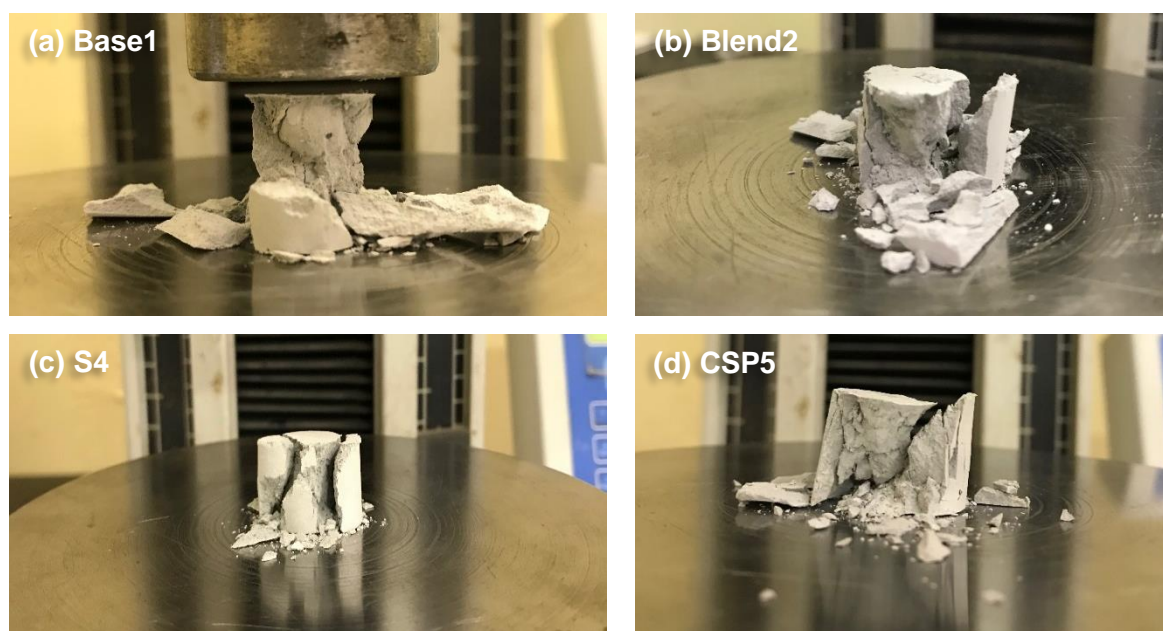
Figure 6-6: Fracture patterns at load failures from compressive strength tests

6.2.4. Specific surface area

The BET surface areas of Base1, Blend2, S4 and CSP5 compositions are listed in Table 6-6. The Blend2 composition possessed the largest surface area of 0.95 m^2 g^{-1}.

Table 6-6: BET surface areas of Base1, Blend2, S4 and CSP5

Sample ID	Base1	Blend2	S4	CSP5
BET surface area (m^2 g^{-1})	0.50	0.95	0.24	0.62

6.2.5. Linear burn rates and maximum surface temperature of Base1, Blend2, S4 and CSP5

Open air burn tests in the laboratory were conducted on alumina tiles and clay bricks where necessary. Burn rates, of casts approximately 5 g in mass and half-cylinder in shape, are shown in Figure 6-7.
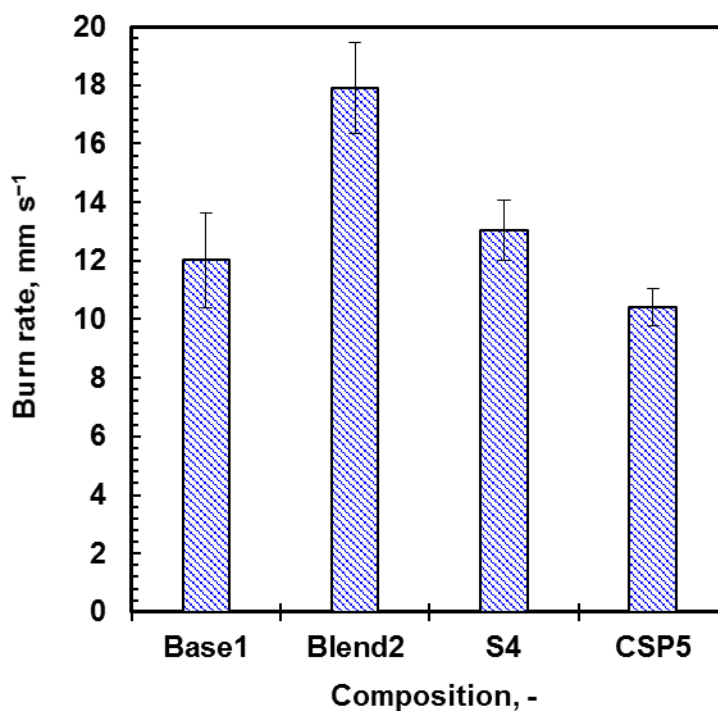
Figure 6-7: Burn rates of Base1, Blend2, S4 and CSP5 compositions

Figure 6-7 shows that Base1 burned at a rate of 12.0 ± 1.6 mm s^{-1}. The S4 composition burned at a rate faster than that at 13.0 ± 1.0 mm s^{-1}. The fastest burn rate of 17.9 ± 1.6 mm s^{-1} was achieved by the Blend2 thermite composition. This is expected since the composition contains less calcium sulfate dihydrate ($CaSO_4 \cdot 2H_2O$). This could indicate that less time and energy was spent driving off the hydration waters of $CaSO_4 \cdot 2H_2O$. The slowest burning composition

was CSP5 at 10.4 ± 0.6 mm s^{-1}. This can be explained by the fact that initially energy both copper sulfate pentahydrate ($CuSO_4 \cdot 5H_2O$) and $CaSO_4 \cdot 2H_2O$ would need to be decomposed to release their waters and oxygens, which would take some time before the reaction could proceed.

Figure 6-8 shows the progression of the casts being burned from ignition to completion. Alumina tiles were used to house and contain burn residues for collection.

(a) Base1

(b) Blend2

(c) S4
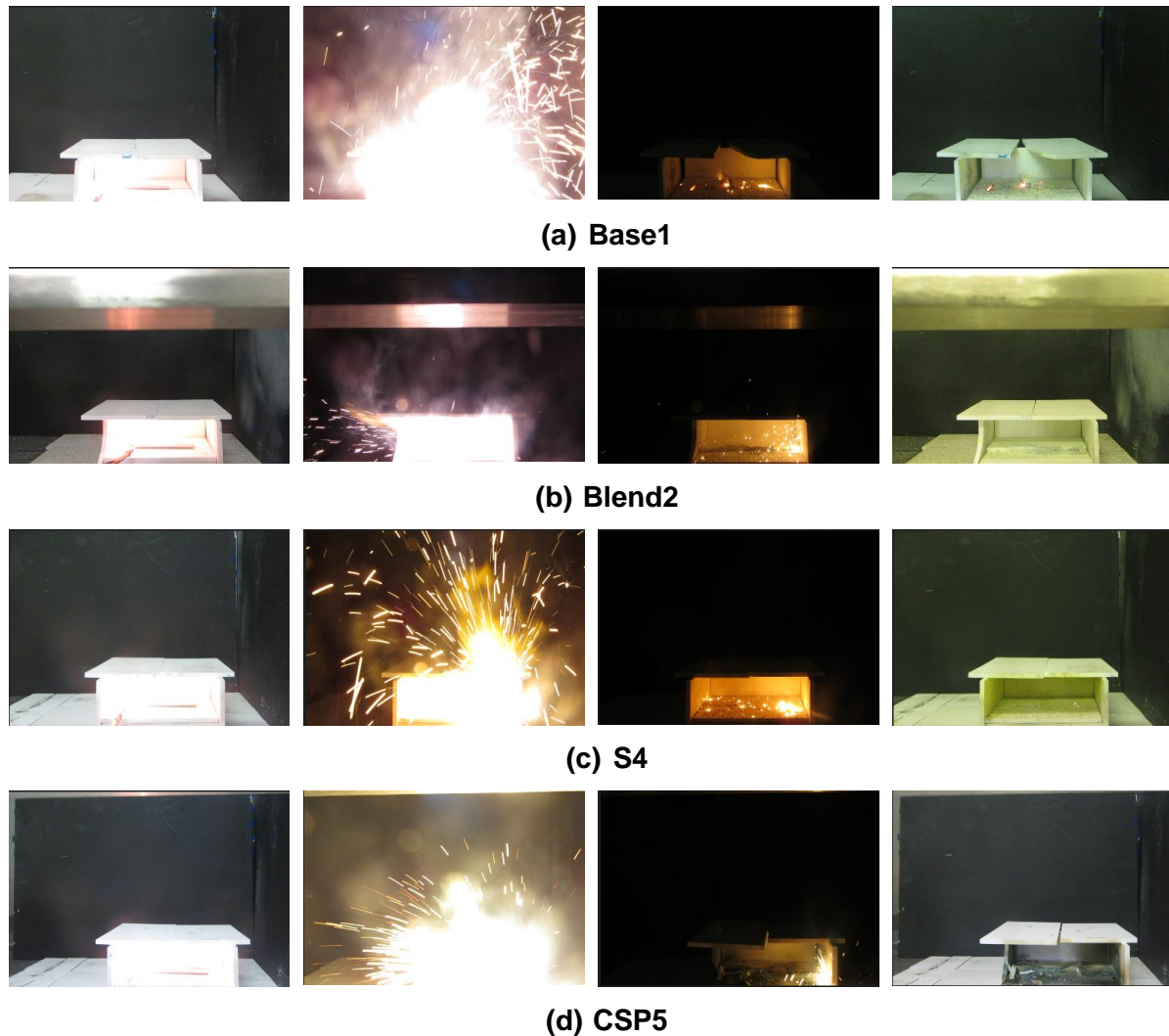
(d) CSP5

Figure 6-8: Progression of open air burn tests for (a) Base1, (b) Blend2, (c) S4 and (d) CSP5 thermites

The burn residues collected from open air burn tests are shown in Figure 6-9.

| (a) | (b) | (c) | (d) |

Figure 6-9: Burn residues collected after open air burn tests for (a) Base1, (b) Blend2, (c) S4 and (d) CSP5

Figure 6-8a shows that Base1 casts sometimes cracked and moved sections of the alumina tiles on which they burnt, leaving a white and pale yellow powder residue. Figure 6-9a shows the small molten spheres that Base1 left behind on the tiles and the surrounding area where the sparks had reached. Similarly, Figure 6-8b shows that Blend2 also broke alumina tiles at times. Blend2 left a white and pale yellow powder residue on the tiles with small molten spheres. It can be seen in Figure 6-9b that the burn residue of Blend2 was finer and contained less molten spheres than Base1.

S4 seemed to ignite quickly and burned with a spray of sparks, see Figure 6-8c. Figure 6-9c shows that there were many large molten spherical particles produced as well as a sticky bright yellow residue left behind on the alumina tiles. A sulfur dioxide/hydrogen sulfide rotten egg smell was observed during burn tests for all compositions. However, the smell was particularly strong for the S4 composition after burn tests and in the burn residues that were collected.

CSP5 burned with a green flame at a rate slower than the other compositions. It produced a dark blue-green powder residue as shown in Figure 6-8d and Figure 6-9d. CSP5 casts broke the alumina tiles, so much so that it sprayed the tiles outwards as it burned. It is assumed that this was because a hotter slag was produced. It was then that tests were moved to clay bricks. It was noted that the slag stayed hot for a longer time after the reaction completed.

The maximum surface temperature and temperature profiles recorded by the pyrometer of Base1, Blend2, S4 and CSP5 are shown in Figure 6-10a and Figure 6-10c. The reproducibility of the burning of Base1 is shown in Figure 6-10b.
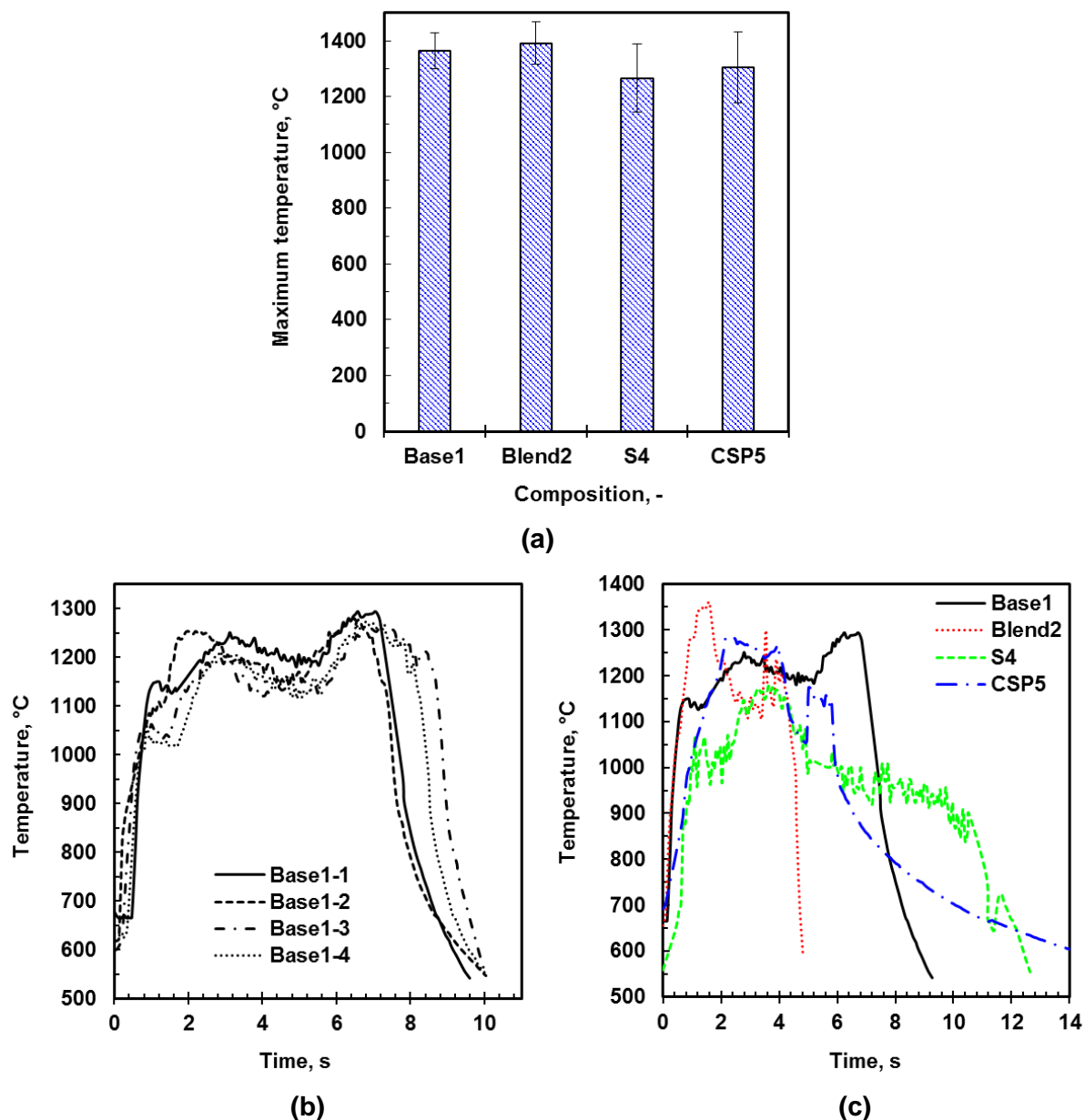
Figure 6-10: The (a) maximum surface temperatures, (b) reproducibility of Base1 temperature profile and (c) temperature profiles of Base1, Blend2, S4 and CSP5

Figure 6-10a shows the maximum surface temperature recorded by the pyrometer was 1392 ± 76 °C for the Blend2 composition. This was followed by Base1 at 1365 ± 64 °C and CSP5 at 1304 ± 126 °C. The pyrometer was directed at the middle of a cast and measurements were recorded at this point. It is assumed that the variability of this point between casts resulted in the large errors.

The reproducibility of the burning of the Base1 composition is shown in Figure 6-10b and the temperature profiles of each thermite composition is shown in Figure 6-10c. The composition Blend2 burned the fastest (shortest) while CSP5 burnt the slowest (longest). The gradual decreasing slope produced by CSP5 at the end of its burn is attributed to the hot cohesive slag that formed during burning that slowly lost its heat. In contrast, Base1 and Blend2 show an immediate drop in temperature upon completion of burning as they did not form large amounts of slag. The residues of all the compositions, except CSP5, were granular.

A summary of the burn rates, maximum temperatures and observation made during open air burn tests for Base1, Blend2, S4 and CSP5 thermites is given in Table 6-7.

Table 6-7: Summary of burn rates for Base1, Blend2, S4 and CSP5 thermites

Sample ID	Linear burn rate (mm s^{-1})	Maximum temperature (°C)	Observations from burn tests on alumina tiles
Base1	12.0 ± 1.6	1365 ± 64	White and yellow residues. Molten metal spheres, slag.
Blend2	17.9 ± 1.6	1392 ± 77	White and yellow residues. Less molten spheres than Base1.
S4	13.0 ± 1.0	1266 ± 121	Sticky bright yellow residue. Larger molten spheres, slag.
CSP5	10.4 ± 0.6	1304 ± 126	Dark blue-green residue. Broke, sprayed alumina tiles (because of hotter slag). Switched to brick.

6.2.6. XRD phase analysis and SEM images of base case burn residues

The XRD phase analysis of the burn residues collected is shown in Table 6-8.

Table 6-8: XRD phase analysis of burn residues collected from base case compositions

Burn product	Base1	Blend2	S4	CSP5
Al_2O_3	11	11	45	53
$CaO \cdot 6Al_2O_3$	24	43	5	13
$CaO \cdot 2Al_2O_3$	47	22	20	25
CaS	15	22	29	9
Al	2	3	0	0
Total (wt-%)	**100**	**100**	**100**	**100**
Measured Al/Ca[*]	2.10	1.98	1.65	4.27
Expected Al/Ca[*]	2.86	2.53	2.58	3.44

[*]Mass ratio

Table 6-8 shows that for all compositions the main condensed products collected from burn tests were aluminium oxide (Al_2O_3), monocalcium dialuminate ($CaO \cdot 2Al_2O_3$) and aluminium (Al). For Base1, the most predominant product was 47 wt-% $CaO \cdot 2Al_2O_3$ while for Blend2 it was 43 wt-% monocalcium hexa-aluminate ($CaO \cdot 6Al_2O_3$). In contrast, the most prominent burn product for S4 and CSP5 was 45 wt-% and 53 wt-% Al_2O_3 respectively.

In comparison, the major condensed products predicted from EKVI simulations for all compositions were Al_2O_3 (l) and CaS (s). For Base1, it was 69 wt-% Al_2O_3 and 18 wt-% CaS while for Blend2 the major products were 65 wt-% Al_2O_3 and 20 wt-% CaS. Similarly, the major products for S4 were 55 wt-% Al_2O_3 and 20 wt-% CaS while for CSP5 it was 65 wt-% Al_2O_3 and 15 wt-% CaS.

The measured mass ratios of Al/Ca for each composition, given in Table 6-8, do not match those expected from theory. The measured and calculated ratios do not correlate and there is a large difference between them. The presence of multiple phases makes the systems very complicated. While the quantitative results are inaccurate, and extensive analysis would be required to obtain a more reliable result, the presence of the phases are true to the peaks identified in the diffractograms.

There is a discrepancy between the phases identified in XRD analysis of burn residues and the products predicted in EKVI simulations. However, one should keep in mind that EKVI predicts the equilibrium product spectrum at the adiabatic reaction temperature. In the actual burns, samples took a long time to cool down and additional reactions could have occurred in the process. In the end, the XRD results reflect the composition of the burn residues at room temperature instead of at the adiabatic reaction temperature. The differences observed between the samples could reflect differences in the temperature histories experienced during burning and cooling down.

Figure 6-11 shows SEM images of the burn residues collected from alumina tiles and clay bricks.
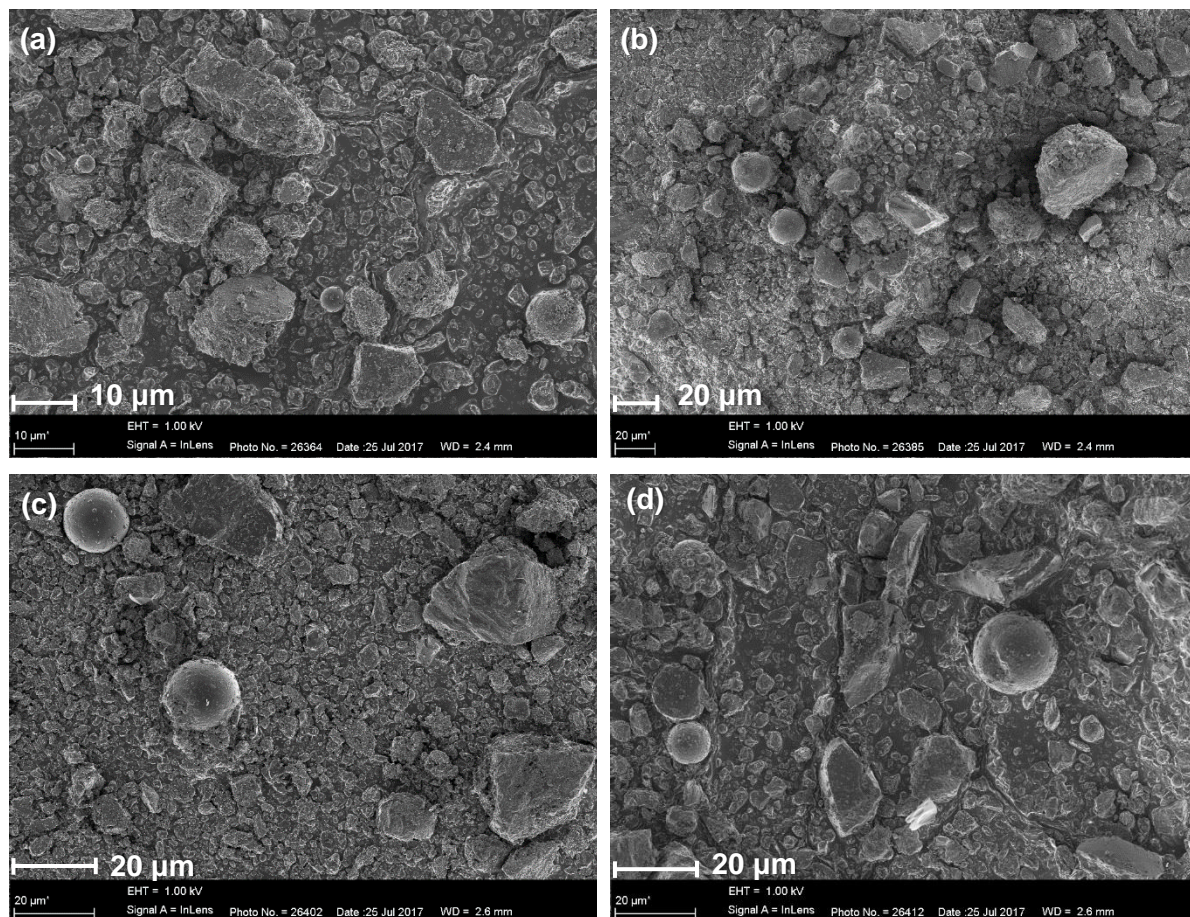
Figure 6-11: SEM images of burn residues of (a) Base1, (b) Blend2, (c) S4 and (d) CSP5

Spheres are visible in the SEM images for all compositions in Figure 6-11. This is indicative that part of the material did convert into a liquid phase, forming droplets that took on a spherical shape due to surface tension effects, which then solidified.

6.2.7. Energy output of compositions from bomb calorimeter

Experimental energy output of the compositions were determined from bomb calorimeter runs. A gross energy output was obtained after subtracting the energy contributions of the starters and the nichrome wire initiator. At constant volume, the heat of a system is equal to the internal energy of the system. The equation $dH = dU + d(PV)$ gives $dH = dU + VdP$ at a constant volume. Rearranging this, the internal energy ΔU can be calculated by $\Delta H - V\Delta P$. The specific enthalpy change ΔH and pressure change ΔP were determined from EKVI simulations at bomb calorimetry conditions of 3.0 MPa He in a 240 mL vessel.

The energy output of the systems obtained from EKVI and bomb calorimetry is compared in Figure 6-12.
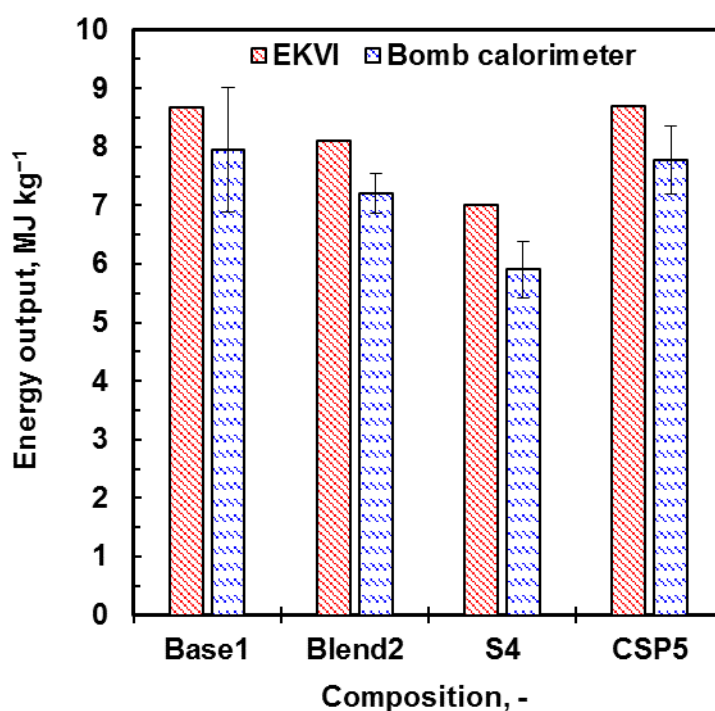
Figure 6-12: EKVI and bomb calorimeter energy outputs for Base1, Blend2, S4 and CSP5

Figure 6-12 shows that the bomb calorimeter energy output values were all less than the theoretical values predicted by EKVI. This was expected since the theoretical simulation was an ideal, adiabatic case while in the bomb calorimeter the reactions probably did not go to completion. The largest heat release was 7.96 ± 1.07 MJ kg^{-1} for Base1, which was closely followed by 7.78 ± 0.58 MJ kg^{-1} for CSP5. Blend2 resulted in a heat release of 7.21 ± 0.34 MJ kg^{-1}. Composition S4 produced the lowest heat release of 5.90 ± 0.48 MJ kg^{-1}. This shows that the presence of more water was not detrimental to the energy output of the systems.

6.2.8. Differential thermal analysis of base case with additives

Differential thermal analysis was conducted on all samples to identify chemical transformations. Of most interest was the melting onset temperature of the fuel, decomposition of the oxidiser and additive components as well as the onset temperature of the reaction of the thermite composition. Figure 6-13 shows the differential thermal analysis on Base1, Blend2, S4 and CSP5 compositions.
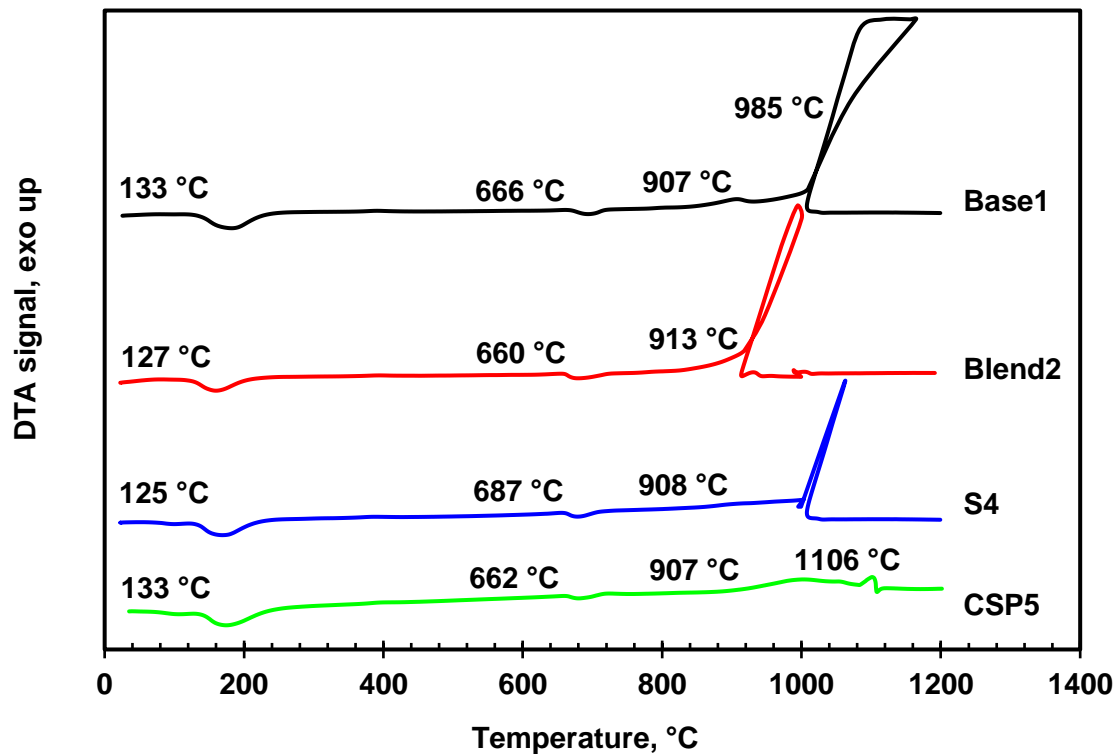
Figure 6-13: Differential thermal analysis of Base1, Blend2, S4 and CSP5

Figure 6-13 shows three main peaks and troughs indicating major changes within the compositions. Onset temperatures were obtained from the TA60 software. The first broad endotherm occurring between 125 – 133 °C indicates energy absorbed to release the water of hydration from the $CaSO_4 \cdot 2H_2O$. The next key change within the compositions took place between 660 – 687 °C. This smaller endotherm is due to the melting of aluminium fuel. Next is the thermal runaway indicative of the ignition of the composition. The instrument dynamics were unable to track the fast combustion. This is clearly seen by the fact that the DTA temperature signal loops back on itself. This means that the thermite reaction heated the chamber so fast that the temperature exceeded the programmed oven temperature. This forced the instrument to attempt cooling the oven to return to the programmed ramped temperature. These onset temperatures indicate an ignition temperature of between 907 – 985 °C at these test conditions.

Noteworthy is that the CSP5 composition did not ignite under these conditions. The implication is that the presence of the copper sulfate pentahydrate acted like an ignition inhibitor. It does not mean that it cannot ignite, but under DTA conditions it could not be ignited even with repeated attempts. Base1 and CSP5 compositions contain a smaller exotherm at 907 °C, which indicates that the aluminium and water may have started reacting.

6.3. Effect of glass spheres inclusion

6.3.1. Linear burn rates and maximum surface temperature of GSB and GS1 – GS5

A foreign, inert substance was introduced to lower the density of the thermite system. Sodium borosilicate glass spheres were included in the Base1 thermite to form low-density compositions labelled GSB and GS1 – GS5. The addition was expressed in add-on terms, i.e. the glass sphere content is expressed as a weight percent of the main composition. It ranged from 0 – 20 wt-% hollow glass spheres. GSB was the control containing 0 wt-% glass spheres while GS1 – GS5 contained between 5 – 20 wt-% glass spheres. Linear burn rates of casts of half-cylinder in shape with varying densities are shown in Figure 6-14.
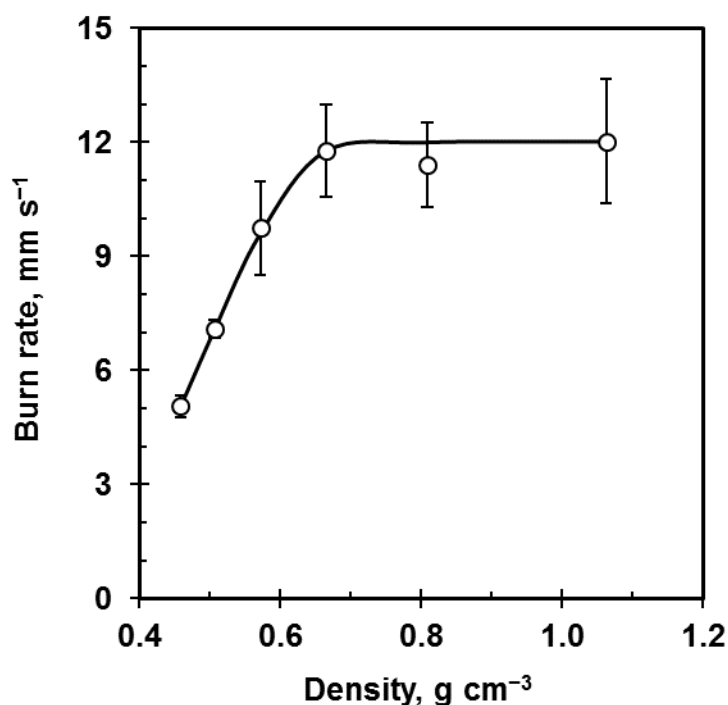
Figure 6-14: Linear burn rate of glass spheres casts with varying densities

Figure 6-14 shows the burn rate (mm s^{-1}) of the glass spheres casts corresponding to the density (g cm^{-3}) of the casts. The inclusion of low loadings of glass spheres, at higher densities, showed little to no effect on the burn rate. Considering the standard deviations of each composition, there seems to be a plateau trend in burn rate between 0 – 9 wt-% glass spheres (between densities of 2.50 – 1.50 g cm^{-3}). Thereafter, there is a rapid drop in burn rate with the inclusion of more glass spheres > 9 wt-% up to 20 wt-% (at densities between 1.50 – 1.00 g cm^{-3}). The glass spheres no longer occur sporadically within the composition. Now, they occur more frequently, creating physical barriers to diffusion. The presence of the inert glass spheres between 9 – 25 wt-% impedes the reaction.

The burn rate can be explained by considering the extreme cases describing kinetics- and diffusion-controlled reactions. Considering the kinetics-controlled case described in Equation 10,

$$u^2 = \frac{g(n)\,RT_c^2}{E_a\,(T_c - T_o)}\,(\alpha k_o)\,e^{-\frac{E_a}{RT_c}} \tag{10}$$

The terms describing reaction kinetics, including the function of reaction order $g(n)$, activation energy E_a and reaction rate constant k_o, are assumed to remain constant. This is since the reacting thermite content is maintained the same between compositions containing glass spheres. The glass spheres contribution to the kinetics of the thermite reaction should be minimal at low loadings where they only introduce sporadic cavities. Similarly, the initial and maximum reaction temperatures of the compositions (T_o and T_c) are expected to remain constant. Therefore, discounting the constant terms in Reaction 10 shows that the burn rate u (m s^{-1}) can be approximated to the square root of thermal diffusivity α (m^2 s^{-1}) shown in Equation 35

$$u \propto \sqrt{\alpha} \tag{35}$$

Expanding the thermal diffusivity term to include thermal conductivity λ (W m^{-1} K^{-1}), density ρ (kg m^{-3}) and specific heat capacity (J kg^{-1} K^{-1}) gives Equation 36

$$u \propto \sqrt{\lambda / (\rho\,C_p)} \tag{36}$$

Since the specific heat capacity remains constant on a mass basis, the burn rate can be approximated to

$$u \propto \sqrt{\lambda / \rho} \tag{37}$$

On the other hand, considering the diffusion-controlled case described in Equation 11,

$$u^2 = \frac{6\,RT_c^2}{E_D\,(T_c - T_o)} \left(\frac{\alpha D_o}{d^2}\right) e^{\frac{E_D}{RT_c}} \tag{11}$$

The pre-exponential factor for the diffusion coefficient E_D ($m^2\,s^{-1}$) and the apparent activation energy for the diffusion coefficient D_o ($J\,mol^{-1}$) are assumed to be constant for the composition. The particle size distribution of the reactants d (m) would remain relatively unchanged. The distance required for gaseous fuel/oxidiser particles to travel to a neighbouring oxidiser/fuel particle would remain the same since the cast material would be well-mixed and embedded in each other. Interestingly, both extreme cases of reaction-controlled and diffusion-controlled in Equation 10 and Equation 11 respectively gives the burn rate to be

$$u \propto \sqrt{\alpha} \tag{38}$$

It was observed that the burn rate decreased with a decrease in density. It must then be the case that the thermal conductivity of the system decreased at a faster rate than the density.

Figure 6-15 shows the progression of the glass spheres casts burning in the open air burn tests conducted in the laboratory.

(a) GSB

(b) GS1

(c) GS2

(d) GS3

(e) GS4

(f) GS5
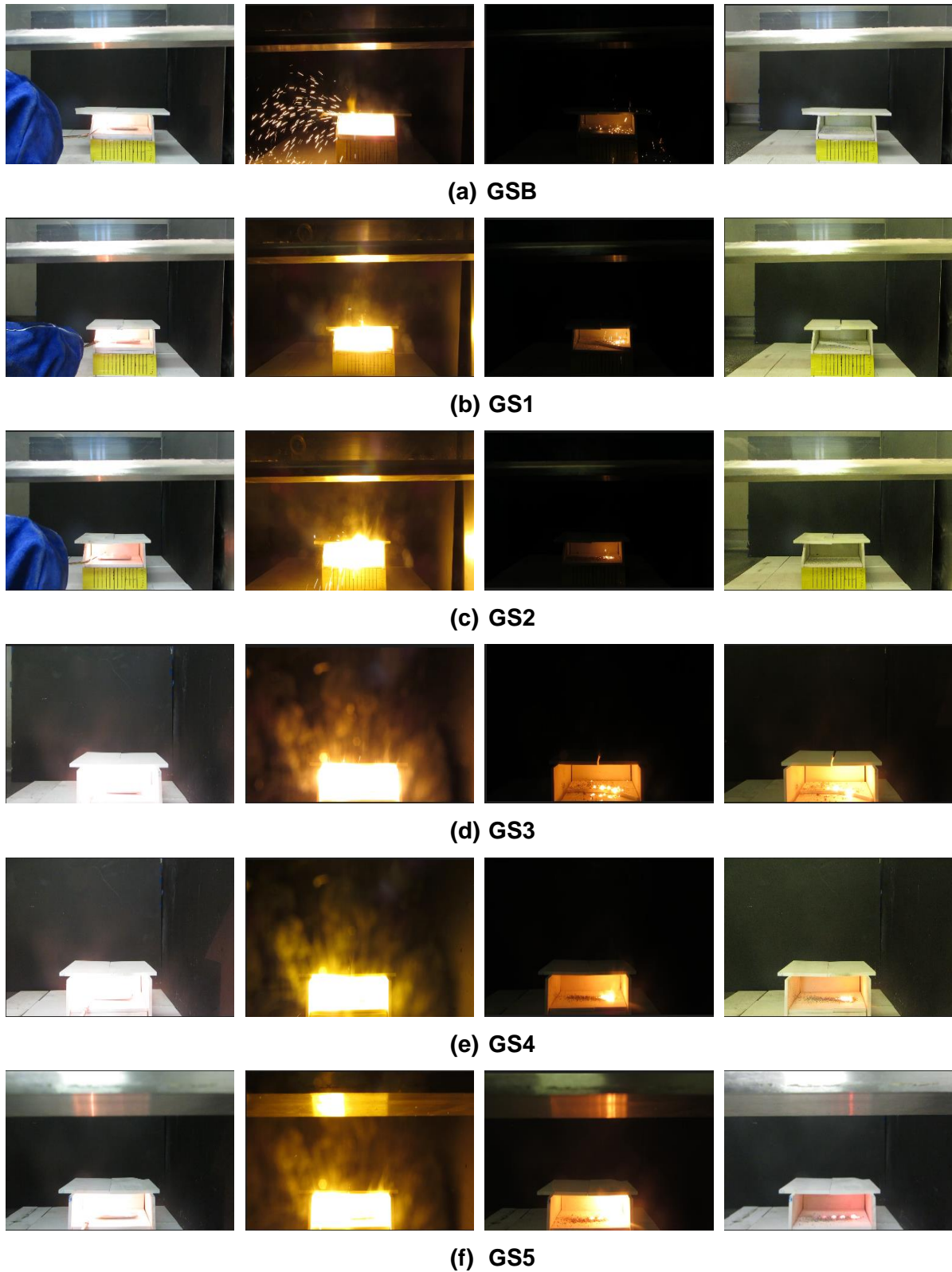
Figure 6-15: Progression of burn tests of glass pheres casts

It was found that, for all compositions, white regions and yellow regions of powder were seen. In addition, white spheres and slag were produced. Alumina tiles cracked at times during burn tests, indicating the reaction had exceeded 1000 °C. Figure 6-15 shows the presence of slag by the glowing products that remain at higher glass spheres loadings (GS3 – GS5).

The maximum surface temperature and temperature profile during burning of the glass spheres casts are shown in Figure 6-16.

(a)   **(b)**
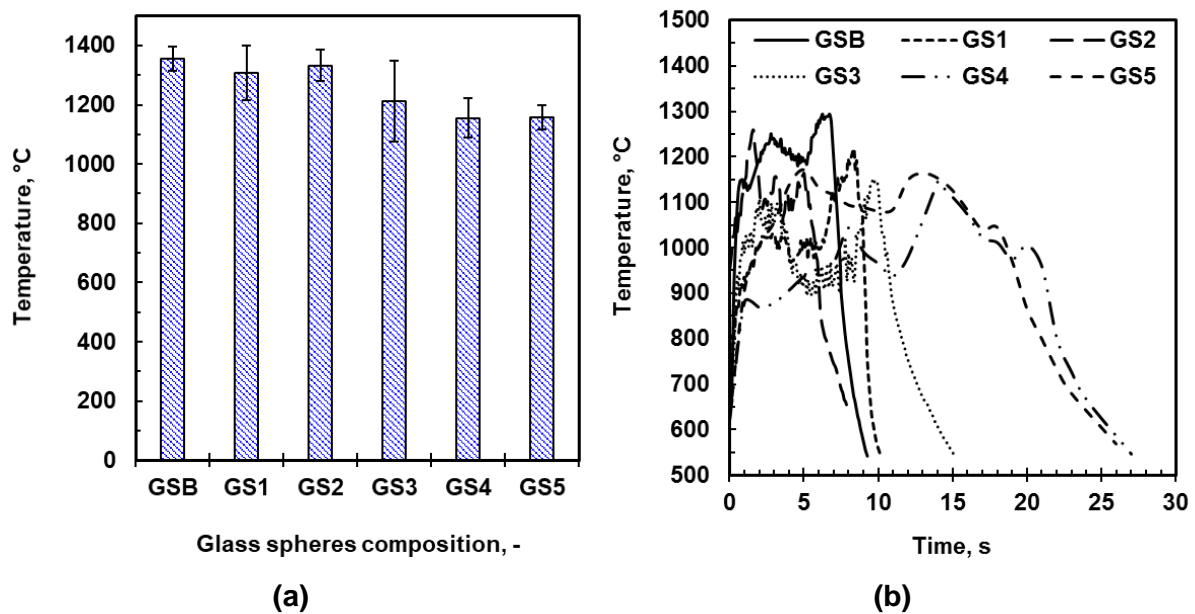
Figure 6-16: The (a) maximum surface temperature and (b) temperature profile of GSB and GS1 – GS5 casts

Figure 6-16a shows the largest surface temperature of 1356 ± 41 °C was achieved by the GSB composition, which contains 0 wt-% glass spheres. As the glass spheres loading increased, the maximum surface temperature decreased slightly. This could have been because the glass spheres created a barrier and solidified before the reacting material could burn. The temperature profiles of each composition during a burn is shown in Figure 6-16b, indicating the length and characteristics of the casts burning. The fastest (shortest) burning casts are GSB and GS1 while the slowest (longest) burning casts are GS4 and GS5. Furthermore, the gradual decreasing slopes observed at the end of the burns for GS4 and GS5 indicate that a slag was produced that stayed warm for longer than the other casts.

6.3.2. XRD phase analysis of burn residues of glass spheres casts

Table 6-9 shows the XRD phase analysis of the burn residues collected from alumina tiles.

Table 6-9: XRD phase analysis of burn residues collected from glass spheres casts

Burn product	GSB	GS1	GS2	GS3	GS4	GS5
Glass spheres (wt-%)	**0**	**5**	**9**	**13**	**17**	**20**
Al_2O_3	11	11	9	13	5	4
CaS	15	17		19	16	15
$CaO \cdot 6Al_2O_3$	24	17	12	63	53	57
$CaO \cdot 2Al_2O_3$	47	17	0	0	0	0
$CaSO_4$	0	0	0	1	1	0
Al	2	2	0	2	2	2
AlN	0	6	5	0	0	0
$Ca_8Na_2Si_{15}Al_9O_{54}$	0	0	31	0	0	0
$Na_2Al_{22}O_{34}$	0	0	4	0	0	1
$NaAl_{11}O_{17}$	0	31	0	0	21	17
Si	0	0	0	2	2	5
Total (wt-%)	**100**	**100**	**100**	**100**	**100**	**100**
Measured Al/Ca[*]	2.10	1.64	2.45	2.56	2.34	2.51
Expected Al/Ca[*]	2.86	2.86	2.86	2.86	2.86	2.86

[*]Mass ratio

Table 6-9 shows the major phase identified for GS1 was 31 wt-% sodium aluminate ($NaAl_{11}O_{17}$). The major phase identified for GS2, GS3, GS4 and GS5 was 40 wt-%, 63 wt-%, 53 wt-% and 57 wt-% monocalcium hexa-aluminate ($CaO \cdot 6Al_2O_3$) respectively. In comparison, the maximum condensed products predicted by EKVI simulations for GS1-GS5 (glass sphere loadings of 5 wt-%, 9 wt-%, 13wt-%, 17 wt-% and 20 wt-%) were 62 wt-% aluminium oxide (Al_2O_3), 55 wt-% Al_2O_3, 27 wt-% Al_2O_3 and 28 wt-% $CaO \cdot 2Al_2O_3$ respectively.

Again, the measured mass ratios of Al/Ca for each composition do not match those expected from theory. The presence of numerous phases makes the systems very complicated and difficult to analyse. Additionally, there is a discrepancy between the phases identified by XRD analysis and the products predicted in EKVI simulations. However, one should keep in mind that the XRD results reflect the composition of the burn residues at room temperature instead of at the adiabatic reaction temperature. In the actual burns, samples took a long time to cool down and additional reactions could have occurred in the process.

6.4. Effect of excess water

6.4.1. Linear burn rates and maximum surface temperature of excess water casts

Excess water was added when casting thermites to introduce porosity after the water had evaporated. Different calcium sulfate hemihydrate to water ratios were used to cast various thermites. Mole ratios between 1:10 and 1:14 were used, which corresponded to water contents of 40.9 – 49.2 wt-% for Base1 and 36.2 – 44.3 wt-% for S4 and CSP5. Mole ratios between 1:17 and 1:21 were used instead for Blend2, which corresponds to water content of 24.8 – 31.6 wt-%. Linear burn rates of the casts, approximately 5 g in mass and half-cylinder in shape, are shown in Figure 6-17.
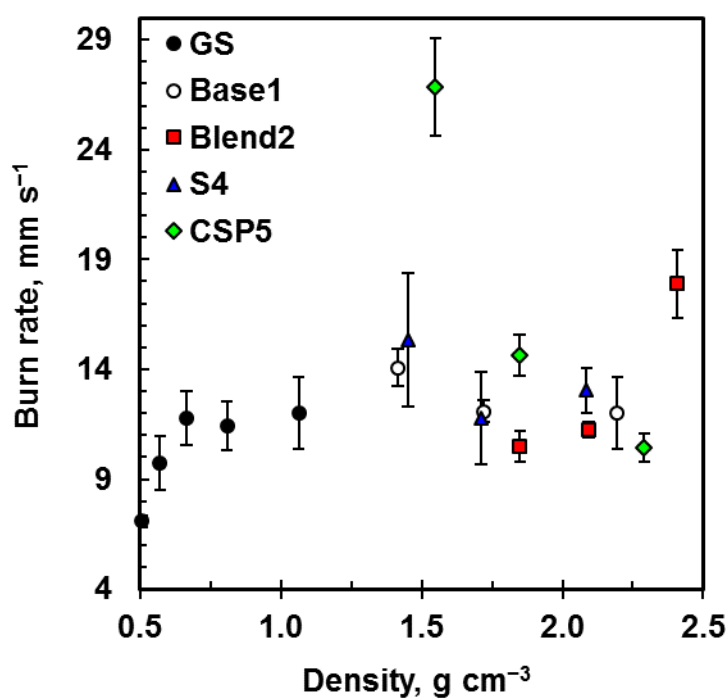
Figure 6-17: Linear burn rate (as a function of density) of excess water compositions compared with glass spheres compositions

Figure 6-17 shows that the excess water used in the Base1, Blend2, S4 and CSP5 compositions had, for the most part, little to no effect on the burn rates of the casts. The burn rates of excess water compositions did not differ greatly within densities of 1.50 – 2.50 g cm^{-3}, which follows the trend of GS casts at low loadings of glass spheres. For Base1, the addition of excess water resulted in a slightly faster burn rate of 14.1 ± 0.9 mm s^{-1} at its lowest density. However, there were outliers in the Blend2 composition and, to a much greater extent, the CSP5 composition. Blend2 had a slower burn rate of 10.5 ± 0.7 mm s^{-1} at its lowest density.

The burn rate of CSP5 compositions increased significantly to 26.8 ± 2.2 mm s^{-1} at lower densities, as the porosity was increased with excess water. This is contrasted with the opposite trend displayed by the GS casts at lower densities (higher loadings of glass spheres). The faster burn rates are attributed to the presence of pores created by the evaporation of the excess water. It is assumed that the pores assisted in the diffusion of gases created once the compositions are ignited. Generally, it was found that the presence of pores by excess water did not make much of a difference to the burn rate of these calcium sulfate-aluminium thermites.

Figure 6-18a shows the maximum surface temperature for the Base1, Blend2, S4 and CSP5 compositions at the three different water loadings. The optimum water ratios (listed in Table 6-2) were added to prepare Samples WR1. The process was repeated with excess quantities of water to form Samples WR2 and WR3. The water content in the slurries therefore ranged between 40.9 – 49.2 wt-% for Base1 and 36.2 – 44.3 wt-% for S4 and CSP5 compositions. For Blend2, the water content ranged between of 24.8 – 31.6 wt-% in the slurry. The temperature profiles of the compositions cast with the maximum excess water are shown in Figure 6-18b.
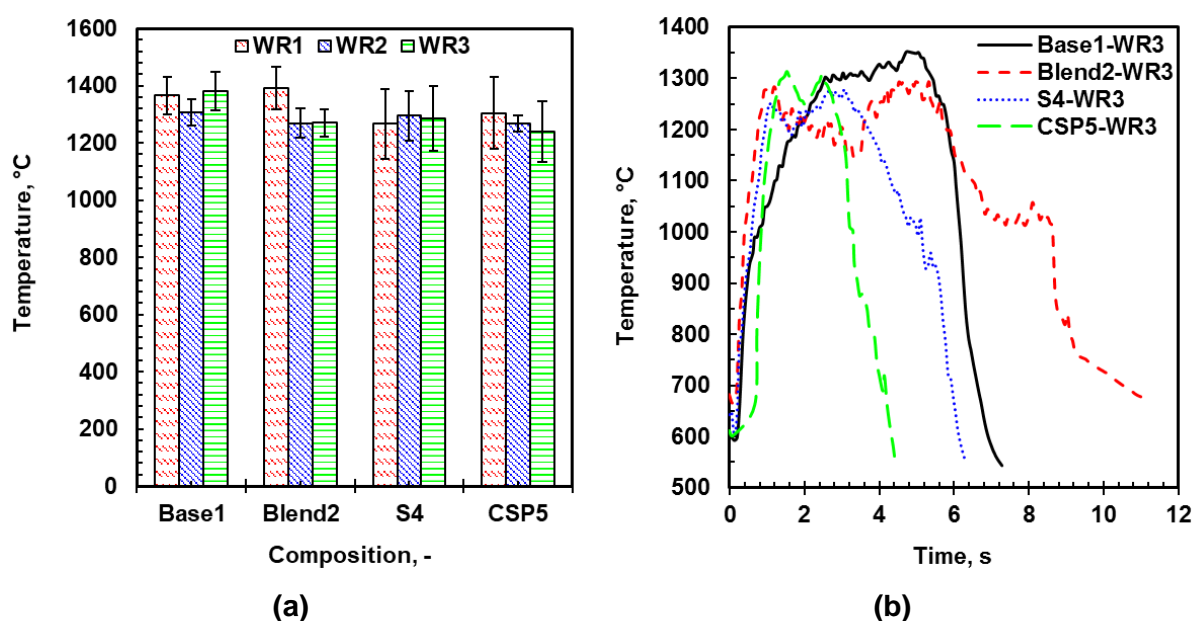
Figure 6-18: The (a) maximum surface temperature of samples WR1[a], WR2[b], WR3[c] and (b) temperature profile of maximum excess water casts

Note: [a]Optimum water ratios equivalent to 24.8 – 40.9 wt-% water in the slurries; [b]3.55 – 4.47 wt-% in excess of water in WR1; [c]6.79 – 8.31 wt-% in excess of water in WR1

Figure 6-18a shows that the surface temperature did not vary greatly between excess water samples. This was expected since the mass of reacting material was maintained constant. The excess water should have only evaporated, leaving pores behind. Figure 6-18b shows the varying temperature profiles recorded by the pyrometer for the excess water castings. The fastest burning composition, CSP5-WR3, can be seen.

6.5. Effect of heat treatment on casts in an oven

6.5.1. Compressive strength after casting and oven treatment

Base1, Blend2, S4 and CSP5 compositions were treated in an oven at 155°C (T2) and 200 °C (T3) for 2 h. The untreated compositions were labelled T1. The compressive strength (MPa) of the heat-treated casts is shown in Figure 6-19.
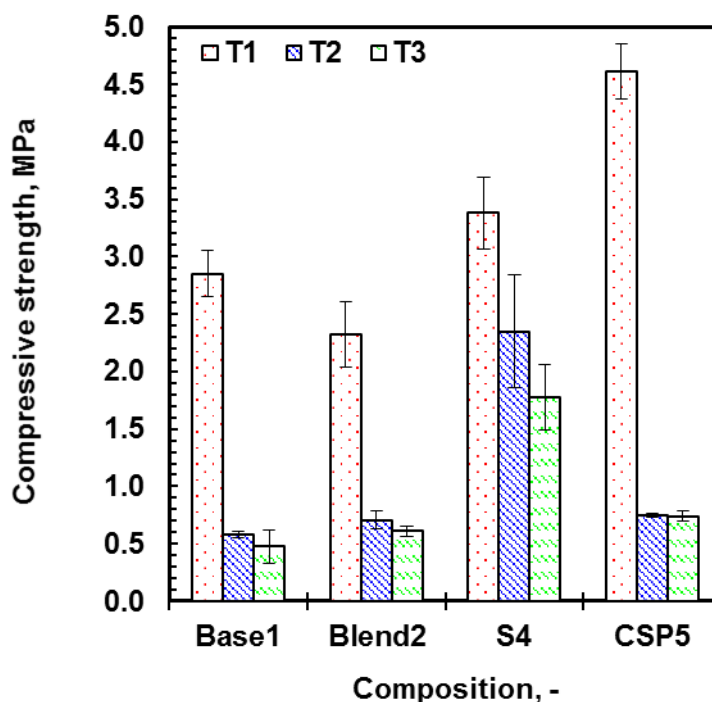
Figure 6-19: Compressive strength of casts after thermal treatment at 155°C (T2) and 200 °C (T3) compared with untreated casts (T1)

Figure 6-19 shows that oven treatment significantly reduced the compressive strength of all the compositions. It was interesting that the compressive strength of the S4 casts seemed to reduce less than the other compositions. At T3, the compressive strength of Base1, Blend2, S4 and CSP5 had reduced to 0.48 ± 0.15 MPa, 0.61 ± 0.04 MPa, 1.78 ± 0.28 MPa and 0.74 ± 0.05 MPa respectively.

6.5.2. Specific surface area

The BET surface areas of the oven-treated compositions are shown in Table 6-10. Blend2-T3 possessed the largest specific surface area of 2.50 m^2 g^{-1}.

Table 6-10: BET surface areas of heat-treated casts at 200 °C (T3)

Sample ID	Base1-T3	Blend2-T3	S4-T3	CSP5-T3
BET surface area (m^2 g^{-1})	1.72	2.50	1.46	1.61

6.5.3. Linear burn rates and maximum surface temperature of oven treated casts

Linear burn rates were recorded for the heat-treated compositions, shown in Figure 6-20.
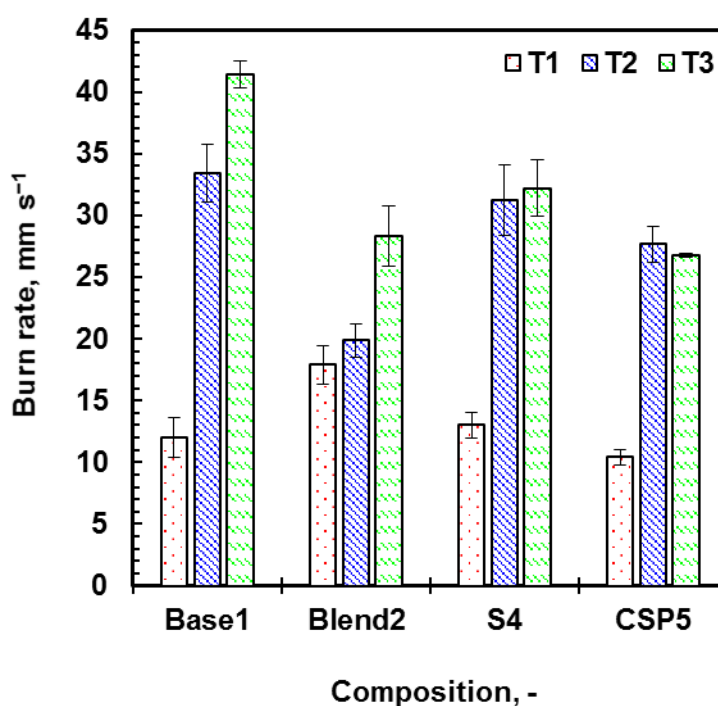
Figure 6-20: Linear burn rate of heat-treated casts at 155°C (T2) and 200 °C (T3) compared with untreated casts (T1)

Figure 6-20 shows that thermal treatment significantly increased the burn rates. The linear burn rate of Base1 increased almost threefold from 12.0 ± 1.6 mm s^{-1} (untreated) to 33.4 ± 2.3 mm s^{-1} (when treated at T2 = 155°C). Base1 produced the fastest burn rate of all the compositions of 41.4 ± 1.1 mm s^{-1} when treated at T3 = 200°C. Burn rates of 19.9 ± 1.4 mm s^{-1} and 28.3 ± 2.5 mm s^{-1} were observed for Blend2 after heat-treatment at T2 = 155°C and T3 = 200°C respectively. Blend2 casts seemed to burn very powerfully,

producing a flat metal-like product on the roof of the alumina tiles. Burn rates for S4-T2 and S4-T3 did not differ greatly, as they burned at a rate of 31.2 ± 2.9 mm s^{-1} and 32.2 ± 2.1 mm s^{-1} respectively. However, they did increase 2.4 and 2.5 times of the burn rate at S4-T1. On the other hand, CSP5-T2 and CSP5-T3 casts burned at a rate of 27.7 ± 1.5 mm s^{-1} and 26.7 ± 0.14 mm s^{-1}. These compositions increased 2.7 and 2.6 times from the burn rate at CSP5-T1 respectively.

The tests at T2 and T3 were to release to the water of hydration in $CaSO_4 \cdot 2H_2O$. Since Blend2 contained less $CaSO_4 \cdot 2H_2O$ than the other compositions, it was expected that its burn rate would be the least affected. It was found that the masses of Blend2 casts after oven treatment showed the least mass change when compared with the other compositions. In contrast for Base1, S4 and CSP5 they consisted predominantly of $CaSO_4 \cdot 2H_2O$. This was manipulated to become $CaSO_4$ resulting in their burn rates being significantly affected. It was observed that T2 and T3 casts burned very fast and this resulted in flat metallic product that formed on the roof of the alumina tiles. Additionally, it was observed that the oven-treated casts ignited more easily than T1 casts.

Figure 6-21a shows the maximum surface temperatures for the thermally treated casts. The temperature profiles of thermally treated casts are shown in Figure 6-21b.
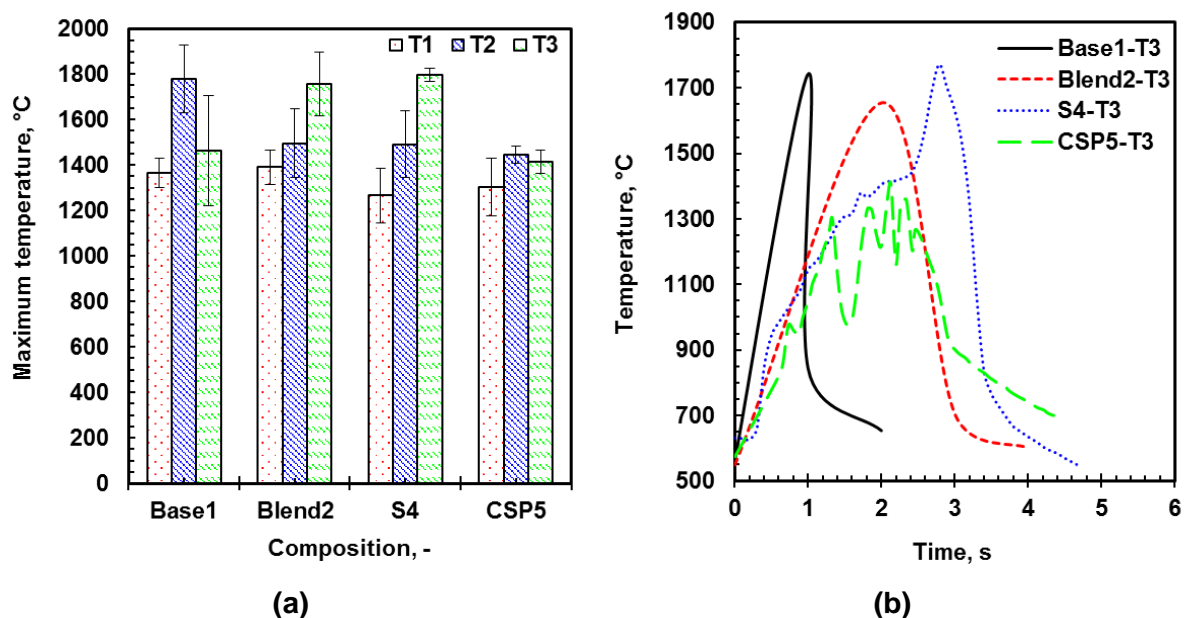
Figure 6-21: The (a) maximum surface temperature of heat-treated samples at 155°C (T2) and 200 °C (T3) compared with untreated casts (T1) and (b) temperature profiles of thermally treated casts at T3

Figure 6-21a shows that for Base1 and CSP5 compositions the highest surface temperature was achieved by casts treated at 155°C (T2). On the other hand, Blend2 and S4 showed that the highest surface temperature was achieved by casts treated at 200°C (T2). Maximum surface temperatures of 1781 ± 149 °C, 1756 ± 141 °C, 1796 ± 30 °C and 1446 ± 36 °C were observed for Base1-T2, Blend2-T3, S4-T3 and CSP5-T2 respectively. Figure 6-21b shows the temperature profile observed for casts thermally treated at 200 °C (T3).

6.5.4. XRD phase analysis of burn residues of oven tests casts

Table 6-11 shows the XRD phase analysis of the burn residues collected from alumina tiles.

Table 6-11: XRD phase analysis of burn residues collected from oven-treated casts

Burn product	Base1-T3[a]	Blend2-T3[a]	S4-T3[a]	CSP5-T3[a]
Al_2O_3	20	32	35	49
$CaO·6Al_2O_3$	27	15	0	0
$CaO·2Al_2O_3$	6	4	2	9
CaS	25	28	28	22
$CaSO_4$	0	0	0	1
Al	9	8	12	4
AlN	12	13	23	3
SiO_2	0	0	0	12
Total (wt-%)	**100**	**100**	**100**	**100**
Measured Al/Ca[b]	2.45	2.33	2.75	2.41
Expected Al/Ca[b]	2.86	2.53	2.58	3.44

[a]T3 = 200 °C; [b]Mass ratio

Table 6-11 shows the XRD phase analysis for the burn residues from the T3 oven tests. The most prominent condensed product for Base1 was 27 wt-% monocalcium hexa-aluminate ($CaO·6Al_2O_3$). In contrast, the largest condensed product for Blend2, S4 and CSP5 compositions were 32 wt-%, 35 wt-% and 49 wt-% aluminium oxide (Al_2O_3) respectively.

Measured Al/Ca ratios do not match the expected values shown in Table 6-11. It is assumed that the multiple phases present made quantitative analysis very challenging. The fact that XRD analysis was conducted on samples that had cooled down after burning means that reactions may have occurred. This may account for the discrepancy between the predicted products from EKVI simulations and the actual phases identified.

6.5.5. Energy output of compositions from bomb calorimeter

The energy output of the T3 compositions were determined from bomb calorimeter runs. The energy contribution of the starters and the nichrome wire initiator were taken into account to obtain an overall energy output shown in Figure 6-22.

Figure 6-22: Energy output of oven-treated Base1, Blend2, S4 and CSP5 thermites at T3 (200 °C)

Figure 6-22 shows that the energy output for the T3-treated casts do not differ greatly between compositions. The largest heat release was 6.92 ± 0.17 MJ kg^{-1} for Blend2. This was closely followed by 6.81 ± 0.19 MJ kg^{-1} for Base1. Composition CSP5 resulted in a heat release of 6.51 ± 0.01 MJ kg^{-1}. Composition S4 produced the lowest heat release of 6.45 ± 0.10 MJ kg^{-1}.

6.6. Effect of urea additive to base case compositions

6.6.1. Compressive strength after casting with urea additive

Cylindrical casts containing U0 – U3 loadings of 0 wt-%, 1 wt-%, 2 wt-% and 9 wt-% urea were tested for compressive strength, as shown in Figure 6-23.
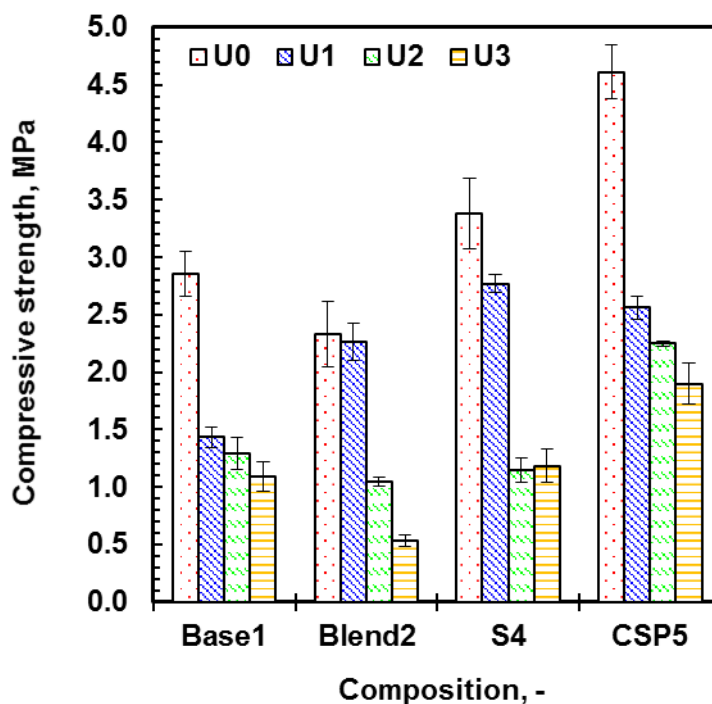
Figure 6-23: Compressive strength of cast thermites containing 0 wt-%, 1 wt-%, 2 wt-% and 9 wt-% urea labelled U0 – U3

Figure 6-23 displays the same trend for all urea-containing compositions. The inclusion of urea, and an increase in urea loading, resulted in a reduction in compressive strength. At a urea loading of 9 wt-% (U3), the compressive strength of Base1, Blend2, S4 and CSP5 had reduced to 1.09 ± 0.13 MPa, 0.53 ± 0.05 MPa, 1.18 ± 0.14 MPa and 1.90 ± 0.18 MPa respectively.

6.6.2. Linear burn rates and maximum surface temperature of urea casts

Linear burn rates were recorded for each composition at urea loadings U0 – U3, corresponding to 0 wt-%, 1 wt-%, 2 wt-% and 9 wt-% urea respectively, as shown in Figure 6-24.
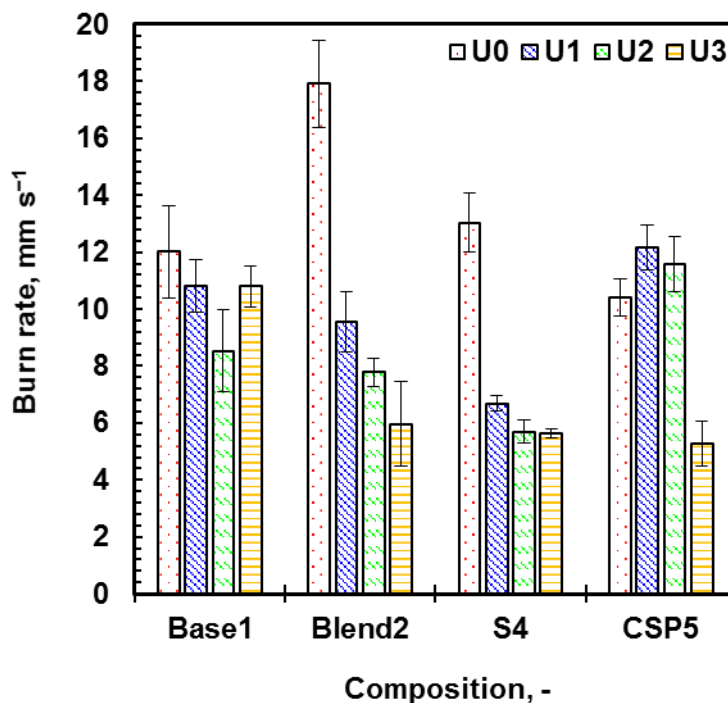
Figure 6-24: Linear burn rate of urea-containing thermites

Figure 6-24 shows that an increase in urea loading for Blend2 and S4 resulted in a slower burn rate. For Base1, burn rates for casts containing urea were all less than Base1-U0. However, no trend was observed. Similarly, no trend was observed for CSP5 casts. The inclusion of 1 wt-% urea (U1) to CSP5 resulted in an increase in burn rate. On the other hand, 2 wt-% and 9 wt-% urea loadings in CSP5-U2 and CSP5-U3 showed a decrease in burn rate.

It was noted during the burns that the compositions with higher urea loadings burned for longer and also produced a slag. This slag remained very hot for a longer period of time after the burn had completed, which may be beneficial for cutting.

Figure 6-25a shows the maximum surface temperatures for the compositions with different urea loadings. The temperature profile of the casts containing 9 wt-% (U3) urea is shown in Figure 6-21b.
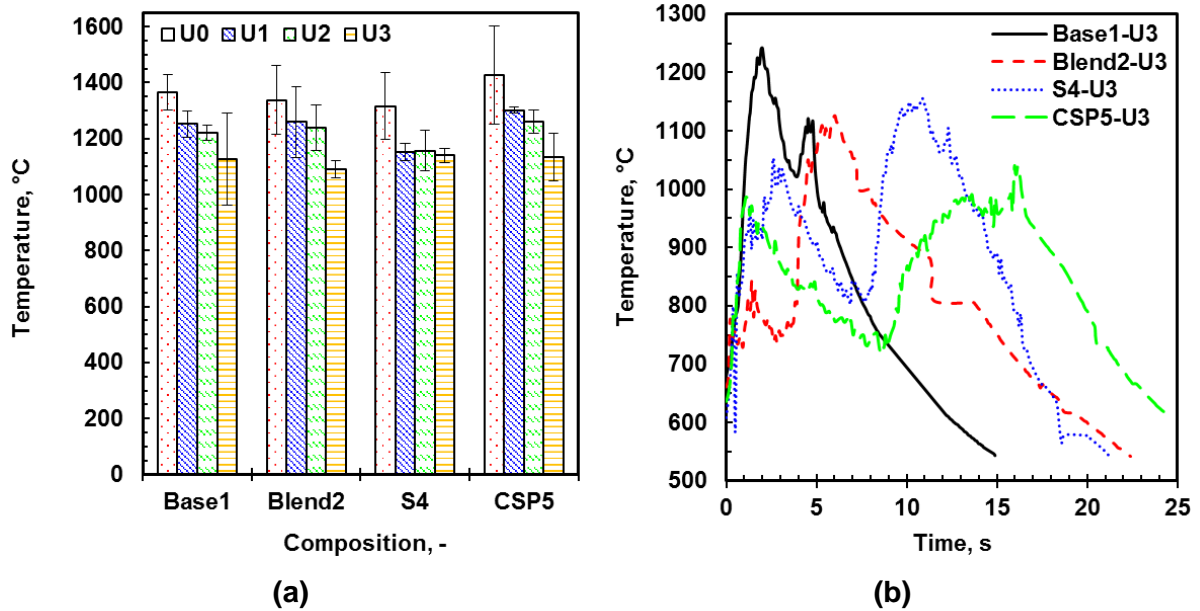
Figure 6-25: The (a) maximum surface temperature of compositions with 0 wt-%, 1 wt-%, 3 wt-% and 9 wt-% urea labelled U0 – U3 and (b) temperature profile of thermites with 9 wt-% urea (U3)

Figure 6-25a shows that the inclusion of 1 wt-% urea to the base case compositions resulted in a decrease in surface temperature for all compositions. Furthermore, an increase in urea loading resulted in even lower surface temperatures being reached. Interestingly, however, the surface temperatures of compositions labelled S4-U1, S4-U2 and S4-U3 remained relatively constant with the urea loading changes.

Figure 6-25b shows the temperature of the reaction observed over time for the compositions loaded with 9 wt-% (U3) urea. It was observed that a hard cohesive slag was produced in the urea compositions, which had remained hot after the composition had finished burning. The presence of slag is evident in Figure 6-25b by the gradual decreasing slope towards the end of the burn for all compositions.

6.6.3. XRD phase analysis of burn residues of urea casts

Table 6-12 shows the XRD phase analysis of the burn residues collected from alumina tiles.

Table 6-12: XRD phase analysis of burn residues collected from urea-containing casts

Burn product	Base1-U3[a]	Blend2-U3[a]	S4-U3[a]	CSP5-U3[a]
Al_2O_3	14	0	58	25
CaS	19	22	15	19
$CaO \cdot 6Al_2O_3$	29	18	0	27
$CaO \cdot 2Al_2O_3$	29	21	0	26
$CaSO_4$	2	2	0	1
AlN	3	4r	0	0
Al	1	0	0	0
N_2H_6O	1	0	11	0
SiO_2	0	5	0	3
Total (wt-%)	**100**	**100**	**100**	**100**
Measured Al/Ca[b]	1.93	1.08	3.48	1.36
Expected Al/Ca[b]	2.86	2.53	2.58	3.44

[a]U3 = 9 wt-% urea; [b]Mass ratio

Table 6-12 shows that the most prominent products for Base1-U3 were calcium aluminates including 29 wt-% $CaO \cdot 6Al_2O_3$ and 29 wt-% $CaO \cdot 2Al_2O_3$. Similarly, the most prominent species for CSP5-U3 were 27 wt-% $CaO \cdot 6Al_2O_3$ and 26 wt-% $CaO \cdot 2Al_2O_3$. For Blend2-U3, the largest condensed product was 22 wt-% CaS. In contrast, the largest solid product for the S4-U3 composition was 58 wt-% Al_2O_3.

FactSage simulations showed that the major products predicted for all composition at a U3 (9 wt-% urea) loading were aluminium oxide (Al_2O_3 (l)) and calcium sulfide (CaS (s)). Base1-U3 and Blend2-U3 were simulated to produce 64 wt-% and 57 wt-% Al_2O_3 (l) with 9 wt-% and 23 wt-% CaS (s) respectively. For S4-U3 and CSP5-U3, the major products were 50 wt-% and 64 wt-% Al_2O_3 (l)) with 18 wt-% and 17 wt-% CaS (s) respectively.

Measured Al/Ca ratios do not match the expected values shown in Table 6-12. Again, it is assumed that the multiple phases present made it difficult to quantitatively analyse the phases. Also, XRD analysis was conducted on samples that had cooled down after burning, where other reactions may have occurred. In contrast, FactSage simulations were at the adiabatic flame temperature.

6.6.4. Energy output of compositions from bomb calorimeter

The energy output of the U3 compositions were determined from bomb calorimeter runs. The energy contribution of the starters and the nichrome wire initiator were taken into account to obtain an overall energy output shown in Figure 6-26.
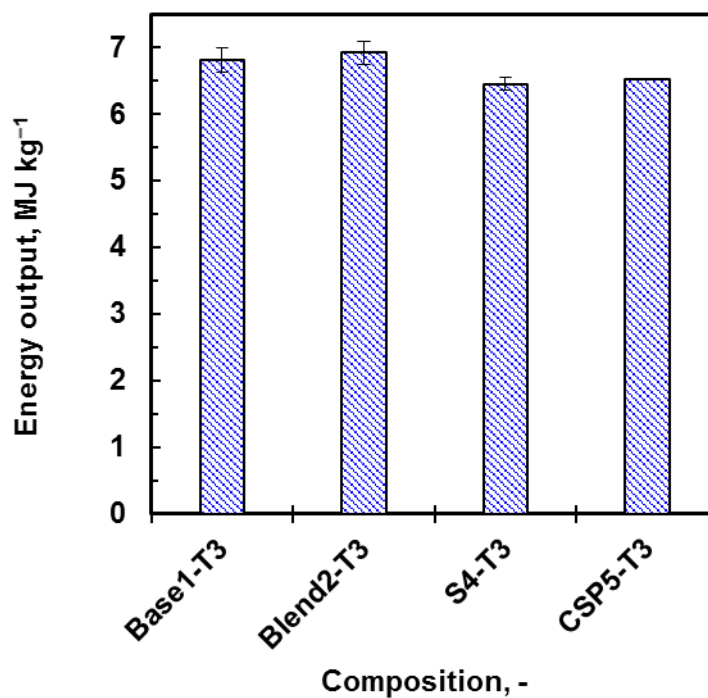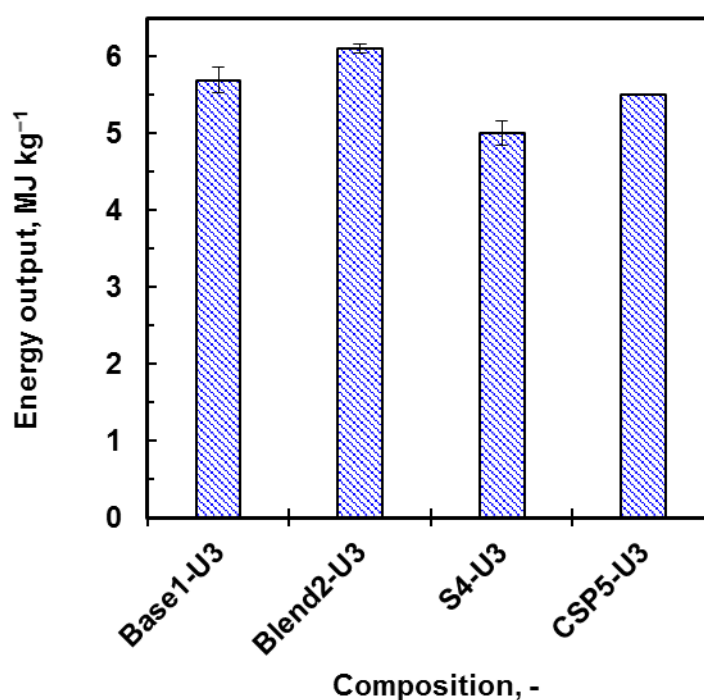

Figure 6-26: Energy output of Base1, Blend2, S4 and CSP5 casts with U3 (9 wt-% urea) loading

Figure 6-26 shows that the largest heat release was 6.10 ± 0.05 MJ kg^{-1} for Blend2. This was closely followed by 5.70 ± 0.16 MJ kg^{-1} for Base1. Composition CSP5 resulted in a heat release of 5.51 ± 0.00 MJ kg^{-1}. Composition S4 produced the lowest heat release of 5.00 ± 0.16 MJ kg^{-1}.

6.7. Summary of key laboratory results

A summary of the defining characteristics for the compositions of most interest for base case compositions, oven-treated casts at 200 °C (T3) and casts with 9wt-% urea (U3) is given in Table 6-13.

Table 6-13: Summary of key results for base, oven-treated and urea compositions

Burn product	Compressive strength (MPa)	Maximum temperature (°C)	Linear burn rate (mm s^{-1})	Energy output (MJ kg^{-1})
Base1	2.85 ± 0.20	1365 ± 64	12.0 ± 1.6	7.96 ±1.07
Base1-T3[a]	0.48 ± 0.15	1463 ± 243	41.4 ± 1.1	6.81 ± 0.19
Base1-U3[b]	1.09 ± 0.13	1126 ± 164	10.8 ± 0.7	5.70 ±0.16
Blend2	2.33 ± 0.28	1392 ± 76	17.9 ± 1.6	7.21 ± 0.34
Blend2-T3[a]	0.61 ± 0.04	1756 ± 141	28.3 ± 2.5	6.92 ±0.17
Blend2-U3[b]	0.53 ± 0.05	1091 ± 31	5.96 ± 1.47	6.10 ±0.06
S4	3.38 ± 0.31	1266 ± 121	13.0 ± 1.0	5.90 ± 0.48
S4-T3[a]	1.78 ± 0.28	1796 ± 30	32.2 ± 2.3	6.45 ± 0.10
S4-U3[b]	1.18 ± 0.14	1141 ± 25	5.62 ± 0.15	5.00 ±0.16
CSP5	4.61 ± 0.24	1304 ± 126	10.4 ± 0.6	7.78 ± 0.58
CSP5-T3[a]	0.74 ± 0.05	1414 ± 50	26.7 ± 0.1	6.51 ±0.01
CSP5-U3[b]	1.90 ± 0.18	1134 ± 86	5.28 ± 0.80	5.51 ±0.00

[a]Heat-treated at 200 °C; [b]Containing 9-wt-% urea

6.8. Suitability of thermites for metal-cutting

It was of interest to determine whether Base1, Blend2, S4 and CSP5 compositions would be suitable for metal-cutting. Additionally, these casts were treated at 155 °C (T2). This temperature was chosen since the phenolic tubes begin decomposing, and release a bad odour, at temperatures > 200 °C. Casts were also prepared with 9 wt-% urea (U3) to investigate if the hot slag observed in open burn tests would be beneficial to metal-cutting. Observations and linear burn rates from the metal-cutting tests are given in Table 6-14.

Table 6-14: Observations during metal-cutting burn tests

Sample ID	Observations	Burn rate (mm s^{-1})
Base1	Did not puncture aluminium block, only produced a slag. The aluminium block was very hot after test.	9.9
Blend2	Did not puncture aluminium block, only produced a slag. The aluminium block was very hot after test.	7.4
S4	Did not puncture aluminium block, only produced a slag. The aluminium block was very hot after test.	8.8
CSP5	Seemed to burn well. Did not puncture aluminium block, only produced a slag. The aluminium block was very hot after test.	9.1
Base1-T2[a]	Burned very fast. Made a dent in the aluminium block.	819
Blend2-T2[a]	Burned very fast. Made a dent in the aluminium block.	781
S4-T2[a]	Burned the fastest, sounded like it exploded. Very loud. Made a dent in the aluminium block.	1016
CSP5-T2[a]	Burned the slowest of the oven-treated compositions. Made a dent in the aluminium block.	18

[a]Heat-treated at 200 °C

The compositions containing urea did not ignite, even with excess starter being used. Table 6-14 shows that Base1, Blend2, S4 and CSP5 compositions produced only a slag, which did not assist in melting the aluminium blocks. They did, however, result in the block becoming very hot after burning, which took longer to cool down after tests. Oven-treated compositions Base1-T2, Blend2-T2, S4-T2 and CSP5-T2 thermites, shown in Table 6-14, were the only compositions that melted through a part of the aluminium block. These blocks did not retain as much heat as the blocks that were tested with the predominantly slag-producing compositions. It was observed that the blocks were not hot to touch soon after tests had been

completed. The mass of the aluminium blocks after testing were all greater than the initial mass recorded. This is attributed to the slag that was produced by the burning compositions. Additionally, any aluminium that was melted may have re-solidified in place and was not sprayed off the block by the jet of burning thermite.

Burn rates were calculated from the sound files associated with the videos taken. Table 6-14 shows that the S4-T2 composition burned significantly faster than the other compositions at 1016 mm s^{-1}. This was explained by the fact this composition was more porous than the other compositions after oven treatment, since both water of hydration and sulfur were being drawn off from the cast. This burn rate was followed by Base1-T2 at 819 mm s^{-1} and Blend2-T2 at 781 mm s^{-1}. Of the thermally treated compositions that had been burned in open air burn tests, the fastest burning composition was Base1-T2. This was followed by S4-T2 and then CSP5-T2. The slowest burning composition in open air burn tests was Blend2-T2.

The punctured aluminium blocks are shown in Figure 6-27.

Figure 6-27: Punctured aluminium blocks after confined burn tests

It is difficult to see the depth of the dents made in the blocks shown in Figure 6-27. The powder burn residues were washed off and the cleaned aluminium blocks are shown in Figure 6-28. An average diameter was measured and the maximum depth was recorded.

(a1) Base1-T2

Diameter

= 16.7 mm

Max depth

= 4.2 mm

(a2) Base1-T2

Diameter

= 10.3 mm

Max depth

= 4.2 mm

(b1) Blend2-T2

Diameter

= 13.7 mm

Max depth

= 6.9 mm

(b2) Blend2-T2

Diameter

= 13.5 mm

Max depth

= 7.1 mm

(c1) S4-T2

Seemed to explode, aluminium block forced out of place.

(c2) S4-T2

Diameter

= 14.0 mm

Max depth

= 3.0 mm

(d1) CSP5-T2

Only produced slag.

(d2) CSP5-T2

Diameter

= 3.4 mm

Max depth

= 2.3 mm
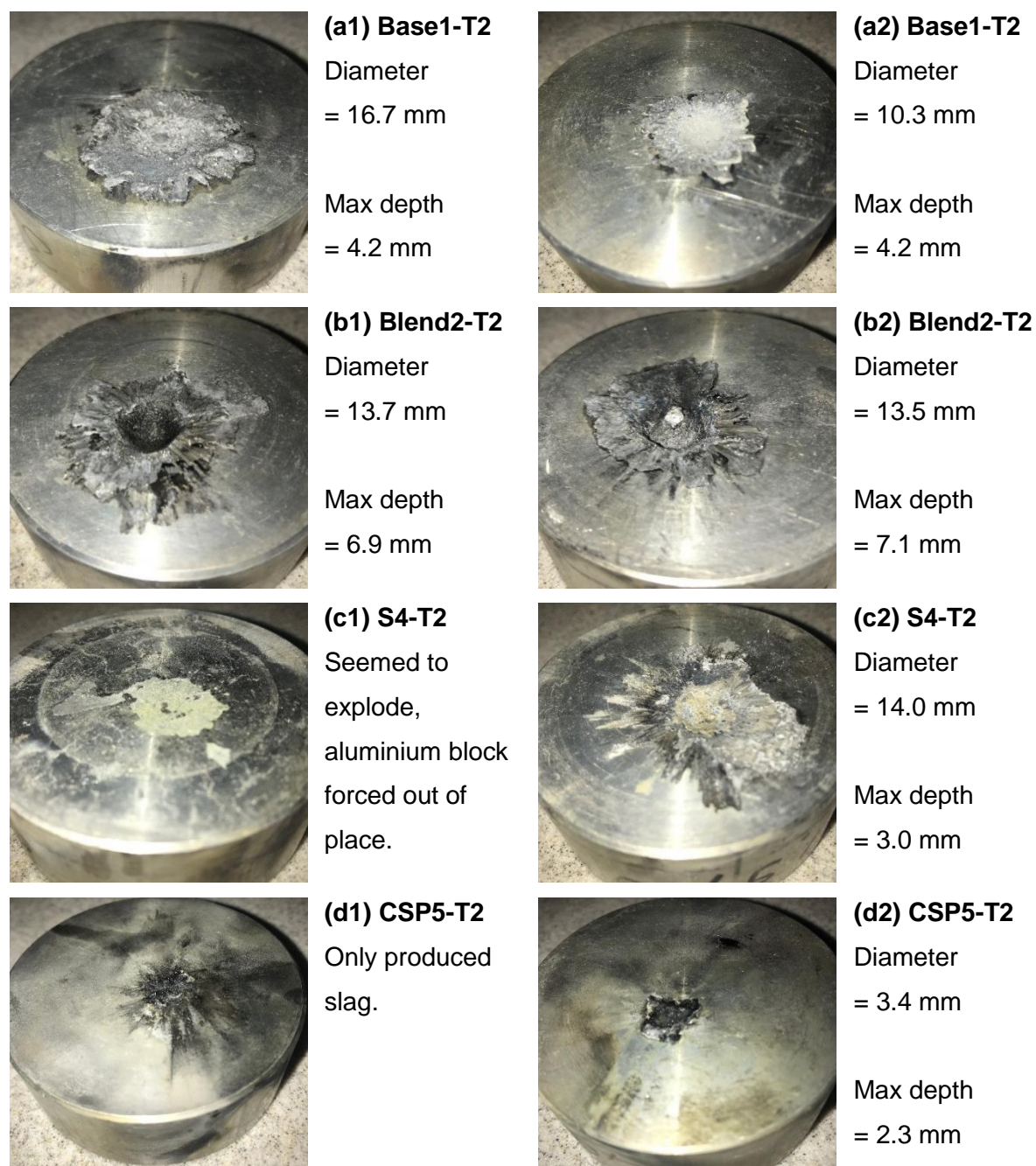
Figure 6-28: Size and depth of puncture resulting from (a) Base1-T2, (b) Blend2-T2, (c) S4-T2 and (d) CSP5-T2 compositions pre-treated at 155 °C (T2)

Figure 6-28b shows that the largest puncture was created by the Blend2-T2 composition. A hole with an average diameter of 13.7 mm and 13.5 mm and depths of 6.9 mm and 7.1 mm were formed for Blend2-T2 compositions. The first aluminium blocks were not punctured by S4-T2 and CSP5-T2 compositions. Interestingly, S4-T2 seemed to explode while CSP5-T2 burned significantly slower and only produced a slag. Both of the second burns, however, punctured into the blocks. A larger diameter hole was produced by S4-T2 in Figure 6-28(c2)

than for CSP5-T2 in Figure 6-28(d2). Despite the thermites being high energy-releasing and portraying high surface temperatures, they were not very effective or suitable for metal-cutting.

The thrust produced by the compositions was not large enough to be detected by the force transducer during burning. However, the initial force of the starter being initiated and the sample igniting at t = 0 s was detected. The sample producing the greatest initial thrust was S4-T2. This corresponded with observations made during the confined burn tests, as it sounded like they exploded. They burned extremely fast and produced a loud noise. The Blend2-T2 composition produced the next largest force upon ignition. CSP5-T2 produced the smallest initial thrust, which corresponded with observations. It seemed to burn the slowest. Flames and gases were observed CSP5-T2 burning.

Chapter 7: Conclusions and recommendations

7.1. Evaluation of the base case

The energetics of the thermite castings comprising calcium sulfate dihydrate (oxidant) with aluminium (fuel) was studied. The optimum composition, in this investigation, was associated with the one that produced the maximum adiabatic surface temperature predicted in EKVI simulations. This was approximately 2800 °C for the base case "Base1" with 60 wt-% $CaSO_4 \cdot 2H_2O$ and 40 wt-% Al.

This system exploits the ability of the calcium sulfate hemihydrate to set when mixed with water. So, in actual fact the starting powder mixture comprised 55.8 wt-% $CaSO_4 \cdot 0.5H_2O$ and 44.2 wt-% Al. It was possible to prepare strong castings using water slurries with solids contents ranging from 51 – 59 wt-%. This water is in excess of that needed to form the dihydrate. The excess water was necessary for effective mixing and for the required flowability to ensure that setting resulted in consistent castings with a smooth surface. The measured heat of hydration, for the reaction between $CaSO_4 \cdot 0.5H_2O$ and H_2O to produce $CaSO_4 \cdot 2H_2O$, for the Base1 formulation was 59 ± 7.9 J g^{-1}. This occurred at a maximum hydration after 53 ± 0.17 min. Casts were allowed to age and dry for at least 3 days at ambient conditions before being used in tests. The compressive strength of Base1 casts was 2.85 ± 0.20 MPa. In open air burn tests, the linear burn rate was 12.0 ± 1.6 mm s^{-1} and a maximum measured surface temperature was 1365 ± 64 °C. Bomb calorimetry studies showed that the Base1 thermite released an energy output of 7.96 ± 1.07 MJ kg^{-1}.

7.2. Burn rates and performance of thermite compositions with additives

Additives, including anhydrous calcium sulfate ($CaSO_4$), sulfur (S) and copper sulfate pentahydrate ($CuSO_4 \cdot 5H_2O$), were added to the base case. The addition of 30 wt-% $CaSO_4$ to 30 wt-% $CaSO_4 \cdot 2H_2O$ and 40 wt-% Al in the Blend2 composition resulted in a linear burn rate of 17.9 ± 1.6 mm s^{-1}. This was the fastest burning composition amongst the base case and compositions with additives. The energy output of the reaction was 7.21 ± 0.34 MJ kg^{-1} while the compressive strength for Blend2 was the lowest of the compositions at 2.33 ± 0.28 MPa.

Composition CSP5, containing 10 wt-% $CuSO_4 \cdot 5H_2O$, 50 wt-% $CaSO_4 \cdot 2H_2O$ and 40 wt-% Al, produced the slowest burn rate of 10.4 ± 0.64 mm s^{-1}. Despite the slow burn rate, it should be noted that CSP5 seemed to produce a cohesive slag residue which implies that the

combustion products were at least partially molten. The residue also remained hot for quite some time after the combustion event was complete. This may be beneficial for a cutting device. Bomb calorimetry runs of CSP5 showed that it produced the next highest energy output after Base1, i.e. 7.78 ± 0.58 MJ kg^{-1}. The CuSO$_4$·5H$_2$O-based composition set significantly faster than the others. It also produced the strongest casts with the highest compressive strength of 4.61 ± 0.24 MPa.

Oven heat treatments were done at 155 °C and 200 °C. These were selected to remove the water of hydration from the CaSO$_4$·2H$_2$O phase in order to form the hemihydrate and anhydrite forms respectively. In all cases the heat treatment resulted in significant increases in burn rates. The most significant change was to Base1, where the linear burn rate increased almost threefold from 12 ± 1.6 mm s^{-1} to 33 ± 2.3 mm s^{-1} and 41 ± 1.1 mm s^{-1} when heat treated at 155 °C and 200 °C respectively. However, at the same time, the compressive strength decreased significantly to 0.58 ± 0.02 MPa and 0.48 ± 0.15 MPa respectively.

Up to 9 wt-% urea (CO(NH)$_2$) was included, dissolved in the casting water, in the base case composition and in compositions with the other additives. The burn rates were universally lowered in the presence of urea. For example, Base1 with 9 wt-% urea burned at a linear rate of 10.8 ± 0.7 mm s^{-1}.

7.3. Effect of density on burn rate

The effect of density on burn rate was investigated by the inclusion of low-density sodium-borosilicate glass spheres. The burn rate was hardly affected down to densities of ca. 1.50 g cm^{-3} but then dipped to significantly lower values. It is speculated that the decrease in burn rate can be attributed to a reduction in the thermal conductivity and/or the glass phase constituting a diffusion barrier at higher loadings of the hollow glass spheres.

Density reduction was also induced by adding excess water, i.e. preparing casts using slurries with a lower solids content. The burn rates of excess water compositions did not differ greatly within densities of 1.50 – 2.50 g cm^{-3}, which followed the trend of glass sphere casts at low loadings of glass spheres. However, the burn rate of CSP5 compositions increased significantly to 26.8 ± 2.2 mm s^{-1} at lower densities, as the porosity was increased with excess water. This is contrasted with the opposite trend displayed by the GS casts at lower densities and higher loadings of glass spheres. It is assumed that the pores assisted in the diffusion of gases created once the compositions were ignited.

For the glass sphere casts, the maximum surface temperatures remained relatively constant but decreased slightly at higher loadings. For the excess water casts, the maximum surface temperatures also remained constant. This was expected since the chemical composition had not been altered in any way.

7.4. Suitability for metal-cutting

The base case composition, as well as those with additives including Base1, Blend2, S4 and CSP5, were not successful in puncturing the aluminium blocks. However, it was observed that they transferred a significant amount of heat to the blocks by the production of slag. The blocks retained this heat for some time after burning. It was found that heat-treated Base1, Blend2, S4 and CSP5 compositions at 155 °C (T2) were capable of puncturing portions of an aluminium block. The mass of melted aluminium could not be quantified since a very hard cohesive slag was formed and contributed to a mass increase. The Blend2-T2 compositions punctured holes of diameters 13.7 mm and 13.5 mm with depths of 6.9 mm and 7.1 mm respectively. The calcium sulfate dihydrate-aluminium thermites on their own were not suitable for metal-cutting. They did not produce sufficient liquid-phase products to assist with ejecting the hot thermite out of the nozzle of the phenolic tube.

7.5. Recommendations for further testing

The calcium sulfate dihydrate-aluminium thermites studied in this investigation were found to be highly energetic and had high adiabatic reaction temperatures. These properties could be a beneficial additive to a metal-cutting thermite as a binder, as it would add energy to a system. In particular, the copper sulfate pentahydrate-containing composition would be best-suited for application in-situ in field, since it sets significantly faster than the other compositions. It would thus be convenient for mixing thermites as required. Further studies should be conducted on the water content that would be required when the binder is combined with other thermite systems. The metal-cutting thermites would require excess aluminium or fuel, since the calcium sulfate dihydrate-based compositions have been found to react with aluminium.

References

Aldushin, A. P. & Khaikin, B. I. 1974. Combustion of mixtures forming condensed reaction products. *Combustion, Explosion and Shock Waves (English Translation),* 10**,** 313-323.

Particle Analytical. 2016a. *BET* [Online]. Available: http://particle.dk/methods-analytical-laboratory/surface-area-bet-2/ [Accessed 12 October 2016].

Particle Analytical. 2016b. *X-Ray Diffraction - XRD* [Online]. Available: http://particle.dk/methods-analytical-laboratory/xrd-analysis/ [Accessed 1 August 2016].

ASTM 2017. Standard Test Method for Compressive Strength of Cylindrical Concrete Specimens. United States: ASTM International.

Bale, C. W. & Pelton, A. D. 2015. FactSage. 7.0 ed.

Berger, B. 2005. Parameters Influencing the Pyrotechnic Reaction. *Propellants, Explosives, Pyrotechnics,* 30**,** 27-35.

Bhadeshia, H. K. D. H. 2002. *Thermal Analysis Techniques* [Online]. Available: https://www.phase-trans.msm.cam.ac.uk/2002/Thermal1.pdf [Accessed November 2017].

Blake, G. R. 2008. Particle Density. *In:* CHESWORTH, W. (ed.) *Encyclopedia of Soil Science* 1ed. The Netherlands: Springer.

Callister, W. D. & Rethwisch, D. G. 2010. *Materials Science and Engineering: An Introduction* John Wiley & Sons, Inc.

Coates, J. 2000. Interpretation of Infrared Spectra, A Practical Approach. *In:* MEYERS, R. A. (ed.) *Encyclopedia of Analytical Chemistry.* Chichester: John Wiley & Sons Ltd.

Comet, M., Vidick, G., Schnell, F., Suma, Y., Baps, B. & Spitzer, D. 2015. Sulfates-Based Nanothermites: An Expanding Horizon for Metastable Interstitial Composites. *Angewandte Chemie International Edition* 4458-4462.

AMT Composites. 2017. *Glass bubbles* [Online]. Available: http://www.amtcomposites.co.za/products/resin-fillers-pigments/fillers/glass-bubbles [Accessed March 2017].

Conkling, J. A. 1985. Pyrotechnics. *Kirk-Othmer Encyclopedia of Chemical Technology.* John Wiley & Sons, Inc.

de Korte, A. C. J. 2015. *Hydration and thermal decomposition of cement/calcium sulphate based materials.* Doctor of Philosophy University of Eindhoven.

du Plessis, M. 2014. A Decade of Porous Silicon as Nano-Explosive Material. *Propellants, Explosives, Pyrotechnics,* 39**,** 348-364.

Ecker, M. 2000. MESICON OMI. 1.2 ed. Martin Luther University of Halle-Wittenberg.

El-Houte, S., El-Sayed, M & Toft Sørensen, O. Dehydration of $CuSO_4 \cdot 5H_2O$ studied by conventional and advanced thermal analysis techniques. *Thermochimica Acta*. 138, 107-114.

Perkin Elmer. 2004. *ATR accessories - An overview* [Online]. Available: https://shop.perkinelmer.com/Content/technicalinfo/tch_atraccessories.pdf [Accessed November 2017].

Perkin Elmer. 2005. *FT-IR and FT-NIR Spectrometers* [Online]. Available: http://www.perkinelmer.com/CMSResources/Images/46-74472BRO_Spectrum100FTIR.pdf [Accessed June 2017].

Fitzpatrick, J. A. 1959. *Hydrogen Gas Generating Propellent Compositions* United States of America patent application.

Furnas, C. C. 1931. Gading Aggregates I-Mathematical Relations for Beds of Broken Solids of Maximum Density *Industrial and Engineering Chemistry,* 23**,** 1052-1058.

Janbozorgi, M., Far, K. E. & Metghalchi, H. 2010. 1. Combustion Fundamentals *In:* LACKNER, M., WINTER, F. & AGARWAL, A. K. (eds.) *Handbook of Combustion Vol.1: Fundamentals and Safety.* Weinheim: WILEY-VCH Verlag GmbH & Co. KGaA.

Jennings-White, C. & Kosanke, K. L. 1995. Hazardous Chemical Combinations: A Discussion. *Journal of Pyrotechnics,* 2**,** 333-345.

Khaikin, B. I. & Merzhanov, A. G. 1966. Theory of thermal propagation of a chemical reaction front *Combustion, Explosion and Shock Waves (English Translation),* 2**,** 557-568.

Klapötke, T. M. 2012. *Chemistry of High Energy Materials*, De Gruyter.

Kosanke, B. J. & Kosanke, K. L. 1994. Control of Pyrotechnic Burn Rate. *Second International Symposium on Fireworks.*

Krieger, I. M. 1972. Rheology of monodisperse latices. *Advances in Colloid and Interface Science,* 3**,** 111-136.

Kumar, R. V., Chivall, J., Brook, D., Barber, B. & Sallows, L. 2008. *Ellingham Diagrams* [Online]. Available: http://www.doitpoms.ac.uk/tlplib/ellingham_diagrams/index.php [Accessed 16 March 2016].

Lewry, A., J & Williamson, J. 1994. The setting of gypsum plaster. *Journal of Materials Science,* 29**,** 5279-5284.

Malvern Instruments Ltd. 2017. *Laser Diffraction* [Online]. Available: https://www.malvern.com/en/products/technology/laser-diffraction [Accessed December 2017].

Ludwig, U. & Singh, N. B. 1978. Hydration of Hemihydrate of Gypsum and Its Supersaturation *Cement and Concrete Research,* 8**,** 291-300.

Mangulkar, M. N. & Jamkar, S. S. 2013. Review of Particle Packing Theories Used For Concrete Proportioning *International Journal of Scientific & Engineering Research,* 4**,** 143-148.

Materials Evaluation and Engineering, I. M. 2001. *Handbook of Analytical Methods for Materials* [Online]. Plymouth. Available: www.mee-inc.com [Accessed 8 February 2017].

Mavrovic, I., Shirley Jr, A. R. & Coleman, G. R. B. 2000. Urea. *Kirk-Othmer Encyclopedia of Chemical Technology.* John Wiley & Sons, Inc.

Merzhanov, A. G. & Abramov, V. G. 1981. Thermal Explosion of Explosives and Propellants. A Review. *Propellants and Explosives,* 6**,** 130-148.

Meyer, B. 1976. Elemental Sulfur *Chemical Reviews,* 76**,** 367-388.

Montgomery, Y. C., Focke, W. W., Atanasova, M., Del Fabbro, O. & Kelly, C. 2016. $Mn+Sb_2O_3$ Thermite/Intermetallic Delay Compositions. *Propellants, Explosives, Pyrotechnics***,** 919-925.

Noläng, B. 1996. EkviCalc. 4.30 ed. Balinge, Sweden.

Olander, D. E. & Petersen, D. W. 1983. *Pyrotechnic composition.*

Padevět, P., Tesárek, P. & Plachý, T. 2011. Evolution of mechanical properties of gypsum in time. *International Journal of Mechanics,* 5**,** 1-9.

Pantoya, M. & Granier, J. J. 2005. Combustion Behavior of Highly Energetic Thermites: Nano versus Micron Composites. *Propellants, Explosives, Pyrotechnics,* 30**,** 53-62.

Parr. 2007. *Introduction to Bomb Calorimetry* [Online]. Available: http://www.scimed.co.uk/wp-content/uploads/2013/03/Introduction-to-bomb-calorimetry.pdf [Accessed June 2017].

Parr. 2010. *6200 Isoperibol Calorimeter* [Online]. Available: http://www.parrinst.com/wp-content/uploads/downloads/2011/06/442M_Parr_6200-Calorimeter-Operating-Instructions-pre-Oct-2010.pdf [Accessed 7 September 2017].

The United States Pharmacopeia. 2010. *Physical Tests and Determinations* [Online]. Available: http://www.usp.org/sites/default/files/usp/document/harmonization/gen-chapter/pages_from_pf365.pdf [Accessed December 2017].

The United States Pharmacopeia. 2012. *Powder Flow* [Online]. Available: http://www.drugfuture.com/pharmacopoeia/usp35/PDF/0801-0804%20%5B1174%5D%20POWDER%20FLOW.pdf [Accessed December 2017].

Poling, B. E., Thomson, G. H., Friend, D. G., Rowley, R. L. & Wilding, W. V. 2008. Physical and Chemical Data. *In:* GREEN, D. W. & PERRY, R. H. (eds.) *Perry's Chemical Engineers' Handbook.* 8th Edition ed. New York: McGraw-Hill.

Ramsdell, L. S. & Partridge, E. P. 1929. The Crystal Forms of Calcium Sulphate. *Journal of Mineralogical Society of America***,** 59-74.

Richardson, H. W. 2012. Copper Compounds. *Ullmann's Encyclopedia of Industrial Chemistry.* Weinheim: Wiley-VCH Verlag GmbH & Co. KGaA.

Rutter, N. A. & Bennet, T. D. 2015. *Natural Sciences Tripos Part 1B, Materials Science, Course D: Materials Chemistry* [Online]. Available: https://www.msm.cam.ac.uk/teaching/partIB/courseD/DH.pdf [Accessed 22 June 2016].

Schroder, K. A. & Dass, R. I. 2012. *Method for Manufacturing Energetic Material Composites* 30 August 2012.

Sharma, H. & Prabu, D. 2013. Plaster of Paris: Past, present and future. *Journal of Clinical Orthopaedics and Trauma,* 4**,** 107-109.

Sigma-Aldrich.   2014.   *Urea*   [Online].   Available: https://www.sigmaaldrich.com/MSDS/MSDS/DisplayMSDSPage.do?country=ZA&language=en&productNumber=208884&brand=ALDRICH&PageToGoToURL=https%3A%2F%2Fwww.sigmaaldrich.com%2Fcatalog%2Fproduct%2Faldrich%2F208884%3Flang%3Den [Accessed June 2017].

Sigma-Aldrich.   2015.   *Sulfur*   [Online].   Available: https://www.sigmaaldrich.com/MSDS/MSDS/PleaseWaitMSDSPage.do?language=&country=ZA&brand=ALDRICH&productNumber=213292&PageToGoToURL=https://www.sigmaaldrich.com/catalog/product/aldrich/213292?lang=en&region=ZA&gclid=CjwKCAiA9MTQBRAREiwAzmytw_i0ebZTUN6oAYWgq0WnZETq-XMGpuP2kLusDk97KiZ-2vkrufyP1hoCLgQQAvD_BwE [Accessed November 2016].

Sigma-Aldrich.   2016.   *Copper(II) sulfate pentahydrate*   [Online].   Available: https://www.sigmaaldrich.com/MSDS/MSDS/PleaseWaitMSDSPage.do?language=&country=ZA&brand=SIGALD&productNumber=209198&PageToGoToURL=https://www.sigmaaldrich.com/catalog/product/sigald/209198?lang=en&region=ZA [Accessed November 2016].

Singh, N. B. & Middendorf, B. 2007. Calcium sulphate hemihydrate hydration leading to gypsum crystallization. *Progress in Crystal Growth and Characterization of Materials,* 53**,** 57-77.

Skoog, D. A., Holler, F. J. & Crouch, S. R. 2007. *Principles of Instrumental Analysis* Brooks/Cole.

PQ Hollow Spheres. 2006. *Hollow Glass Microspheres - 5 and 7 series* [Online]. Available: http://www.amtcomposites.co.za/sites/default/files/media/msdata-sheets/Q-Cel%20MSDS.pdf [Accessed November 2016].

Steinhauser, G. & Klapötke, T. M. 2008. "Green" pyrotechnics: a chemists' challenge. *Angew Chem Int Ed Engl,* 47**,** 3330-47.

Steinhauser, G. & Klapötke, T. M. 2010. Using the Chemistry of Fireworks To Engage Students in Learning Basic Chemical Principles: A Lesson in Eco-Friendly Pyrotechnics. *Journal of Chemical Education,* 87**,** 150-156.

Tan, K. H., Hajek, B. F. & Barshad, I. 1986. Thermal Analysis Techniques. *Methods of Soil Analysis, Part 1. Physical and Mineralogical Methods* 2ed. Madison, USA: Americal Society of Agronomy-Soil Science Society of America.

Thomas, M., V & Puleo, D., A 2009. Calcium Sulfate: Properties and Clinical Applications. *Journal of Biomedical Materials Research Part B: Applied Biomaterials* 88B.

Thompson, A. 2009. *Allotropes of sulfur* [Online]. Available: http://www.rsc.org/learn-chemistry/content/filerepository/CMP/00/000/764/cfns%20experiment%205%20-%20allotropes%20of%20sulfur.pdf [Accessed 26 September 2016].

Tichapondwa, S. M., Focke, W. W., Del Fabbro, O. & Kelly, C. 2015. Calcium sulfate as a possible oxidant in "green" silicon-based pyrotechnics time delay compositions. *Propellants, Explosives, Pyrotechnics*, 1-9.

Tydlitát, V., Tesárek, P. & Cerny, R. 2008. Effects of the type of calorimeter and the use of plasticizers and hydrophobizers on the measured hydration heat development of FGD gypsum. *Journal of Thermal Analysis and Calorimetry* 91, 791-796.

Tydlitát, V., Trnik, A., Scheinherrova, L., Podoba, R. & Cerny, R. 2015. Application of isothermal calorimetry and thermal analysis for the investigation of calcined gypsum-lime-metakaolin-water system. *Journal of Thermal Analysis and Calorimetry,* 122, 155-122.

Universitat Politècnica de València. 2012. *Field Emission Scanning Electron Microscopy* [Online]. Available: http://www.upv.es/entidades/SME/info/859071normali.html [Accessed November 2017].

Wang, L. L., Munir, Z. A. & Maximov, Y. M. 1993. Thermite reactions: their utlization in the synthesis and processing of materials *Journal of Materials Science* 28, 3693-3708.

Webb, P. A. 2001. *Volume and Density Determination for Particle Technologists* [Online]. Available: http://www.micromeritics.com/Repository/Files/Volume_and_Density_determinations _for_Particle_Technologists_0.pdf [Accessed 5 September 2016].

Weismiller, M. R., Malchi, J. Y., Lee, J. G., Yetter, R. A. & Foley, T. J. 2011. Effects of fuel and oxidizer particle dimensions on the propagation of aluminum containing thermites. *Proceedings of the Combustion Institute,* 33, 1989-1996.

Whittaker, C. W., Lundstrom, F. O. & Hendricks, S. B. 1933. Reaction between Urea and Gypsum. *Industrial and Engineering Chemistry,* 25, 1280-1282.

Wu, C., Sullivan, K., Chowdhury, S., Jian, G., Zhou, L. & Zachariah, M. R. 2012. Encapsulation of Perchlorate Salts within Metal Oxides for Application as Nanoenergetic Oxidizers. *Advanced Functional Materials,* 22, 78-85.

Zhang, J. & Richardson, H. W. 2016. Copper compounds. *Ullmann's Encyclopedia of Industrial Chemistry.* Weinheim: Wiley-VCH Verlag GmbH & Co. .

A. Appendix A: Characterisation of raw materials by XRF

XRF analysis of the hydrated calcium sulfate hemihydrate, anhydrous calcium sulfate, sulfur, copper sulfate pentahydrate, sodium borosilicate glass spheres raw materials are shown in **Error! Reference source not found.** to **Error! Reference source not found.** respectively.

Table A-1: Mass elemental composition of calcium sulfate dihydrate by XRF analysis

Element	Mass composition (wt-%)
$CaSO_4.2H_2O$	93.25
$CaSO_4$	<0.01
Mg	3.30
Na	2.17
Si	0.49
Sr	0.24
Ba	0.21
Cs	0.13
P	0.11
I	0.07
Fe	0.04
K	0.02
Bi	0.01
Nb	0.01
Total	100.05

Table A-2: Mass elemental composition of calcium sulfate anhydrite by XRF analysis

Element	Mass composition (wt-%)
$CaSO_4$	97.68
$CaSO_4.2H_2O$	<0,01
Mg	3.30
Na	2.17
Si	0.49
Sr	0.24
Ba	0.21
Cs	0.13
P	0.11
I	0.07
Fe	0.04
K	0.02
Bi	0.01
Nb	0.01
Total	**99.95**

Table A-3: Mass elemental composition of sulfur by XRF analysis

Element	Mass composition (wt-%)
S	98.20
Mg	0.36
Na	0.23
Cl	0.06
K	0.05
Px	0.03
Ca	0.02
Pr	0.01
Total	**98.95**

Table A-4: Mass elemental composition of copper sulfate pentahydrate by XRF analysis

Element	Mass composition (wt-%)
CuO	63.81
SO_3	34.72
CaO	0.39
MgO	0.37
SiO_2	0.34
Al_2O_3	0.17
Fe_2O_3	0.06
Cl	0.04
P	0.04
MoO_3	0.03
ZnO	0.01
Total	**99.98**

Table A-5: Mass elemental composition of sodium borosilicate by XRF analysis

Element	Mass composition (wt-%)
SiO_2	55.04
B	25.19
Na_2O	19.27
SO_3	0.24
MgO	0.08
Cl	0.06
BaO	0.03
Al_2O_3	0.02
I	0.01
ZrO_2	0.01
Fe_2O_3	0.01
CaO	0.01
K_2O	0.01
TiO_2	0.01
Total	**99.99**